Engineering Geology 296 (2022) 106462

Contents lists available at ScienceDirect

Engineering Geology

journal homepage: www.elsevier.com/locate/enggeo

A GPU-accelerated Efficient Simulation Tool (EST) for 2D variable-density mud/debris flows over non-uniform erodible beds

S. Martínez-Aranda *, J. Murillo, P. García-Navarro

Fluid Dynamic Technologies-I3A, University of Zaragoza, Spain

ARTICLE INFO

Keywords:
Mud/debris flow
Non-uniform erodible bed
Variable-density mixture
Augmented riemann solvers
Well-balanced schemes
Source terms integration
GPU-accelerated codes

ABSTRACT

Mud/debris flows are among the most challenging gravity-driven flows in environmental and geophysical processes. Natural muddy slurries and debris are solid-laden fluids where the density of the mixture can be more than twice or three times the water density and, hence, the bulk solid phase can represent 40–80% of the flow column volume. Furthermore, these unsteady flows usually occur along steep and irregular terrain which requires a refined non-structured spatial discretization, increasing the computational times of the models. In this work a new upwind Roe-type solver for two-dimensional multi-grain mixture shallow-flow over non-uniform erodible bed is presented. The coupled system of depth-averaged equations is formed by the conservation equations for the mass and momentum of the variable-density mixture, the mass conservation equations for the N different solid phases transported in the flow and the continuity equation for the erodible bed layer, where the different solid phases can be exchanged independently modifying the bed level. The non-Newtonian rheological behavior of the multi-grain mixture is included into the momentum equations using six different basal resistance formulations. An accurate, robust and efficient x-split Augmented Roe (xA-Roe) solver for variable-density flow is derived, which requires a complete reformulation of the averaged-Roe values at the intercell edges and allows the mixture density to participate in the definition of the characteristic wave celerities of the local Riemann problem. The global time step is dynamically controlled by the wave celerities of the coupled system of equations, preserving the scheme stability even for high density gradients. The bed slope and basal resistance source terms are also upwind discretized and included into the intercell numerical fluxes, ensuring a well-balanced flux formulation in steady states and the correct treatment of wet-dry fronts. The proposed model is GPU-accelerated using a CUDA/C++ algorithm and applied to synthetic tests and the USGS debris dambreak experiments over erodible bed, demonstrating its robustness, accuracy and efficiency. Finally, the model is tested against a real-scale and long-term case, the mining-tailing dam failure occured in Brumadinho (Brazil) in 2019. The numerical results show good agreement with the observed field data and the computational cost reduction obtained with the GPU-accelerated algorithm is up to 60 times compared to a CPU-based code.

1. Introduction

Mud/debris flows are probably the most challenging and unknown gravity-driven flows in environmental and geophysical processes. In this kind of flows the fluid in motion consists of a mixture of water and multiple solid phases of different nature, such as different sediment size-classes, organic materials, or heavy metals in mine tailings, moving rapidly downstream steep channels. Natural muddy slurries and debris are considered highly solid-laden fluids where the density of the mixture can be more than twice or three times the water density and the bulk solid phase represents 40–80% of the flow volume (Iverson, 1997). Furthermore, the characteristic size of the different solid phases varies from couple of meters (for boulders or trees stumps) to very fine materials (as fine clay or heavy metal particles).

The presence of the solid phases, especially the fine material, affects the rheological behavior of the mixture. Therefore, different states can be distinguished in highly solid-laden shallow flows. A clear-water flow transitions into a hyperconcentrated flow when particles on the bed begin to move together and coarse sediment becomes suspended in the flow. Following Pierson (2005), the water-sediment mixture rheology begins to be affected by fine solid particles transported in the flow when the volumetric concentration of fine sediment particles reaches about

* Corresponding author.
E-mail address: sermar@unizar.es (S. Martínez-Aranda).

https://doi.org/10.1016/j.enggeo.2021.106462
Received 12 July 2020; Received in revised form 19 October 2021; Accepted 14 November 2021
Available online 23 November 2021

4% by volume, creating a slight shear strength within the fluid. For higher concentrations the mixture shows a marked non-Newtonian rheology. Mud/debris flows lie between hyperconcentrated flows and dry avalanches (Hungr et al., 2001). The high concentration of solids generates a critical yield stress which allows that coarse particles can be suspended indefinitely in the mixture flow (Calhoun and Clague, 2018). Mud/debris flows are characterized by high sediment volume concentrations, often greater than 60%. In debris flows, sand/gravel and coarser sediment fractions predominate in the solid phase whereas dominant fine fractions (silt and clay) are typical of mud flows. Also the plasticity of the fine transported materials has been used to difference debris flows (plasticity index lower than 5%) from muddy slurries with plasticity index larger than 5% in the sand and finer fractions (Hungr et al., 2001). Nevertheless, these transitional processes in the flow behavior are extremely complex and continue to be debated up to now.

The mathematical modeling of solid-liquid mixture flows and their numerical resolution is still a challenging topic, especially when dealing with realistic applications. When liquid and solid phases are well-mixed, assuming that the solid phase is distributed uniformly over the flow column allows the use of depth-averaged models derived from the vertical integration of the Navier-Stokes equations (Wu, 2007). The simplest models consider null or small enough mixture density variations throughout the flow and hence the mixture density can be extracted from the conservative terms of the depth-averaged equations. Most of the numerical models reported for highly solid-laden flows use this one-single-phase approach, neglecting the mixture density in the shallow-flow mass and momentum conservation equations (Brufau et al., 2000; Murillo and García-Navarro, 2012; Luna et al., 2012; Juez et al., 2013). Based on the same assumption of small density gradients, Cao et al. (2004) manipulated the depth-averaged equations to decouple the flow density and depth, leading to a modified form of the shallow-water equations where the mixture density spatial gradients only contribute within the momentum conservation equation as a source term. This simplification has been widely used since it allows to compute the numerical fluxes at the intercell edges using the numerical schemes implemented for plain shallow-water models. Mathematically, this momentum source term involving the horizontal density gradients needs to be carefully treated but its effect seems to be negligible even for complex water-sediment flow processes (Cao et al., 2015; Xia et al., 2017).

More complicated models consider transport of the liquid and solid phases presented in the mixture. Some distinctions can be made here between two-phase and quasi-single-phase models. On the one hand, two-phase approaches consider the depth-averaged mass and momentum conservation for the liquid and solid phases separately (George and Iverson, 2011; Meng and Wang, 2016; Li et al., 2018; Greco et al., 2019; Hess et al., 2019). Theoretically, the two-phase mathematical framework describes properly the complex interaction between fluid and solid particles within the mixture but the high uncertainty involved in the equations and the difficulty to implement efficient and robust numerical schemes have hindered its application to realistic geophysical problems. Two-phase depth-averaged systems have been proposed using the two different sets of equations: the first option is based on the liquid and solid phases mass and momentum conservation laws; the second one consists of using the bulk mixture and solid phase conservation equations. It is known that the first option suffers from loss of hyperbolicity since the eigenvalues of the coupled Jacobian matrix of the liquid and solid convective fluxes become complex under certain configurations (Kowalski, 2008; Pitman and Le, 2005). This drawback can cause that numerical models based on the complete eigenstructure of the Jacobian (Roe-type approach) become unstable (Pelanti et al., 2008) so that the loss of hyperbolicity must be prevented numerically. The latter option ensures the hyperbolicity of the mathematical system and successful models have been reported in the last five years (Li et al., 2018, 2019, 2020; Xia et al., 2018). However, despite the benefits offered by this reformulation, the computational effort demanded by two-phase numerical models is much larger than that required by one-single-phase or quasi-single-phase models.

On the other hand, an alternative approach consists of encapsulating solid-fluid phase velocities into the depth-averaged bulk velocity of the mixture by accounting for the effects of solid-fluid particle interactions in the mixture stresses. This leads to the quasi-single-phase approach, which considers separately the mass and momentum conservation for the mixture and the mass conservation for the solid phase. Many versions of this approach have been reported in last years. Both Iverson and Denlinger (2001) and Denlinger and Iverson (2001) adopted a constant-density one phase approach but included the solid-liquid phase interaction effects in the mixture basal resistance by using the Terzaghi's effective stress principle, i.e. normal stresses at grain contacts are proportional to bulk normal stresses minus the pore-fluid pressure. The pore-fluid pressure was estimated as a fraction of the basal normal stress, indicating the liquefaction state of the flow. Lancaster et al. (2003) assumed the same hypothesis but estimated the pore-fluid pressure at the basal surface as an excess of pressure over the hydrostatic value. George and Iverson (2014) proposed a constant-density mixture model but added a vertical dissipation term for the pore-fluid pressure and advected this pressure with the bulk mixture velocity. The solid-liquid phases interaction was included into the momentum equations by the evolution of the granular dilatancy, which was determined by the evolution of the pore-fluid pressure excess and solid volume fraction. Kowalski and McElwaine (2013) derived a one-dimensional quasi-single-phase model where changes on the flow density were included into the homogeneous fluxes and the pore-fluid pressure component of the bulk mixture stress was algebraically coupled to the volume fraction, based on whether there is net solid phase settling or resuspension. The quasi-single-phase mathematical approach requires important simplifications of the multi-grain mixture physics but their unconditional hyperbolic character represents a decisive advantage in order to develop efficient numerical models able to deal with realistic large-scale mud/-debris events.

Other important aspect of mud/debris flows is the entrainment of materials from the erodible bed layer. The mass exchange between mud/debris flow layer and the erodible bed involves complicated physical processes and the understanding of the theoretical basis remains unclear. Experiments in large-scale channels (Egashira et al., 2001; Rickenmann et al., 2003; Iverson et al., 2011) and field observations in real debris events (Wang et al., 2003; Berger et al., 2011; McCoy et al., 2012) indicate that the entrainment volume in steep beds can be in the same order of magnitude of the initial volume mobilized. Mud/debris flows gain much of their mass and momentum as they move over steep slopes as a consequence of the material entrainment from the erodible bed, before deposition begins on flatter terrain downstream. Armanini et al. (2009) proposed a 2D quasi-single-phase model including the mixture density into the homogeneous part of the system and taking into account the bulk bed entrainment. Both Ouyang et al. (2015a) and Ouyang et al. (2015b) also included the bulk bed entrainment in their 2D single-phase models but considering additional momentum terms due to entrainment and deposition of the solid phase (Iverson and Ouyang, 2015). These additional momentum exchange terms bewteen the bed and the flow layer are problematic since they must vanish from a physical perspective (Cao et al., 2017). Moreover, natural beds involve different size sediment particles which participate directly in the bulk solid phase volume when they are incorporated into the moving mixture. Each sediment size-class can be considered as an independent solid phase, with its own entrainment and settling processes, leading to multi-grain mixture models. Both Li et al. (2018) and Xia et al. (2018) obtained promising results using a 1D two-phase and a 1D quasi-single-phase model, respectively, including entrainment of different sediment classes into the multi-grain mixture.

One of the biggest challenges for the application of depth-averaged models to realistic large-scale long-term mud/debris flows is the computational effort required. This kind of unsteady flows usually occur

along very steep and irregular terrain which requires to use a refined non-structured spatial discretization in order to capture the terrain complexity, increasing exponentially the computational times. Furthermore, the complexity of the numerical resolution and the computational cost of the solvers also increase considerably with the number of equations involved and the coupling between flow variables adds special features to the mathematical model. Most of the numerical models specially designed for mud/debris flow are one-dimensional or their resolution procedures are based on square-structured meshes in case of 2D models. There exists a lack of efficient and robust two-dimensional numerical models specifically designed for mud/debris flows and able to work with non-structured triangular meshes. New strategies to reduce the computational effort have been developed in the last decade through the use of parallelization techniques based on Multiprocessing (OpenMP) or Message Passing Interface (MPI), which allow to run simulations on multi-CPU clusters. Their main drawback is the associated hardware cost and energy requirements, which are directly proportional to the number of CPU-cores available and limit their efficiency. In the last 5 years, the use of Graphic Processing Units (GPU) hardware accelerators for sequential computation has demonstrated to be an efficient and low cost alternative to the traditional multi-CPU strategies (Lacasta et al., 2015). GPU-accelerated algorithms have been developed for real-time flood forecasting (Lacasta et al., 2014, 2015b; Ming et al., 2020), real-scale bedload erosive shallow-flows (Juez et al., 2016) or tsunami prediction (de la Asunción and Castro, 2017; Macías et al., 2017).

In this work, an upwind Roe-type Riemann solver is formulated for the quasi-single-phase system of equations formed by the 2D conservation equations for the mass and momentum of the mixture, the mass conservation equation for the N different solid phases transported in the flow and the non-uniform bed variation equation. The bulk mixture density varies according to the volumetric concentration of the different solid-phases and is included into both the conserved variables and the convective fluxes. The non-Newtonian rheological behavior of the multi-grain mixture is included into the momentum equations using different basal resistance formulations (Murillo and García-Navarro, 2012). The complete eigenstructure of the approximate Riemann problem is defined to properly couple density variations and flow depth into the homogeneous part of the system. The global time step is dynamically controlled by the wave celerities given by the Jacobian eigenvalues, preserving the scheme stability even for large density gradients and wetting-drying situations. Following Murillo and Navas-Montilla (2016) and Martínez-Aranda et al. (2020), the bed slope and basal resistance source terms are also projected on the eigenvectors and included into the numerical fluxes (augmented approach), ensuring a well-balanced flux formulation in steady states and wet-dry fronts in both structured and unstructured meshes. Furthermore, this upwind discretization of the source terms avoids additional time step reductions to ensure the stability of the solution regardless of the basal resistance formulation (Martínez-Aranda et al., 2020). GPU-acceleration techniques are applied to generate an Efficient Simulation Tool (EST) suitable for realistic large-scale long-term mud/debris events without requiring the use of coarse meshes.

This paper is structured as follows: in Section 2 the two-dimensional quasi-single-phase equations for multi-grain mud/debris flows over non-uniform erodible beds are presented; Section 3 is devoted to describe the proposed x-split Augmented Roe (xA-Roe) scheme for variable-density flows, paying especial attention to the formulation of the numerical fluxes at the cell edges, the correct integration of the momentum source terms and the liquid-solid phase decoupling; the GPU-base algorithm implementation is detailed in Section 4. The numerical results have been reported in Section 5: first, the numerical scheme properties are analyzed using synthetic cases and the model is validated against the complete set of USGS debris dambreak experiments reported by Iverson et al. (2011); second, the model capabilities are assessed by simulating the mining-tailings dam failure occurred on 25th January 2019 at Brumadinho (Brazil). Finally, the conclusions are drawn in Section 6.

2. Governing equations

The depth-averaged model for the variable-density multi-grain mixture flows over non-uniform erodible beds is derived from the integration of the Navier-Stokes equations along the vertical direction in the flow and bed layer assuming hydrostatic pressure distribution and includes the mass conservation equation for the fluid-solid mixture:

$$\frac{\partial}{\partial t}(\rho h)+\frac{\partial}{\partial x}(\rho \mathrm{hu})+\frac{\partial}{\partial y}(\rho \mathrm{hv})=-\sum_{p=1}^{N}\rho_{b,p}\frac{N_{b,p}}{1-p_p} \tag{1}$$

being ρ the depth-averaged fluid-solid mixture density, h the vertical flow depth and (u, v) are the components of the depth-averaged flow velocity vector $\mathbf{u}$ along the (x, y) horizontal coordinates. Additionally, the mass conservation equations for the N different solid phases composing the mixture are expressed as:

$$\begin{aligned}&\frac{\partial}{\partial t}(\rho_1 h\varphi_1)+\frac{\partial}{\partial x}(\rho_1 \mathrm{hu}\varphi_1)+\frac{\partial}{\partial y}(\rho_1 \mathrm{hv}\,\varphi_1)=-\rho_1 N_{b,1}\\ &\vdots\\ &\frac{\partial}{\partial t}(\rho_N h\varphi_N)+\frac{\partial}{\partial x}(\rho_N \mathrm{hu}\varphi_N)+\frac{\partial}{\partial y}(\rho_N \mathrm{hv}\varphi_N)=-\rho_N N_{b,N}\end{aligned} \tag{2}$$

where ρ_p and φ_p are the density and depth-averaged volumetric concentration in the flow of the pth solid phase respectively with $p = 1, \ldots, N$. The horizontal momentum conservation equations for the fluid-solid mixture can be written as follows:

$$\frac{\partial}{\partial t}(\rho \mathrm{hu})+\frac{\partial}{\partial x}(\rho \mathrm{hu}^2+\frac{1}{2}g_\psi \rho h^2)+\frac{\partial}{\partial y}(\rho \mathrm{huv})=-g_\psi \rho h\frac{\partial z_b}{\partial x}-\tau_x \tag{3}$$

$$\frac{\partial}{\partial t}(\rho \mathrm{hv})+\frac{\partial}{\partial x}(\rho \mathrm{huv})+\frac{\partial}{\partial y}(\rho \mathrm{hv}^2+\frac{1}{2}g_\psi \rho h^2)=-g_\psi \rho h\frac{\partial z_b}{\partial x}-\tau_y \tag{4}$$

where z_b is the bed layer elevation, the momentum terms (τ_x, τ_y) are the components of the depth-averaged basal resistance vector $\boldsymbol{\tau}$ for the mixture flow along the (x, y) horizontal coordinates and $g_\psi = g\cos^2\psi$ is the bed-normal projection of the gravity in the (x, y) horizontal coordinates system, being g the gravitational acceleration and $\cos\psi$ the direction cosine of the bed normal with respect to the vertical axis (Juez et al., 2013). The mass conservation equation for the non-uniform erodible bed layer is expressed as:

$$\sum_{p=1}^{N}\frac{\partial}{\partial t}(\rho_{b,p}F_{b,p}z_b)=\sum_{p=1}^{N}\rho_{b,p}\frac{N_{b,p}}{1-p_p} \tag{5}$$

where $F_{b,p}$ denotes the bed fraction of the pth solid phase, which is considered constant in time and space with $\sum_{p=1}^{N}F_{b,p}=1$, and the term $\rho_{b,p}=\rho_w C_{w,p}+\rho_p(1-p_p)$ is the deposition density of the pth solid phase in the static bed, being ρ_w the fluid phase density, $C_{w,p}$ the specific fluid content in the static bed layer and p_p the specific deposition porosity for the pth solid phase. On the right hand side (RHS) of (1), (2) and (5) the term $N_{b,p}$ is the net volumetric solid exchange flux between the bed layer and the flow for the pth solid phase.

The bulk density of the fluid-solid mixture is estimated as $\rho=\rho_w+\sum_{p=1}^{N}(\rho_p-\rho_w)\varphi_p$. Accordingly, the ratio of the mixture density to the fluid density $r=\rho/\rho_w$ can be expressed by defining a new variable φ^χ, referred as buoyant solid concentration:

$$r=\frac{\rho}{\rho_w}=1+\varphi^\chi \quad \text{with}: \varphi^\chi=\sum_{p=1}^{N}\frac{\rho_p-\rho_w}{\rho_w}\varphi_p \tag{6}$$

Using (6), the equations forming the two-dimensional system (1)–(5) can be reduced to five conservation laws and rewritten in vector form as:

$$\frac{\partial \mathrm{U}}{\partial t}+\frac{\partial \mathrm{F(U)}}{\partial x}+\frac{\partial \mathrm{G(U)}}{\partial y}=\mathrm{S_b(U)}+\mathrm{S_\tau(U)}+\mathrm{E_b(U)} \tag{7}$$

where **U** is the vector of conserved variables and **F(U)** and **G(U)** are the convective fluxes along the (x, y) horizontal coordinates respectively:

$$\mathrm{U} = (\,\mathrm{rh},\quad \mathrm{rhu},\quad \mathrm{rhv},\quad h\varphi^{\chi},\quad z_b\,)^T \tag{8}$$

$$\mathrm{F(U)} = \begin{pmatrix} \mathrm{rhu} \\ \mathrm{rhu}^2 + \frac{1}{2} g_{\psi} r h^2 \\ \mathrm{rhuv} \\ \mathrm{hu}\,\varphi^{\chi} \\ 0 \end{pmatrix} \quad \mathrm{G(U)} = \begin{pmatrix} \mathrm{rhv} \\ \mathrm{rhuv} \\ \mathrm{rhv}^2 + \frac{1}{2} g_{\psi} r h^2 \\ \mathrm{hv}\,\varphi^{\chi} \\ 0 \end{pmatrix} \tag{9}$$

Note that mixture density and flow depth are coupled in the conserved variables and convective fluxes. The vector $\mathbf{S_b(U)}$ accounts for the momentum source term associated to the variation of the pressure force on the bed interface, whereas $\mathbf{S_\tau(U)}$ is the momentum dissipation due to the basal resistance:

$$\mathrm{S_b(U)} = \begin{pmatrix} 0 \\ -g_{\psi} \mathrm{r\ h} \dfrac{\partial z_b}{\partial x} \\ -g_{\psi} \mathrm{r\ h} \dfrac{\partial z_b}{\partial y} \\ 0 \\ 0 \end{pmatrix} \mathrm{S_\tau(U)} = \begin{pmatrix} 0 \\ -\tau_x/\rho_w \\ -\tau_y/\rho_w \\ 0 \\ 0 \end{pmatrix} \tag{10}$$

To date, there is not a universal closure relation for representing the basal resistance $\boldsymbol{\tau}$ in mud/debris flows. Stresses in fluid-solid multi-phase flows include distinct contributions from solid grains friction, intergranular fluid shear stress, and solid-fluid interactions (Jakob and Hungr, 2005). The basal resistance formulation must incorporate the bulk rheological behavior of the liquid-solid mixture in motion. Different kinds of stresses influence this complex rheology. The modulus of the turbulent-dispersive stress τ_t act throughout the fluid phase and its contribution to the basal resistance at the bed interface is commonly expressed as a quadratic velocity relation:

$$\tau_t = \rho g_{\psi} h C_f |\mathbf{u}|^2 \tag{11}$$

where $C_f = n^2\, h^{-4/3}$ is a friction coefficient and n is the Manning's roughness coefficient. Similarly, a viscous stress modulus τ_μ appears also due to the shear deformation of the pore-fluid and generates a basal resistance contribution commonly expressed using a linear shear rate relation:

$$\tau_\mu = 3\mu \frac{|\mathrm{u}|}{h} \tag{12}$$

being μ the dynamic viscosity. Rheological measurements of muddy debris-flows also indicate the existence of a finite yield strength τ_y which opposes the liquid-solid mixture deformation. Typical values for the yield strength τ_y can be in the range 10–400 *Pa* (O'Brien and Julien, 1988; Parsons et al., 2001). The frictional intergranular stress is usually modeled using a generalized Coulomb-type relation between the effective normal stress at the bed interface and the basal intergranular shear resistance τ_f:

$$\tau_f = (\rho g_{\psi} h - \sigma_{\mathrm{pp}}) tan\phi_b + c \tag{13}$$

where ϕ_b denotes the basal friction angle for the grain-bed interface, c is the cohesive strength component and σ_{pp} estimates the pore-fluid pressure at the bed interface (Jakob and Hungr, 2005). For granular material subject to large deformations, as in debris flows, cohesive forces are generally negligible. Estimation of the pore-pressure relaxation for mud/debris flows in motion is a challenging task for modeling multi-phase fluid-solid flows (Iverson, 1997; Iverson and Vallance, 2001; Jakob and Hungr, 2005), although its effects on the reduction of the intergranular effective frictional stress seem to be demonstrated (Major and Iverson, 1999; Berti et al., 1999; Berti and Simoni, 2005; McArdell et al., 2007; Iverson et al., 2011). As a simplification, an idealized relation $\sigma_{\mathrm{pp}} = \gamma_{\mathrm{pp}} \rho_w g\ \mathrm{h} cos\psi$ has been previously used in literature (Denlinger and Iverson, 2001; Lancaster et al., 2003; Ouyang et al., 2015a), being γ_{pp} a coefficient for estimating the excess of pore-fluid pressure over its hydrostatic value at the bed surface, which usually takes values from about 1.4 to 1.8 (Iverson et al., 2010; Lancaster et al., 2003).

All these kind of stresses act simultaneously along the mixture column and are combined in different ways to estimate the bulk rheological behavior of the liquid-solid flow. Non-Newtonian Bingham-type muddy mixtures do not flow until a threshold value of the tangential stress, the yield strength τ_y, is reached. During the movement, the boundary basal shear stress $\boldsymbol{\tau}$ is characterized by means of a cubic equation accounting for the plastic viscosity of the sediment-water mixture:

$$2|\boldsymbol{\tau}|^3 - 3(\tau_y + 2\tau_\mu)|\boldsymbol{\tau}|^2 + \tau_y^3 = 0 \tag{14}$$

The Coulomb-Viscous rheological model also estimates the basal resistance $\boldsymbol{\tau}$ using a cubic relation accounting for the intergranular frictional stress and the viscous shear stress in the pore fluid:

$$2|\boldsymbol{\tau}|^3 - 3(\tau_f + 2\tau_\mu)|\boldsymbol{\tau}|^2 + \tau_f^3 = 0 \tag{15}$$

The different basal resistance formulations considered in this work have been summarized in Table 1. The basal resistance term in the momentum equations (3) and (4) is estimated as:

$$\boldsymbol{\tau} = \mathrm{sgn}\,(u, v)\,|\boldsymbol{\tau}|. \tag{16}$$

In (7), the source term $\mathbf{E_b(U)}$ accounts for the mass net exchange flux between the mixture flow and the bed layer:

$$\mathrm{E_b(U)} = \begin{pmatrix} -N_b^r \\ 0 \\ 0 \\ -N_b^{\chi} \\ N_b^z \end{pmatrix} = \begin{pmatrix} -\sum_{p=1}^{N} \dfrac{r_{b,p}}{1-p_p} N_{b,p} \\ 0 \\ 0 \\ -\sum_{p=1}^{N} \dfrac{\rho_p - \rho_w}{\rho_w} N_{b,p} \\ \sum_{p=1}^{N} \dfrac{1}{1-p_p} N_{b,p} \end{pmatrix} \tag{17}$$

where $r_{b,p} = \rho_{b,p}/\rho_w$ and $N_{b,p} = D_p - E_p$, being D_p and E_p the specific deposition and erosion rates for the pth solid phase, which can be expressed as a function of the mixture depth-averaged volumetric concentration φ_p and the capacity volumetric concentration φ_p^*, respectively:

$$\begin{aligned} D_p &= \alpha_p\, \omega_{s,p}\, \varphi_p (1 - \varphi_0)^{m_0}\, cos\psi \\ E_p &= \alpha_p\, \omega_{s,p}\, \varphi_p^* \end{aligned} \tag{18}$$

where α_p is an empirical parameter representing the difference between

Table 1
Flow resistance formulations.

	Formulation	Flow resistance relation
PT	Pure turbulent	$\lvert\boldsymbol{\tau}\rvert = \tau_t$
TC	Turbulent & Coulomb	$\lvert\boldsymbol{\tau}\rvert = \tau_t + \tau_f$
SB	Simplified Bingham	$\lvert\boldsymbol{\tau}\rvert = 1.5\tau_y + 3\tau_\mu$
FB	Full Bingham	$2\lvert\boldsymbol{\tau}\rvert^3 - 3(\tau_y + 2\tau_\mu)\lvert\boldsymbol{\tau}\rvert^2 + \tau_y^3 = 0$
QD	Quadratic	$\lvert\boldsymbol{\tau}\rvert = \tau_y + \tau_t + \kappa/8\ \tau_\mu$
CV	Coulomb–Viscous	$2\lvert\boldsymbol{\tau}\rvert^3 - 3(\tau_f + 2\tau_\mu)\lvert\boldsymbol{\tau}\rvert^2 + \tau_f^3 = 0$

the near-bed concentration and the depth-averaged concentration for the pth solid phase, $\varphi_0 = \sum_{p=1}^{N} \varphi_p$ is the bulk solid volumetric concentration in the mixture, m_0 is an empirical exponent accounting for the hindering effect on the settling velocity due to high suspended concentrations, and $\omega_{s,p}$ denotes the specific settling velocity of the sediment particles in clear water, computed using the Zhang and Xie (1993) formula:

$$\omega_{s,p} = \left[\left(13.95 \frac{\nu}{d_p} \right)^2 + 1.09 \frac{\rho_p - \rho_w}{\rho_w} g\, d_p \right]^{\frac{1}{2}} - 13.95 \frac{\nu}{d_p} \tag{19}$$

being d_p the characteristic grain diameter of the pth solid phase and ν the kinematic viscosity of water. In mud/debris flows, solid and liquid phases are generally well mixed along the flow column, hence it is common to adopt $\alpha_p = 1$ and the empirical exponent m_0 takes a value around 4.

For the estimation of the specific entrainment rate, φ_p^* denotes the capacity solid concentration for each solid phase, computed as:

$$\varphi_p^* = A_{b,p} \frac{q_{s,p}^*}{h|\mathrm{u}|} \tag{20}$$

where $q_{s,p}^*$ accounts for the phase-specific solid transport throughout the mixture column in capacity regime, which is estimated using the Wu (2007) formula:

$$\frac{q_{s,p}^*}{\beta_T \sqrt{\left(\rho_p / \rho_w\right) g d_p^3}} = 5.3 \times 10^{-3} \left[\left(\frac{n_p}{n} \right)^{1.5} \frac{\theta_{b,p}}{\theta_{c,p}} - 1 \right]^{2.2} + 2.62 \times 10^{-5} \left[\left(\frac{\theta_{w,p}}{\theta_{c,p}} - 1 \right) \frac{|\mathbf{u}|}{\omega_{s,p}} \right]^{1.74} \tag{21}$$

being $n_p = 1/21\, d_p^{1/6}$ the Manning roughness parameter corresponding to grain resistance of the pth solid phase, $\theta_{c,p}$ the critical Shields stress for the incipient motion of the pth solid phase which must include the hiding/exposure mechanism in non-uniform beds, $\theta_{b,p} = |\boldsymbol{\tau}|/[(\rho_p - \rho_w)\, \mathrm{g} d_p]$ the phase-specific Shield stress corresponding to the basal resistance $|\boldsymbol{\tau}|$ at the bed surface, $\theta_{w,p} = \tau_w/[(\rho_p - \rho_w)\mathrm{g} d_p]$ the phase-specific Shield stress throughout the wetted perimeter, with τ_w accounting for the pore-fluid shear stress within the mixture column, and β_T a modification coefficient which is considered equal for all the solid phases composing the mixture.

The term $A_{b,p}$ in (20) denotes the areal exposure fraction of the pth sediment class in the bed layer, satisfying $\sum_{p=1}^{N} A_{b,p} = 1$. The most simplified approach for multi-grain entrainment consists of considering the areal exposure as the specific fraction in the bed layer $A_{b,p} = F_{b,p}$ (Martínez-Aranda et al., 2020), referred to as fixed-fractions approach from now on. In this approach, the hidding /exposure effects on the non-uniform bed surface are included into the capacity solid transport $q_{s,p}^*$ by the specific critical Shields stress for each sediment class $\theta_{c,p}$ (Wu, 2007). In this work, the critical Shields stress for the pth sediment class in the non-uniform bed is estimated using the Egiazaroff (1965) relationship:

$$\theta_{c,p} = \begin{cases} 0.843 \left(\dfrac{d_{s,p}}{d_m} \right)^{-1} \theta_c & \text{if} \quad \dfrac{d_{s,p}}{d_m} \leq 0.4 \\ \left(\dfrac{log19}{log\left(19\, d_{s,p}/d_m\right)} \right)^2 \theta_c & \text{if} \quad \dfrac{d_{s,p}}{d_m} > 0.4 \end{cases} \tag{22}$$

being θ_c a bulk value for the critical Shields stress and $d_m = \sum_{p=1}^{N} F_{b,p}\, d_{s,p}$ the medium sediment diameter in bed layer.

A more complicated approach is provided by the active layer concept (Hirano, 1971), where the areal exposure is given by:

$$A_{b,p} = \frac{f_{a,p}/d_p}{\sum_{p=1}^{N} f_{a,p} \Big/ d_p} \tag{23}$$

being $f_{a,p}$ the fraction of the pth sediment class in the active layer, which satisfies $\sum_{p=1}^{N} f_{a,p} = 1$. The active layer is placed between the mud/debris flow layer and the static substrate bed layer. Sediments in the active layer can be freely exchanged with the flow and the underlying bed layer.

Following Li et al. (2018) and Xia et al. (2018), the specific conservation law for each sediment class in the active layer is formulated as:

$$\frac{\partial}{\partial t}(f_{a,p}\eta_a) + f_{s,p} \frac{\partial (z_b - \eta_a)}{\partial t} = \frac{N_{b,p}}{1 - p_p} \tag{24}$$

being η_a the active layer thickness, which is estimated here as $\eta_a = 2\, d_{84}$ (Wu, 2007; Li et al., 2018), and d_{84} the size for which 84% of the sediment particles is finer. The term $f_{s,p}$ denotes fraction of the pth sediment class at the interface between the active layer and the underlying bed, i.e. $(z_b - \eta_a)$, which satisfies $\sum_{p=1}^{N} f_{s,p} = 1$. The specific fraction $f_{s,p}$ at the active interface $(z_b - \eta_a)$ is estimated here as:

$$f_{s,p} = \begin{cases} F_{b,p} & \text{if} \quad \partial(z_b - \eta_a)/\partial t \leq 0 \\ \beta_a \varphi_p / \varphi_0 + (1 - \beta_a) f_{a,p} & \text{if} \quad \partial(z_b - \eta_a)/\partial t > 0 \end{cases} \tag{25}$$

where β_a is tuning weighting parameter and φ_p/φ_0 represents the relative concentration of the pth sediment class in the mud/debris flow.

3. Finite volume method for variable-density flows

This section is devoted to the derivation of a new Finite Volume (FV) numerical scheme for 2D variable-density multi-grain mixture flow considering net exchange mass flux between the mixture and the bed layer. System (7) is time dependent, non linear and contains source terms. Under the hypothesis of dominant advection it can be classified as belonging to the family of hyperbolic systems. In order to obtain a numerical solution, the spatial domain is divided in computational cells using a mesh fixed in time and system (7) is integrated in each cell Ω_i using the Gauss theorem:

$$\frac{d}{\mathrm{d\,t}} \int_{\Omega_i} \mathrm{U}\, d\Omega + \oint_{\partial\Omega_i} \mathrm{E{\cdot}n\,dl} = \int_{\Omega_i} \mathrm{S_b(U)}\, d\Omega + \int_{\Omega_i} \mathrm{S_\tau(U)}\, d\Omega + \int_{\Omega_i} \mathrm{E_b(U)}\, d\Omega \tag{26}$$

being $\mathbf{E} \cdot \mathbf{n} = \mathbf{F(U)}\, n_x + \mathbf{G(U)}\, n_y$ the flux normal to the Ω_i cell boundary and $\mathbf{n} = (n_x, n_y)$ the outward unit normal vector. Assuming a piecewise uniform representation of the conserved variables $\mathbf{U}$ at the i cell for the time $t = t^n$:

$$\mathrm{U}_i^n = \frac{1}{A_i} \int_{\Omega_i} \mathrm{U}(x, y, t^n)\, d\Omega \tag{27}$$

where A_i is the cell area, (26) can be expressed as:

$$\frac{d}{\mathrm{d}\,t}\int_{\Omega_i} \mathrm{U}\,d\Omega + \sum_{k=1}^{\mathrm{NE}} (\mathrm{E}\cdot\mathrm{n})_k\, l_k = \sum_{k=1}^{\mathrm{NE}} \int_{\Omega_{i,k}} [\mathrm{S_b}(\mathrm{U}) + \mathrm{S_\tau}(\mathrm{U})]\,d\Omega + \int_{\Omega_i} \mathrm{E_b}(\mathrm{U})\,d\Omega \tag{28}$$

being *NE* the number of edges for the *i* cell, $(\mathbf{E}\cdot\mathbf{n})_k$ the value of the normal flux through each edge, l_k the length of the edge and $\Omega_{i,k}$ the area of the *i* cell associated to the *k*th edge.

The theory of Riemann problems (RP) can be used to solve the intercell fluxes in the 2D problem (28). For each *k*th cell edge, it is possible to define a local 1D RP by projecting (7) along **n**. Furthermore, (7) satisfies the rotation invariance property (Godlewski and Raviart, 1996; Castro et al., 2009) and hence can be expressed in the local framework $(\hat{x},\hat{y})$, corresponding to normal and tangential directions to each cell edge respectively. Defining a rotation matrix $\mathbf{T}_k$ for the *k*th cell edge as:

$$\mathbf{T}_k = \begin{pmatrix} 1 & 0 & 0 & 0 & 0 \\ 0 & n_x & n_y & 0 & 0 \\ 0 & -n_y & n_x & 0 & 0 \\ 0 & 0 & 0 & 1 & 0 \\ 0 & 0 & 0 & 0 & 1 \end{pmatrix}_k \tag{29}$$

which satisfies the condition:

$$(\mathrm{E}\cdot\mathrm{n})_k = \left[\mathrm{F}(\mathrm{U})\,n_x + \mathrm{G}(\mathrm{U})\,n_y\right]_k = \mathrm{T}_k^{-1}\,\mathrm{F}(\mathrm{T}_k\mathrm{U}) \tag{30}$$

the local RP normal to the *k*th cell edge can be expressed in the local framework $(\hat{x},\hat{y})$ as (Murillo and García-Navarro, 2012b; Murillo and Navas-Montilla, 2016):

$$\frac{\partial \mathrm{T}_k\mathrm{U}}{\partial t} + \frac{\partial \mathrm{F}(\mathrm{T}_k\mathrm{U})}{\partial \hat{x}} = \mathrm{T}_k\mathrm{S_b} + \mathrm{T}_k\mathrm{S_\tau}$$
$$\mathrm{T}_k\mathrm{U}(\hat{x},0) = \begin{cases} \mathrm{T}_k\mathrm{U}_i & \text{if} \quad \hat{x} < 0 \\ \mathrm{T}_k\mathrm{U}_j & \text{if} \quad \hat{x} > 0 \end{cases} \tag{31}$$

where subscripts *i* and *j* indicate the left and right cells of the *k*th edge, respectively. Note that the net exchange term between the mixture flow and the bed, $\mathbf{E_b}$, has been dropped in the local RP (31) since it implies a mass source rather than a momentum source and will be incorporated into the solution as a cell-centered contribution, as it is described below.

Therefore, the set of local conserved variables $\widehat{\mathrm{U}} = \mathrm{T}_k\mathrm{U}$ at the cell edge is defined as:

$$\widehat{\mathrm{U}} = \mathrm{T}_k\mathrm{U} = (\,\mathrm{rh},\quad \mathrm{rh}\,\hat{u},\quad \mathrm{rh}\,\hat{v},\quad h\varphi^{\chi},\quad z_b \qquad)^T \tag{32}$$

where $\hat{u} = un_x + vn_y$ and $\hat{v} = -un_y + vn_x$ are the flow velocities along the $\hat{x}$ and $\hat{y}$ coordinates, respectively, and the local convective fluxes $\mathrm{F}(\widehat{\mathrm{U}}) = \mathrm{F}(\mathrm{T}_k\mathrm{U})$ can be expressed as:

$$\mathrm{F}(\widehat{\mathrm{U}}) = \mathrm{F}(\mathrm{T}_k\mathrm{U}) = \begin{pmatrix} \mathrm{rh}\hat{u} \\ \mathrm{rh}\hat{u}^2 + \frac{1}{2}g_\psi rh^2 \\ \mathrm{rh}\hat{u}\hat{v} \\ h\hat{u}\,\varphi^{\chi} \\ 0 \end{pmatrix} \tag{33}$$

The augmented value of the fluxes through the *k*th cell edge in (28) incorporates the non-conservative contribution of the momentum source terms $\mathbf{S_b}$ and $\mathbf{S_\tau}$ into the convective fluxes $(\mathbf{En})_k$. In order to integrate (31) over the space $[-\Delta\hat{x}/2, \Delta\hat{x}/2]$ corresponding to the *k*th edge, the momentum source terms are linearized in time and involved in the Riemann solver as a singular source at the discontinuity $\hat{x} = 0$ so that:

$$\int_{-\Delta\hat{x}/2}^{\Delta\hat{x}/2} \mathbf{T}_k\mathbf{S_b}\,d\hat{x} = \mathbf{T}_k \int_{-\Delta\hat{x}/2}^{\Delta\hat{x}/2} \mathbf{S_b}\,d\hat{x} \approx \mathbf{T}_k\,\mathbf{S_b^\vee}$$
$$\int_{-\Delta\hat{x}/2}^{\Delta\hat{x}/2} \mathbf{T}_k\mathbf{S}\;d\hat{x} = \mathbf{T}_k \int_{-\Delta\hat{x}/2}^{\Delta\hat{x}/2} \mathbf{S}\;d\hat{x} \approx \mathbf{T}_k\,\mathbf{S}^\vee \tag{34}$$

where $\mathbf{S_b^\vee}$ and $\mathbf{S_\tau^\vee}$ are suitable numerical source vectors along the normal direction to the cell edge, which can be expressed in the 2D framework (x, y) as:

$$\mathbf{S_b^\vee} = (\,0,\quad \widetilde{H}\,n_x,\quad \widetilde{H}\,n_y,\quad 0,\quad 0\,)_k^T$$
$$\mathbf{S}^\vee = (\,0,\quad -\widetilde{T}\,n_x,\quad -\widetilde{T}\,n_y,\quad 0,\quad 0\,)_k^T \tag{35}$$

being $\widetilde{H}_k$ and $\widetilde{T}_k$ the bed slope and friction momentum contributions, respectively, spatially integrated in the control volume corresponding to the *k*th cell edge.

Using the rotation invariance property (30) and the solution of the local plane RP (31), it is possible to rewrite (28) as:

$$\frac{d}{\mathrm{d}\,t}\int_{\Omega_i} \mathrm{U}\,d\Omega = -\sum_{k=1}^{\mathrm{NE}} \mathrm{T}_k^{-1}\left(\mathrm{F}(\widehat{\mathrm{U}}) - \widehat{\mathrm{S}}_{\mathrm{b}}^{\vee} - \widehat{\mathrm{S}}_{\tau}^{\vee}\right)_k l_k + \int_{\Omega_i} \mathrm{E_b}(\mathrm{U})\,d\Omega \tag{36}$$

where $\widehat{\mathrm{S}}_{\mathrm{b}}^{\vee} = \mathrm{T}_k\,\mathrm{S}_{\mathrm{b}}^{\vee}$ and $\widehat{\mathrm{S}}_{\tau}^{\vee} = \mathrm{T}_k\,\mathrm{S}_{\tau}^{\vee}$, allowing to define an augmented numerical flux $\mathrm{F}(\widehat{\mathrm{U}})_k^{\downarrow}$ for the *k*th cell edge which incorporates the integrated momentum source terms into the convective numerical fluxes at the cell edge, ensuring the well-balance property for steady states (Murillo and GGarcía-Navarro, 2010):

$$\mathrm{F}(\widehat{\mathrm{U}})_k^{\downarrow} = \left(\mathrm{F}(\widehat{\mathrm{U}}) - \widehat{\mathrm{S}}_{\mathrm{b}}^{\vee} - \widehat{\mathrm{S}}_{\tau}^{\vee}\right)_k \tag{37}$$

Furthermore, the net exchange flux term $\mathbf{E_b(U)}$ is also linearized in time and integrated in space using:

$$\int_{\Omega_i} \mathbf{E_b}(\mathbf{U})\,d\Omega \approx \int_{\Omega_i} \mathbf{E_b}\left(\mathbf{U}_i^n\right) d\Omega = A_i\,\mathbf{E_b}\left(\mathbf{U}_i^n\right) \equiv \mathbf{E}_{\mathbf{b}}^{\boxdot} \tag{38}$$

Replacing (37) and (38) into (36), we obtain the updating formula for the conserved variables **U** at the cells:

$$\mathrm{U}_i^{n+1} = \mathrm{U}_i^n - \frac{\Delta t}{A_i}\sum_{k=1}^{\mathrm{NE}} \mathrm{T}_k^{-1}\,\mathrm{F}(\widehat{\mathrm{U}})_k^{\downarrow}\,l_k + \frac{\Delta t}{A_i}\,\mathrm{E}_{\mathrm{b}}^{\boxdot} \tag{39}$$

where $\Delta t = t^{n+1} - t^n$ is the time step. Hence the resolution procedure needs to compute the numerical fluxes $\mathrm{F}(\widehat{\mathrm{U}})_k^{\downarrow}$ at the cell edges ensuring (37). In this work, we propose a new approximated Riemann solver for variable-density flows based on the augmented Roe solver (A-Roe) approach (Roe, 1981; Toro, 1997; Murillo and GGarcía-Navarro, 2010).

3.1. Riemann solver for variable-density flows

The plane Riemann problem (31) defined in the local framework $(\hat{x}, \hat{y})$ of the *k*th edge, separating the left *i* cell and the right *j* cell, can be approximated by using the following constant coefficient linear RP (Toro, 1997):

$$\frac{\partial \widehat{\mathrm{U}}}{\partial t} + \widetilde{\mathrm{J}}_k\frac{\partial \widehat{\mathrm{U}}}{\partial \hat{x}} = (\widehat{\mathrm{S}}_{\mathrm{b}}^{\vee} + \widehat{\mathrm{S}}_{\tau}^{\vee})_k$$
$$\widehat{\mathrm{U}}(\hat{x},0) = \begin{cases} \widehat{\mathrm{U}}_i = \mathrm{T}_k\mathrm{U}_i^n & \text{if} \quad \hat{x} < 0 \\ \widehat{\mathrm{U}}_j = \mathrm{T}_k\mathrm{U}_j^n & \text{if} \quad \hat{x} > 0 \end{cases} \tag{40}$$

where $\widetilde{\mathrm{J}}_k = \widetilde{\mathrm{J}}_k(\widehat{\mathrm{U}}_i, \widehat{\mathrm{U}}_j)$ is a constant coefficient matrix which approximates the Jacobian of the non-linear RP $\widetilde{\mathbf{J}}_k \approx (\partial\mathbf{F}(\widehat{\mathbf{U}})/\partial\widehat{\mathbf{U}})_k$. Integrating (40) over the discrete space $[\hat{x}_i, \hat{x}_j]$ leads to the following constraint involving conservation across discontinuities:

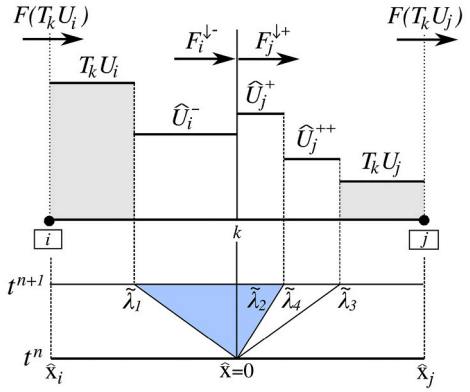

Fig. 1. Sketch of the solution reconstruction for the approximated Riemann solver.

$$\delta \mathrm{F}(\widehat{\mathrm{U}})_k = \widetilde{\mathrm{J}}_k \ \delta \widehat{\mathrm{U}}_k \tag{41}$$

where $\delta\widehat{\mathrm{U}}_k = \widehat{\mathrm{U}}_j - \widehat{\mathrm{U}}_i$ is the conserved variables jump at the kth edge.

It is worth noting that in (33), the convective flux for the bed evolution equation is null and that the mixture mass and momentum convective fluxes do not depend on the bed level variable z_b. Hence the bed evolution equation can be discarded in (40) and the numerical flux for the bed elevation updating is $\mathrm{F}_k^{\{5\}\downarrow} = 0$. Therefore, $\widetilde{\mathrm{J}}_k$ reduces to a 4×4 constant matrix defined as:

$$\widetilde{\mathbf{J}}_k = \begin{pmatrix} 0 & 1 & 0 & 0 \\ \frac{1}{2} g_\psi \widetilde{h}\left(1+\widetilde{r}\right) - \widetilde{u}^2 & 2\widetilde{u} & 0 & -\frac{1}{2} g_\psi \widetilde{h}\widetilde{r} \\ -\widetilde{u}\widetilde{v} & \widetilde{v} & \widetilde{u} & 0 \\ -\widetilde{u}\,\widetilde{\varphi}^\chi/\widetilde{r} & \widetilde{\varphi}^\chi/\widetilde{r} & 0 & \widetilde{u} \end{pmatrix}_k \tag{42}$$

being:

$$\begin{gathered} \widetilde{r} = \frac{r_i h_i + r_j h_j}{h_i + h_j} \qquad \widetilde{h} = \frac{h_i + h_j}{2} \\ \widetilde{u} = \frac{\widehat{u}_i\sqrt{r_i h_i} + \widehat{u}_j\sqrt{r_j h_j}}{\sqrt{r_i h_i} + \sqrt{r_j h_j}} \qquad \widetilde{v} = \frac{\widehat{v}_i\sqrt{r_i h_i} + \widehat{v}_j\sqrt{r_j h_j}}{\sqrt{r_i h_i} + \sqrt{r_j h_j}} \\ \widetilde{\varphi}^\chi = \widetilde{r}\,\frac{\varphi_i^\chi h_i\sqrt{r_j h_j} + \varphi_j^\chi h_j\sqrt{r_i h_i}}{r_i h_i\sqrt{r_j h_j} + r_j h_j\sqrt{r_i h_i}} \end{gathered} \tag{43}$$

The approximate matrix $\widetilde{\mathrm{J}}_k$ (42) is diagonalizable with four approximate real eigenvalues:

$$\widetilde{\lambda}_{1,k} = (\widetilde{u} - \widetilde{c})_k \qquad \widetilde{\lambda}_{2,k} = \widetilde{u}_k \qquad \widetilde{\lambda}_{3,k} = (\widetilde{u} + \widetilde{c})_k \qquad \widetilde{\lambda}_{4,k} = \widetilde{u}_k \tag{44}$$

where the averaged celerity $\widetilde{c}_k$ is defined as:

$$\widetilde{c}_k = \left(\sqrt{\frac{1}{2} g_\psi \widetilde{h}\left(1 + \widetilde{r} - \widetilde{\varphi}^\chi\right)}\right)_k \tag{45}$$

Therefore, using the associated orthogonal basis of eigenvectors $(\widetilde{\mathrm{e}}_m)_k$ of $\widetilde{\mathrm{J}}_k$, a matrix $\widetilde{\mathrm{P}}_k = (\widetilde{\mathrm{e}}_1, \widetilde{\mathrm{e}}_2, \widetilde{\mathrm{e}}_3, \widetilde{\mathrm{e}}_4)_k$ can be built as:

$$\widetilde{\mathrm{P}}_k = \begin{pmatrix} 1 & 0 & 1 & \widetilde{r} \\ \widetilde{\lambda}_1 & 0 & \widetilde{\lambda}_3 & \widetilde{r}\widetilde{u} \\ \widetilde{v} & \widetilde{c} & \widetilde{v} & \widetilde{r}\widetilde{v} \\ \widetilde{\varphi}^\chi/\widetilde{r} & 0 & \widetilde{\varphi}^\chi/\widetilde{r} & 1 + \widetilde{r} \end{pmatrix}_k \tag{46}$$

with the following property:

$$\widetilde{\mathbf{J}}_k = \left(\widetilde{\mathbf{P}}\widetilde{\mathbf{\Lambda}}\widetilde{\mathbf{P}}^{-1}\right)_k^{\sim} = \begin{pmatrix} \widetilde{\lambda}_1 & & 0 \\ & \ddots & \\ 0 & & \widetilde{\lambda}_4 \end{pmatrix}_k \tag{47}$$

being $\widetilde{\mathrm{P}}_k^{-1}$ the inverse matrix of $\widetilde{\mathrm{P}}_k$ and $\widetilde{\Lambda}_k$ a diagonal matrix with approximate eigenvalues in the main diagonal. One result of Roe's linearization is that the approximate Riemann solution consists of only discontinuities and $\widehat{\mathrm{U}}(x,t)$ is constructed as a sum of jumps or shocks. The solution for $\widehat{\mathrm{U}}(x,t)$ is governed by the celerities in $\widetilde{\Lambda}_k$ and consists of four regions connected by 5 waves, one of them a contact wave with null celerity accounting for the integrated source term at $\widehat{x} = 0$ (Fig. 1).

According to the Godunov-type method, it is sufficient to provide the solution for $\widehat{\mathrm{U}}(\widehat{x},t)$ at the intercell position $\widehat{x} = 0$ in order to obtain the updating numerical fluxes $\mathrm{F}_k^{\downarrow}$ (37). The numerical flux at the left and right side of the kth cell edge can be estimated using an approximate flux function $\mathrm{F}(\widehat{x},t)$:

$$\mathbf{F}_k^{\downarrow}\left(\widehat{x}\to 0^-\right) \equiv \mathbf{F}_i^{\downarrow -} = \mathbf{F}\left(\widehat{\mathbf{U}}_i^-\right) \mathbf{F}_k^{\downarrow}\left(\widehat{x}\to 0^+\right) \equiv \mathbf{F}_j^{\downarrow +} = \mathbf{F}\left(\widehat{\mathbf{U}}_j^+\right) \tag{48}$$

being $\widehat{\mathrm{U}}_i^-$ and $\widehat{\mathrm{U}}_j^+$ the intermediate states of the approximated solution at the corresponding side of the kth edge:

$$\widehat{\mathbf{U}}_i^- = \lim_{\widehat{x}\to 0^-} \widehat{\mathbf{U}}_i\left(\widehat{x},t\right) \widehat{\mathbf{U}}_j^+ = \lim_{\widehat{x}\to 0^+} \widehat{\mathbf{U}}_j\left(\widehat{x},t\right) \tag{49}$$

Following Toro (1997), the conserved variable differences $\delta\widehat{\mathrm{U}}_k$ and the integrated momentum source terms $(\widehat{\mathrm{S}}_{\mathrm{b}}^{\vee} + \widehat{\mathrm{S}}_{\boldsymbol{\tau}}^{\vee})_k$ at the cell edge are projected on the eigenvector basis in order to obtain the wave and source strength vectors, $\widetilde{\mathrm{A}}_k$ and $\widetilde{\mathrm{B}}_k$ respectively.

$$\begin{gathered} \widetilde{\mathbf{A}}_k = (\widetilde{\alpha}_1, \ldots, \widetilde{\alpha}_4)_k^T = \widetilde{\mathbf{P}}^{-1}{}_k\, \delta\widehat{\mathbf{U}}_k \quad \longrightarrow \quad \delta\widehat{\mathbf{U}}_k = \sum_{m=1}^{4} (\widetilde{\alpha}_m \widetilde{\mathbf{e}}_m)_k \\ \widetilde{\mathbf{B}}_k = (\widetilde{\beta}_1, \ldots, \widetilde{\beta}_4)_k^T = \widetilde{\mathbf{P}}^{-1}{}_k \left(\widehat{\mathbf{S}}_{\mathbf{b}}^{\vee} + \widehat{\mathbf{S}}^{\vee}\right)_k \quad \longrightarrow \quad \left(\widehat{\mathbf{S}}_{\mathbf{b}}^{\vee} + \widehat{\mathbf{S}}^{\vee}\right)_k = \sum_{m=1}^{4} (\widetilde{\beta}_m \widetilde{\mathbf{e}}_m)_k \end{gathered} \tag{50}$$

The reconstruction of the approximated solution at the left and right sides of the cell edge (Murillo and GGarcía-Navarro, 2010), $\widehat{\mathrm{U}}_i^-$ and $\widehat{\mathrm{U}}_j^+$ respectively, can be expressed as:

$$\widehat{\mathrm{U}}_i^- = \widehat{\mathrm{U}}_i + \sum_{m-} (\widetilde{\gamma}_m \widetilde{\mathrm{e}}_m)_k \widehat{\mathrm{U}}_j^+ = \widehat{\mathrm{U}}_j - \sum_{m+} (\widetilde{\gamma}_m \widetilde{\mathrm{e}}_m)_k \tag{51}$$

where $\widetilde{\gamma}_m = \widetilde{\alpha}_m - \widetilde{\beta}_m/\widetilde{\lambda}_m$ and the subscript $m-$ and $m+$ under the sums indicate waves travelling inward and outward the i cell.

Therefore, the approximated solution for the flux function $\mathrm{F}(\widehat{x},t)$ can also be constructed by defining appropriate Rankine-Hugoniot (RH) relations across each moving wave. The solution of the approximate flux function provides the definition of the numerical fluxes at the left and right sides, $\mathrm{F}_i^{\downarrow -}$ and $\mathrm{F}_j^{\downarrow +}$ respectively, of the kth cell edge:

$$\mathrm{F}_i^{\downarrow -} = \mathrm{F}(\widehat{\mathrm{U}}_i) + \sum_{m-} (\widetilde{\lambda}_m \widetilde{\gamma}_m \widetilde{\mathrm{e}}_m)_k \mathrm{F}_j^{\downarrow +} = \mathrm{F}(\widehat{\mathrm{U}}_j) - \sum_{m+} (\widetilde{\lambda}_m \widetilde{\gamma}_m \widetilde{\mathrm{e}}_m)_k \tag{52}$$

where the subscript $m-$ and $m+$ under the sums indicate waves travelling inward and outward the i cell.

Note that, when momentum source terms are incorporated into the Riemann solver, it is no longer possible to define a unique value of the numerical flux at both sides of the cell edge. The relation between the approximate fluxes $\mathrm{F}_i^{\downarrow -}$ and $\mathrm{F}_j^{\downarrow +}$ can be analyzed using the Rankine-Hugoniot (RH) relation at $\widehat{x} = 0$, which includes a steady contact wave (Rosatti and Begnudelli, 2010; Li and Chen, 2006) between the approximate solutions $\widehat{\mathrm{U}}_i^-$ and $\widehat{\mathrm{U}}_j^+$. The corresponding flux jump for the approximate solution is given by:

$$\mathrm{F}_j^{\downarrow +} - \mathrm{F}_i^{\downarrow -} = \sum_{m=1}^{4} (\widetilde{\beta}_m \widetilde{\mathrm{e}}_m)_k = (\widehat{\mathrm{S}}_{\mathrm{b}}^{\vee} + \widehat{\mathrm{S}}_{\boldsymbol{\tau}}^{\vee})_k \tag{53}$$

and hence the updating formula (39) can be rewritten using the augmented intercell numerical fluxes defined in (52) as:

$$\mathrm{U}_i^{n+1} = \mathrm{U}_i^n - \frac{\Delta t}{A_i}\sum_{k=1}^{\mathrm{NE}} \mathrm{T}_k^{-1}\,\mathrm{F}_i^{\downarrow -}\,l_k + \frac{\Delta t}{A_i}\,\mathrm{E}_{\mathrm{b}}^{\boxdot} \tag{54}$$

Finally, in order to ensure the stability of the explicitly computed numerical solution, the time step should be small enough to avoid the interaction of waves from neighbouring Riemann problems. The dynamical limitation of the time step at each k edge is addressed here assuming that the fastest wave celerity corresponds to the absolute maximum of the eigenvalues of $\widetilde{\mathrm{J}}_k$ (42):

$$\Delta t_k = \frac{min(A_i, A_j)}{l_k\left[max(|\widetilde{\lambda}_1|, |\widetilde{\lambda}_3|)\right]_k} \tag{55}$$

and the global time step $\Delta t = t^{n+1} - t^n$ is limited using the Courant-Friedrichs-Lewy (CFL) condition as:

$$\Delta t = \mathrm{CFL}\min_{\mathrm{k}}\left(\Delta t_k\right) \tag{56}$$

with CFL<1.

3.2. Well-balanced integration of the momentum source terms

The correct integration of the momentum source terms $(\widehat{\mathrm{S}}_{\mathrm{b}}^{\vee})_k$ and $(\widehat{\mathrm{S}}_{\boldsymbol{\tau}}^{\vee})_k$ for the 1D local RP associated to the kth cell edge ensures the well-balanced property of the Riemann solver (Murillo and Navas-Montilla, 2016) and avoids numerical oscillations in the solution when large momentum sources appear, especially associated to the non-Newtonian basal resistance (Burguete et al., 2008; Murillo et al., 2008). The bed slope pressure contribution $\widetilde{H}_k$ in (35) for the kth cell edge is discretized as:

$$\widetilde{H}_k = -g_\psi(\widetilde{\mathrm{rh}})_k\,\delta(z_b)_k \tag{57}$$

being $(\widetilde{\mathrm{rh}})_k$ an edge-averaged value to be defined, and the discrete basal resistance $\widetilde{T}_k$ is integrated as follows:

$$\widetilde{T}_k = \mathrm{sgn}\,(\widehat{u}_k)\frac{1}{\rho_w}\int_{\widehat{x}_i}^{\widehat{x}_j} |\boldsymbol{\tau}|\,d\widehat{x} \approx \mathrm{sgn}\,(\widehat{u}_k)\frac{1}{\rho_w}|\boldsymbol{\tau}(\widehat{\mathrm{U}}_i, \widehat{\mathrm{U}}_j)|\,d_{n,k} \tag{58}$$

where $\boldsymbol{\tau}(\widehat{\mathrm{U}}_i, \widehat{\mathrm{U}}_j)$ is a suitable averaged basal resistance for the kth edge and $d_{n,k}$ is the distance normal to the edge between the center of the i and j cells.

In static conditions, $\widehat{u}_i = \widehat{u}_j = 0$ and the normal momentum equation in the discrete local RP (40) at the kth cell edge reduces to:

$$\frac{1}{2}g_\psi\delta(\mathrm{rh}^2)_k = \widetilde{H}_k - \widetilde{T}_k \tag{59}$$

Considering frictionless flow, i.e. $\widetilde{T}_k = 0$, there exist two different equilibrium configurations which must be maintained (Leighton et al., 2010; Martínez-Aranda et al., 2020). First, considering constant density $r_i = r_j = \widetilde{r}_k$, the uniform free surface condition must be guaranteed:

$$\delta(z_b + h)_k = 0 \tag{60}$$

and, second, considering constant flow depth $h_i = h_j = \widetilde{h}_k$, the discrete density jump must agree:

$$\delta(r)_k = -2\frac{\widetilde{r}_k}{\widetilde{h}_k}\delta(z_b)_k \tag{61}$$

Imposing (60) and (61) into (59) leads to:

$$\widetilde{H}_k = -g_\psi\widetilde{r}_k\,\widetilde{h}_k\,\delta(z_b)_k \tag{62}$$

with $\widetilde{r}_k$ and $\widetilde{h}_k$ as defined in (43). Furthermore, the non-Newtonian basal resistance term $\widetilde{T}_k$ is not null in static conditions, so that it can not be oriented with the velocity sign. Hence, in zero-velocity configurations, the basal resistance is defined to oppose the pressure force generated by the variation of the surface level:

$$\widetilde{T}_k = \begin{cases} +|\widetilde{T}_k| & \text{if} \quad \delta(z_b + h)_k \le 0 \\ -|\widetilde{T}_k| & \text{if} \quad \delta(z_b + h)_k > 0 \end{cases} \tag{63}$$

This discretization of the momentum source contributions at the cell edges ensures the well-balanced formulation of the numerical fluxes in static equilibrium states. However the correct integration of the basal resistance term is not straight-forward and requires a careful treatment in order to avoid numerical instabilities and additional time step restrictions (Murillo and García-Navarro, 2012). A suitable integration procedure for the momentum source terms in variable-density RP were reported in (Martínez-Aranda et al., 2020) and implemented for the proposed model.

3.3. Decoupling of liquid and solid phases

Once the conserved variables are updated using (54), U_i^{n+1}, it is necessary to estimate separately the flow depth h and mixture density ρ at the time $t = t^{n+1}$. From the values of the first and fourth conserved variables, $\mathrm{U}_i^{\{1\}n+1}$ and $\mathrm{U}_i^{\{4\}n+1}$ respectively, the updated values of depth and density can be computed as:

$$\begin{aligned} h_i^{n+1} &= \mathrm{U}_i^{\{1\}n+1} - \mathrm{U}_i^{\{4\}n+1} \\ \rho_i^{n+1} &= \rho_w\,\mathrm{U}_i^{\{1\}n+1}\Big/h_i^{n+1} \end{aligned} \tag{64}$$

The mixture mass numerical flux at the cell edge, $F_i^{\{1\}\downarrow -} = F_j^{\{1\}\downarrow +} = (\mathrm{rh}\widehat{u})_k^{\downarrow}$ (52), is used to compute the volume numerical flux of each pth solid phase at the kth edge $(h\widehat{u}\varphi_p)_k^{\downarrow}$ as:

$$\left(h\widehat{u}\varphi_p\right)_k^{\downarrow} = \begin{cases} \dfrac{(\mathrm{rh}\widehat{u})_k^{\downarrow}}{\widetilde{r}_k}\left(\varphi_p\right)_i^n & \text{if} \quad (\mathrm{rh}\widehat{u})_k^{\downarrow} > 0 \\ \dfrac{(r\widehat{hu})_k^{\downarrow}}{\widetilde{r}_k}\left(\varphi_p\right)_j^n & \text{if} \quad (r\widehat{hu})_k^{\downarrow} < 0 \end{cases} \tag{65}$$

and the volume fraction of the pth solid phase at the i cell is updated as follows:

$$(h\varphi_p)_i^{n+1} = (h\varphi_p)_i^n - \frac{\Delta t}{A_i}\sum_{k=1}^{\mathrm{NE}}(h\widehat{u}\varphi_p)_k^{\downarrow}\,l_k - \Delta t\,(D_p - E_p)_i^n \tag{66}$$

hence computing the volumetric concentration at the next time step as:

$$(\varphi_p)_i^{n+1} = (h\varphi_p)_i^{n+1}\Big/h_i^{n+1} \tag{67}$$

Furthermore, when the active layer approach is used to estimate the material entrainment from the bed layer, the mass conservation equation for the pth sediment class in the active layer (24) is discretized at the i cell as:

$$\frac{\left(f_{a,p}\eta_a\right)_i^{n+1} - \left(f_{a,p}\eta_a\right)_i^n}{\Delta t} + \left(f_{s,p}\right)_i^n\frac{(z_b - \eta_a)_i^{n+1} - (z_b - \eta_a)_i^n}{\Delta t} = \frac{\left(D_p - E_p\right)_i^n}{1 - p_p} \tag{68}$$

and, using $\sum_{p=1}^{N}(f_{a,p}\eta_a)_i^{n+1} = (\eta_a)_i^{n+1}$, allows to update the fraction of the pth sediment class in the active layer at the i cell to the next time $(f_{a,p})_i^{n+1}$.

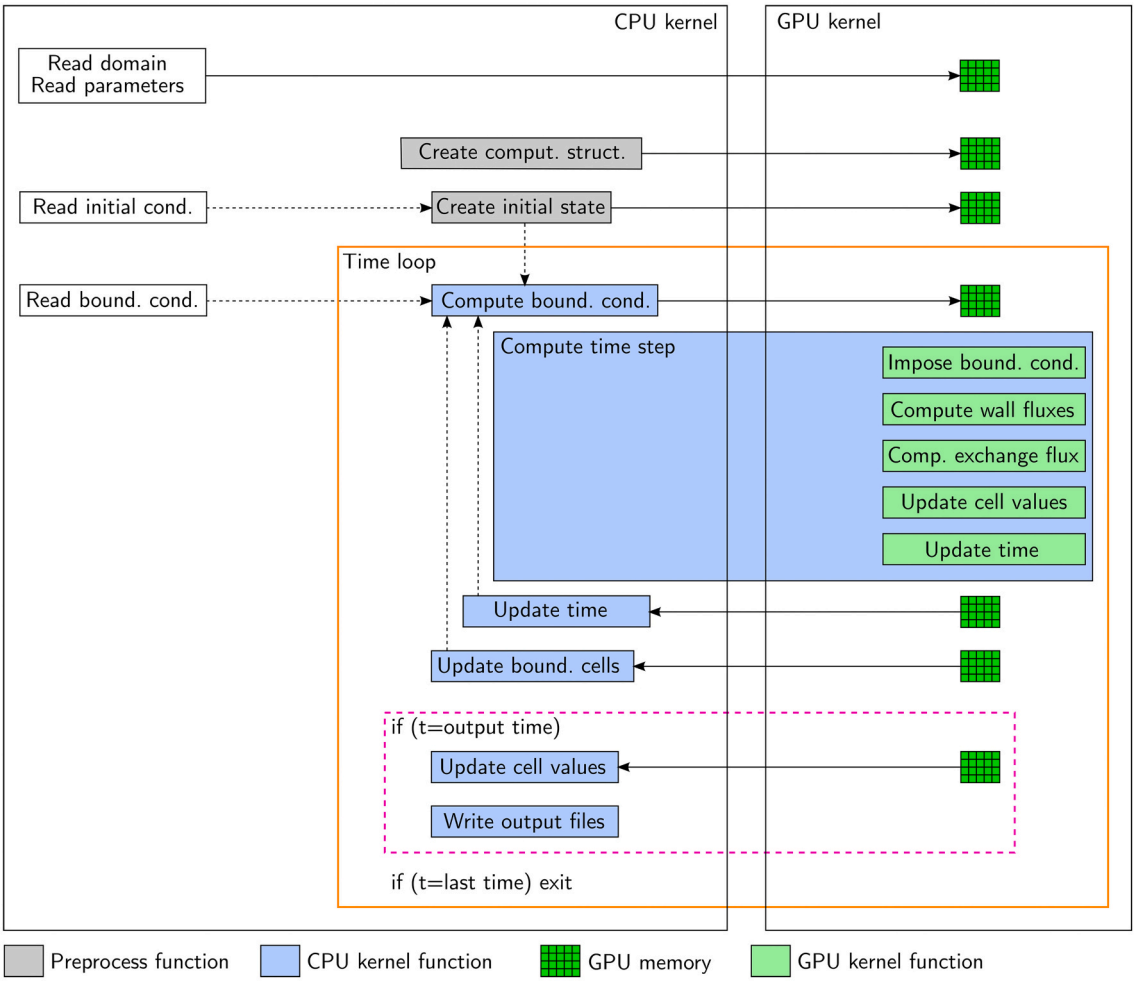

Fig. 2. Scheme of the GPU-accelerated algorithm.

4. GPU-accelerated algorithm

Due to the large computational effort required to solve this kind of problems when dealing with realistic spatial and temporal scales, a GPU-based algorithm has been implemented using the NVIDIA CUDA Toolkit. GPUs are oriented to perform arithmetical operations on vector-based information. Unlike the conventional CPU implementations, the GPU solution must be designed taking into account the fact that the GPU is an independent device with its own RAM memory. This means that the memory transfer between the conventional RAM memory and the GPU device memory plays a key role in the performance of GPU-accelerated software. The most common way of performing this memory transfer is by means of explicit memory copy operations in the code. In any case, if the algorithm requires a large number of transfers, the performance of the GPU solution may be dramatically reduced due to this separate memory space.

Fig. 2 shows a scheme of the GPU-based algorithm proposed for the above 2D model for mud/debris flows over erodible beds. The preprocess step and CPU-GPU memory transfer are implemented to run on one CPU core, whereas the time loop computation is accelerated using GPU. However, some tasks inside the time loop are controlled yet by the CPU, as the time advance control, the boundary conditions application and the output data dump. Therefore, it is necessary to transfer information from/to the GPU at each time-step. While the computational effort required for the time and boundaries transference is considerably smaller than that of each kernel function, in order to dump the intermediate output information all the variables in the domain must be transferred from GPU device to CPU host.

In order to obtain an efficient GPU-accelerated code dealing with unstructured meshes, some of the strategies proposed by Lacasta et al. (2014) and Lacasta et al. (2015) have been implemented. The CUDA toolkit allows that all the processed elements can be distributed by threads and blocks of threads. Each thread uses its own thread index to identify the element to be processed, launching several execution threads at the same time (parallel computation). As computing GPU devices are well designed to work efficiently with ordered information, the variables needed for computation are stored in the GPU memory as structures of arrays (SoA), improving the spatial locality for memory accesses. Only the kernel functions which require a higher computational effort have been implemented to run on the GPU device. Some tasks in the GPU kernel are optimized using the CUBLAS library included in CUDA. The memory transfer between the CPU host and the GPU device has been reduced as much as possible for each time step.

Finally, in order to compare the computational requirements of the CPU-based and the GPU-based version of the algorithm, it is worth noting that all the tests presented in this work using the CPU-based version of the code were run on a Intel(R) Core(TM) i7-3820 @3.60GHz and a last generation Intel(R) Core(TM) i7-7700K @4.50GHz, whereas the GPU-based code was tested using two devices: a medium-grade NVIDIA Tesla K40c and a NVIDIA GeForce GTX 1080 Ti. GPU's technology is continuously growing and the devices are fastly improving regarding the number of computation cores, speed on the data transfer and efficiency of the CUDA Toolkit. Therefore, it is expected that the performance of the GPU-accelerated algorithm may

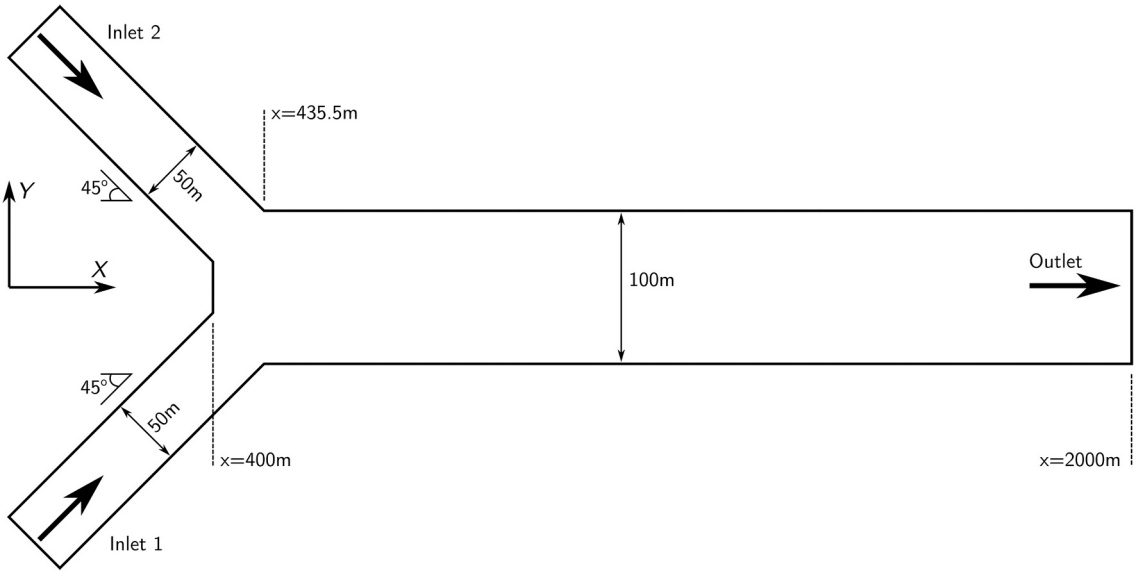

Fig. 3. Synthetic test A: sketch of the geometrical configuration.

Table 2
Parameters for the synthetic test A.

Liquid density ρ_w	1000 kg/m^3
Number of solid grain-classes N	1
Solid density ρ_p	2700 kg/m^3
Grain diameter d_p	0.4 mm
Basal resistance	Pure turbulent (PT)
Manning's roughness parameter n	0.018 sm$^{-1/3}$

increase markedly running in last generation NVIDIA GPUs.

5. Numerical results

5.1. Synthetic tests

Due to the lack of experimental data for mud/debris flows, synthetic cases are first included in order to evaluate the basic performance of the proposed numerical approach.

5.1.1. Test A: mixing of two steady currents of different density over rigid bed

The main goal of this idealized test A is to assess the capability of the 2D FV scheme to correctly deal with mixing of flows with a different density. In cases where two steady currents of equal discharge and different density converge, the influence of the spatial density gradients should dominate the hydrodynamics of the mixing region (Lane et al., 2008; Gualtieri et al., 2019). This effect of the density gradients is only properly reproduced at the numerical level if the mixture density is taken into account in the eigenstructure of the Riemann solver at the cell edges. A symmetric confluence of two 565 m long and 50 m wide tributary channels into a main channels of length 1600 m and width 100 m is considered. The center axis of the tributary channels forms a 45° angle with the x axis. A uniform longitudinal bed slope $S_0 = 0.0025$ is set for the tributary and main channels. Fig. 3 shows a plane view of the test geometry.

The setup parameters for the synthetic test A are summarized in Table 2. The entrainment term is neglected, avoiding erosion and deposition, and the basal shear stress is estimated using only the turbulent and dispersive effects using the PT formulation (see Table 1). The selected value of Manning's roughness coefficient allows the flow to reach slight supercritical uniform regimes ($S_0 = S_f$) along both the tributary and main channels. The spatial domain is discretized using an unstructured triangular mesh with 23500 cells approximately. The simulation starts form dry bed conditions and the CFL is set to 0.95. The simulation runs in a NVIDIA Tesla K40c device.

Constant discharge inflows $q_{inlet} = 10$ m^2/s per unit width are set at both inlets 1 and 2 during the whole simulation time ($t_{end} = 240$ min). The temporal evolution of the solid phase volumetric concentration at inlet 1 φ^1_{inlet} remains null, whereas at inlet 2 the solid phase volumetric concentration φ^2_{inlet} varies with time following:

$$\text{Inlet1}: \begin{cases} q^1_{\text{inlet}} = 10\,\text{m}^2/\text{s} & \text{for } 0 \le t \le 240\,\text{min} \\ \varphi^1_{\text{inlet}} = 0.0 & \text{for } 0 \le t \le 240\,\text{min} \end{cases}$$

$$\text{Inlet2}: \begin{cases} q^2_{\text{inlet}} & 10\,\text{m}^2/\text{sfor } 0 \le t \le 240\,\text{min} \\ \varphi^2_{\text{inlet}} & \begin{cases} 0.0 & \text{if } 0 \le t \le 60\,\text{min} \\ 0.3/60(t-60) & \text{if } 60 \le t \le 120\,\text{min} \\ 0.3 & \text{if } 120 \le t \le 240\,\text{min} \end{cases} \end{cases}$$

leading to a constant value of the inflow mixture density $\rho = 1510$ kg/m^3 for inlet 2 at $t \ge 120$ min. Only the specific mass flow rate is imposed at the inlet boundary. The value of the flow depth, and corresponding flow velocity, is computed by the numerical scheme applied at the boundary cell, but not directly imposed. At $t = 60$ min a symmetric confluence state is expected, whereas for larger times the density gradients should change the flow configuration at the confluence region, reaching a new non-symmetric steady state at $t = 240$ min.

Fig. 4 shows (a) the flow depth and (b) the Froude number contour levels for the steady state reached at $t = 60$ min. The flow at both the tributary channels and the main channel is slightly supercritical, however the mixing of both flows at the confluence region creates a subcritical flow zone which propagates upstream creating hydraulic jumps in the tributary channels. As at this time $t = 60$ min the inlet density of both flows is equal ($\rho = 1000$ kg/m^3), the wave-structure in the tributary channels and in the main channel is totally symmetric.

From this steady state, the inflow solid phase concentration is linearly increased at inlet 2 to a value of 0.3 at $t = 120$ min. The symmetric structure in the confluence region is broken due to the higher momentum term of the denser inflow 2. Fig. 5 shows (a) the flow depth and

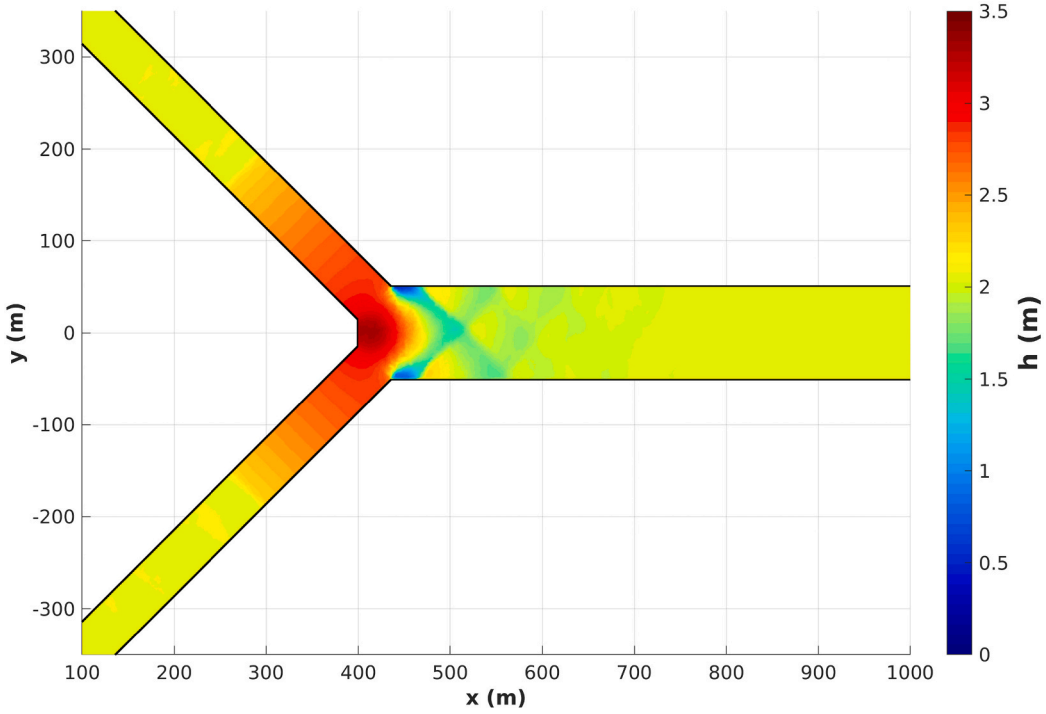

(a)

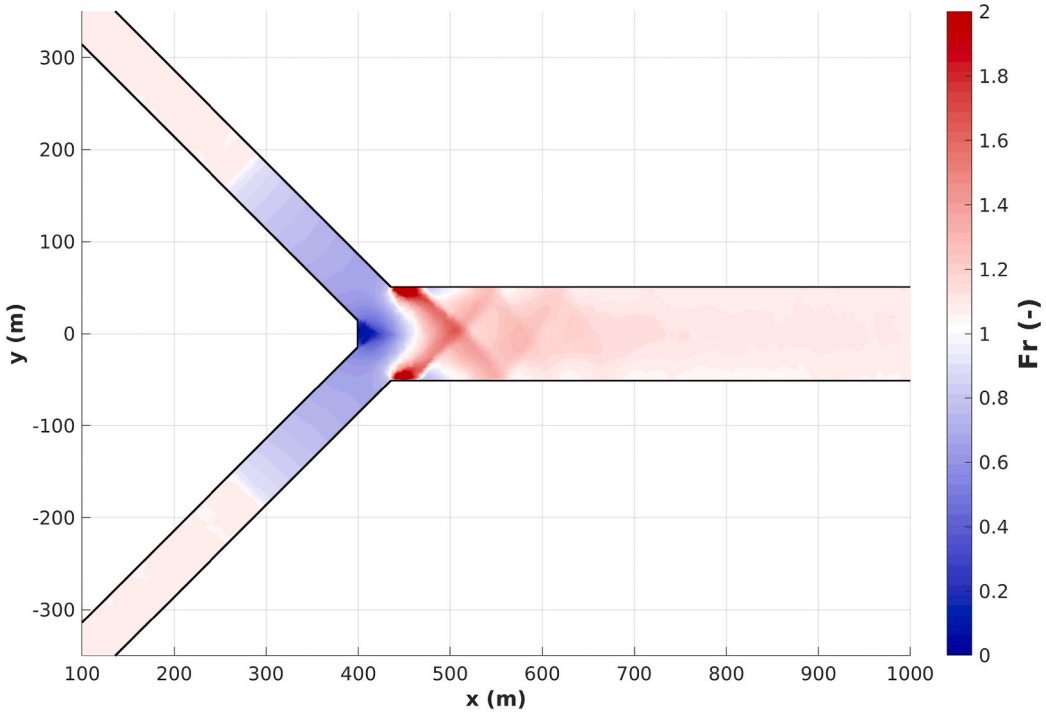

(b)

Fig. 4. Synthetic test A: steady state at $t = 60$ min: (a) flow depth and (b) Froude number.

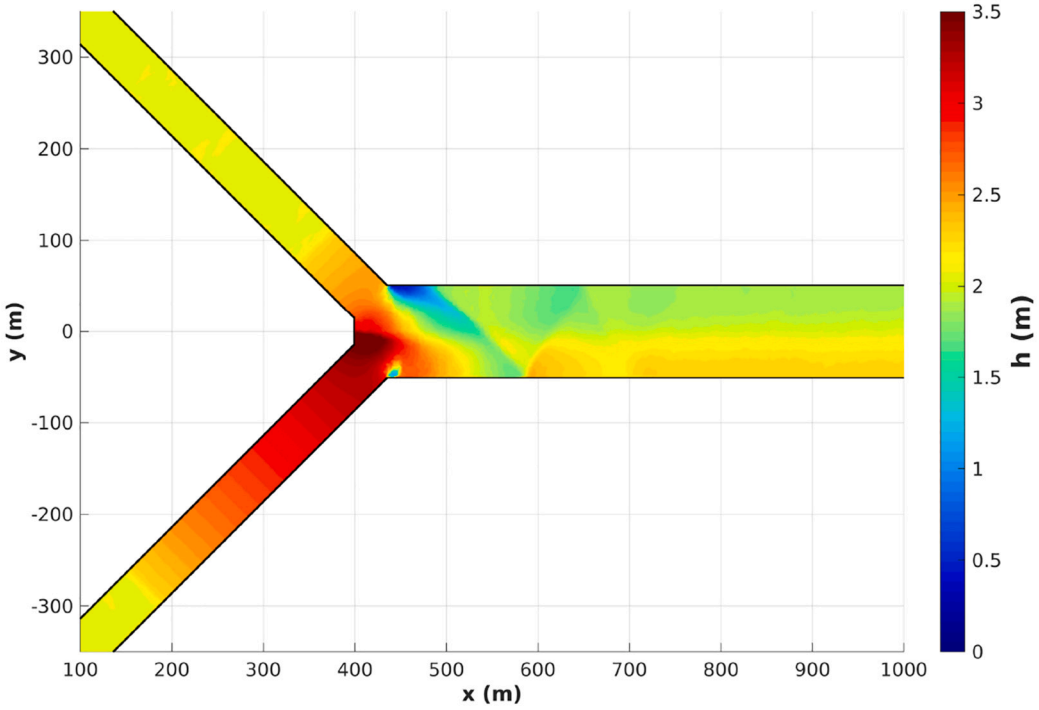

(a)

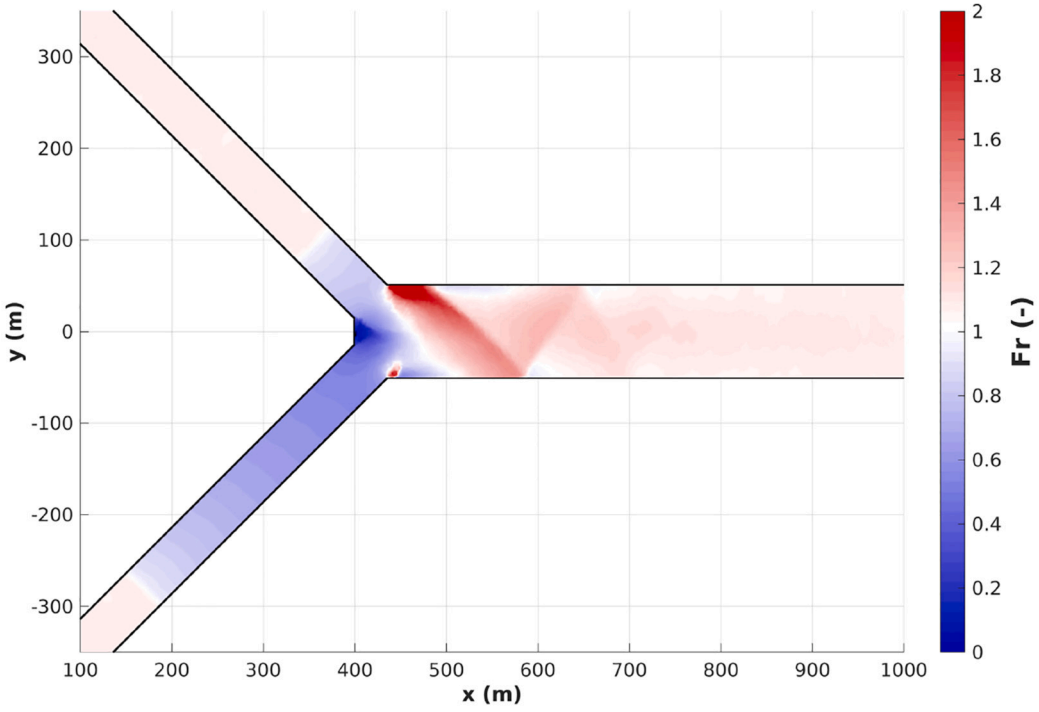

(b)

Fig. 5. Synthetic test A: steady state at $t = 240$ min: (a) flow depth and (b) Froude number.

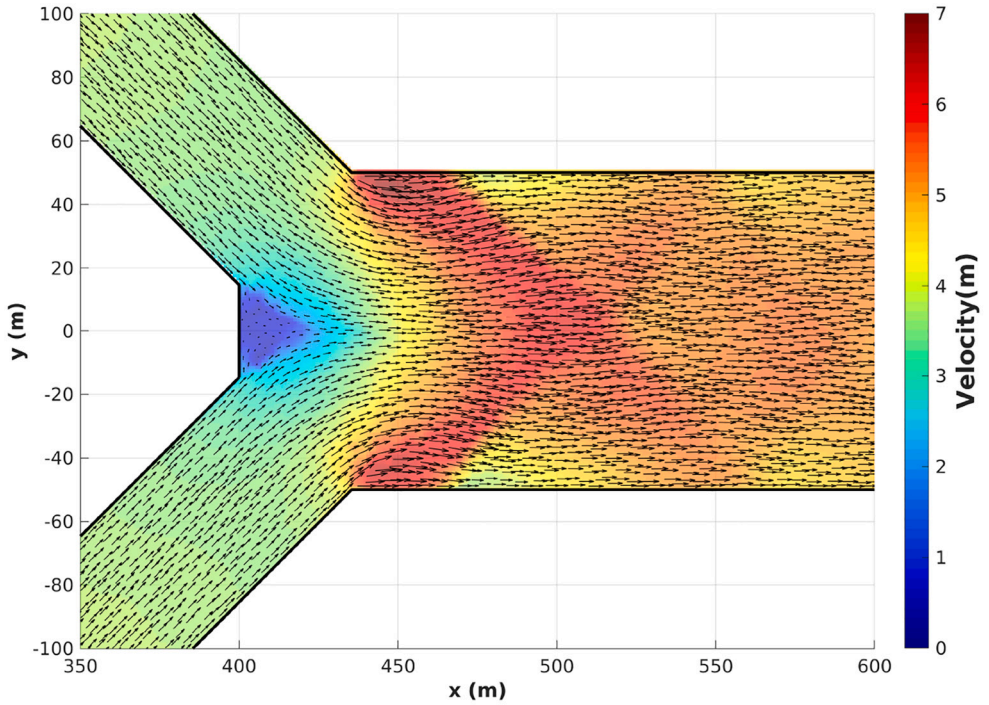

(a) $t = 60\,min$

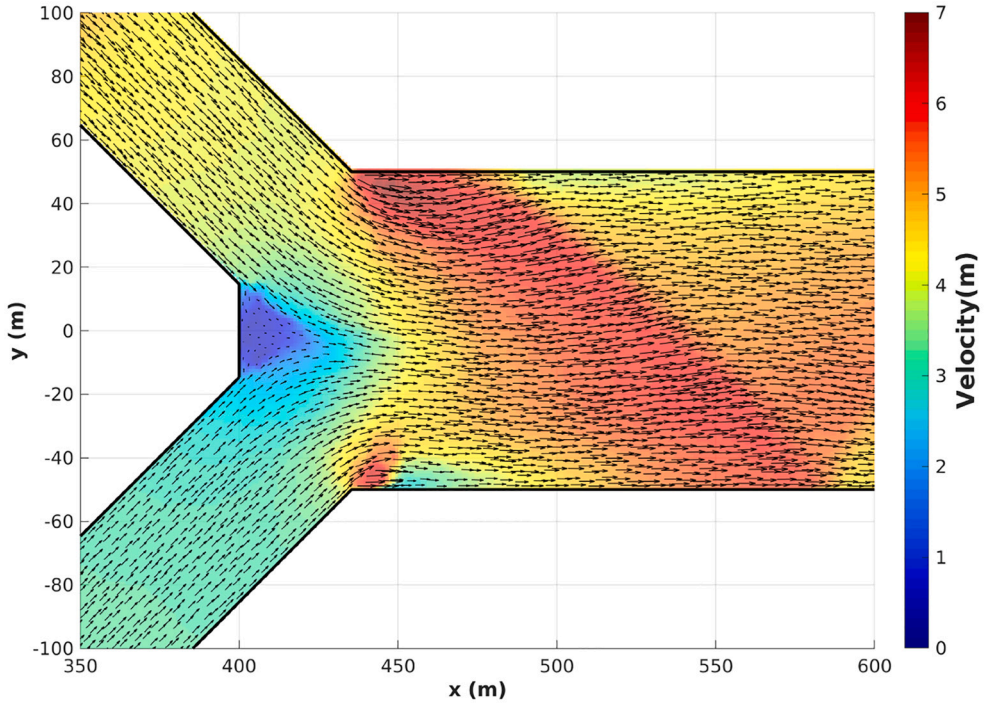

(b) $t = 240\,min$

Fig. 6. Synthetic test A: 2D velocity fields at (a) $t = 60$ min and (b) $t = 240$ min.

(b) the Froude number contour levels for the new steady state reached at $t = 240$ min. The hydraulic jump created by the presence of the confluence in the tributary channel 2 moves downstream whereas the hydraulic jump in the tributary channel 1 moves upstream. Furthermore, the wave-structure downstream the confluence in the main channel shows also a non-symmetric configuration, following a sequence of alternative diagonal shock waves.

This behavior is directly caused by the inclusion of the density into

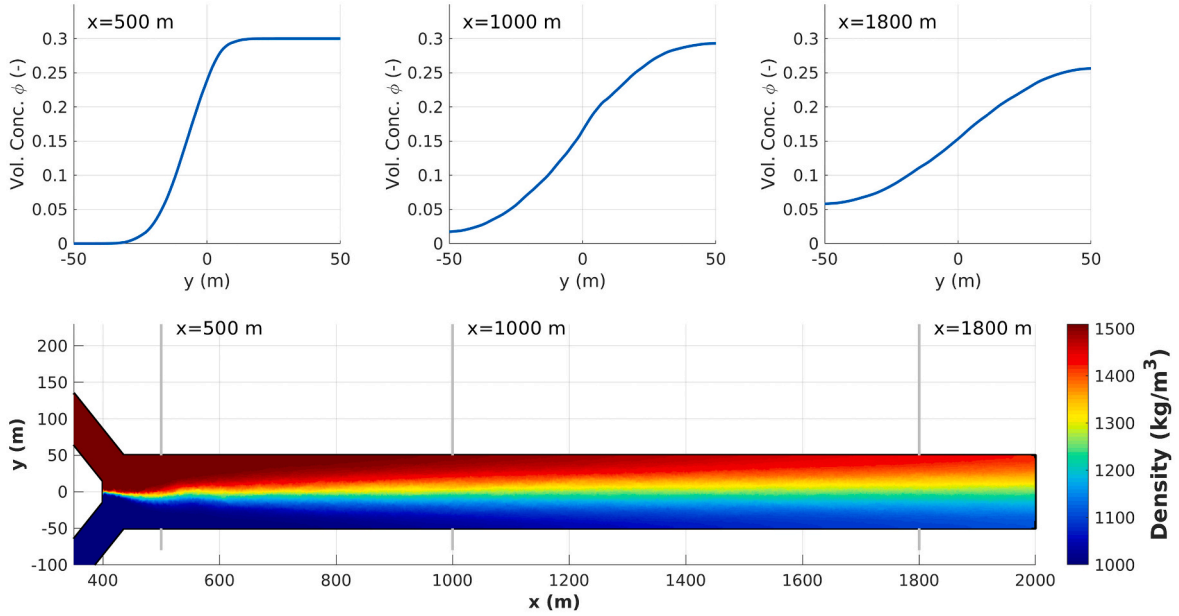

Fig. 7. Synthetic test A: flow density along the main channel at $t = 240$ min and cross-section profiles for the sediment volumetric concentration at $x = 500$ m, $x = 1000$ m and $x = 1800$ m.

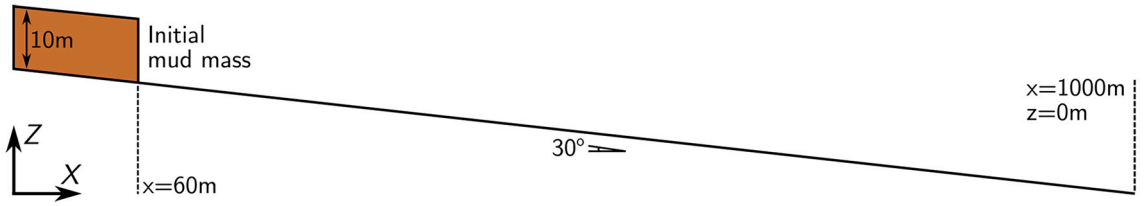

Fig. 8. Synthetic test B: sketch of the geometrical configuration.

the conserved variables and convective fluxes in the Riemann solver. Spatial density gradients modify the celerity of the characteristic waves in the approximated solution, leading to a more realistic behavior of the scheme. This modification of the waves celerity can not be achieved by models which do not consider density into the homogeneous part of the system of conservation laws for highly sediment-laden flows (Murillo and García-Navarro, 2012; Ouyang et al., 2015a; Cao et al., 2017).

Fig. 6 depicts a zoom view of the steady state velocity fields within the confluence region at (a) $t = 60$ min (same density flows) and (b) $t = 240$ min (different density flows). The symmetric velocity pattern created with the same density flows configuration is broken when the density of inflow 2 increases, leading to higher velocities at the tributary channel 2 than those at the channel 1 and altering the symmetric velocity patterns in the main channel downstream the confluence.

Finally, Fig. 7 shows the mixing process along the main channel at $t = 240$ min. The mass and momentum exchange between different density flows tends to create a uniform cross-section density profile downstream the confluence region. At $x = 500$ m, a clear interface separating the high denser flow from the clear water current appears. This interface is less marked at $x = 1000$ m as a consequence of the mixing process whereas it practically disappears at $x = 1800$ m, although a uniform cross-section volumetric concentration profile has not been reached yet.

5.1.2. Test B: bed entrainment on mud/debris flows moving over downward slopes

The aim of the synthetic test is to assess the influence of the bed entrainment in the flow dynamics when a mud/debris mass moves along a steep downward slope. Fig. 8 shows a sketch of the test geometrical configuration. A 1000 m long and 10 m wide channel is considered with a uniform positive bed slope $S_0 = 0.58$ (30°). The setup parameters for the synthetic test B are summarized in Table 3. The bed layer is fully erodible and composed by a uniform sediment. An initially static 600 m^3 mud volume is considered between $x = 0$ m and $x = 60$ m with a uniform depth of 10 m over the channel bed. The initial mud fluid consists of a mixture of water with a solid volumetric concentration of $\varphi_p = 0.60$, leading to a mixture density $\rho = 2020$ kg/m^3.

Table 3
Parameters for the synthetic test B.

Liquid density ρ_w	1000 kg/m^3
Number of solid grain-classes N	1
Solid density ρ_p	2700 kg/m^3
Grain diameter d_p	0.4 mm
Initial solid concentration φ_p	0.60
Basal resistance	Turbulent & Coulomb (TC)
Basal friction angle ϕ_b	22°
Basal pore pressure coefficient γ_{pp}	1.0
Manning's roughness parameter n	0.018 sm$^{-1/3}$
Bed porosity	0.25
Critical Shields stress $\theta_{c,p}$	0.030
Transport capacity modification parameter β_T	1.0

In order to assess the influence of the entrainment term in the flow dynamics, two simulations have been performed neglecting and considering the bed-flow exchange flux, i.e. avoiding and allowing erosion/deposition respectively. The TC formulation is selected to estimate the basal shear stress (see Table 1), considering hydrostatic pore-

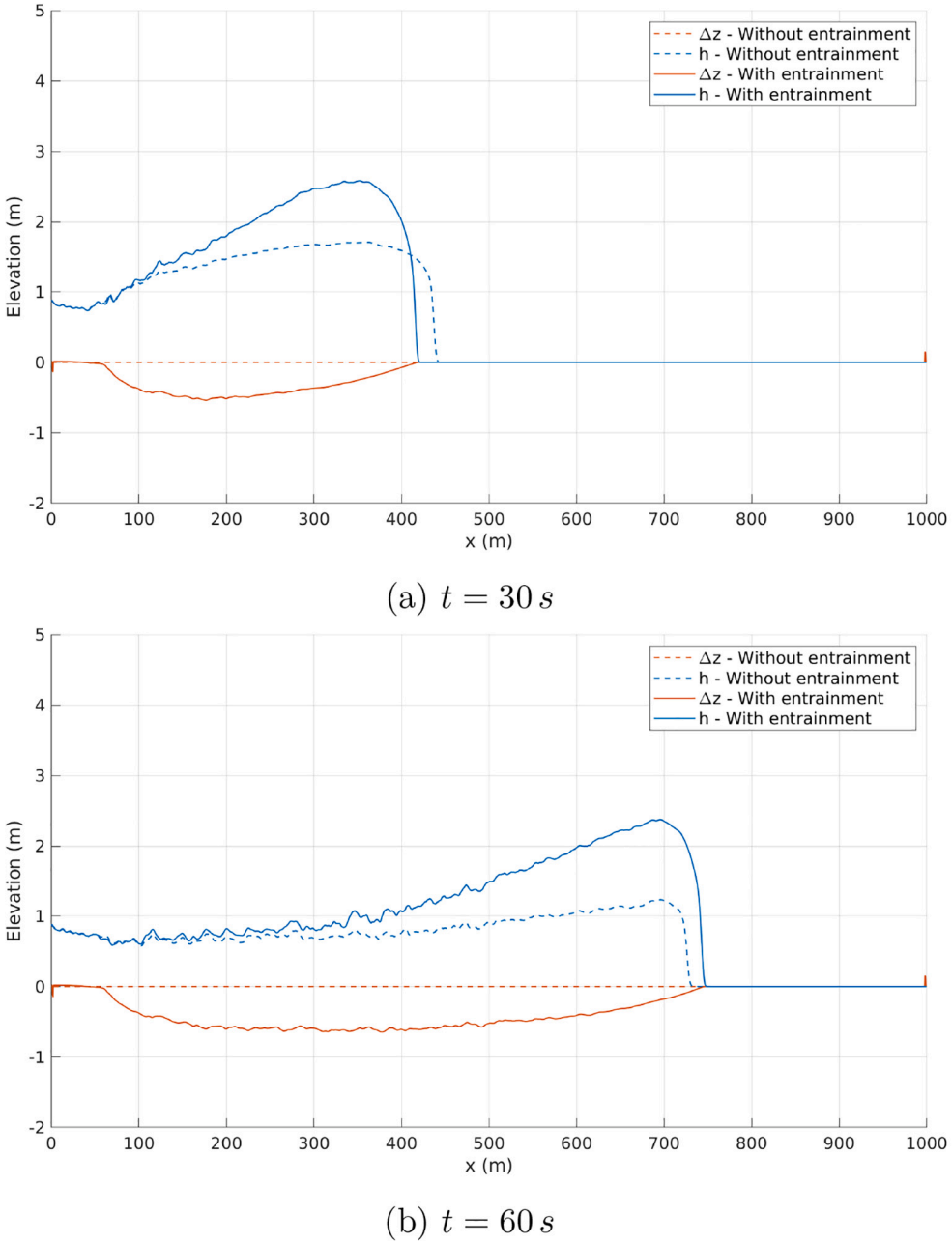

Fig. 9. Synthetic test B: flow depth and bed erosion at (a) $t = 30$ s and (b) $t = 60$ s, with and without considering bed entrainment.

fluid pressure. The spatial domain is discretized using an unstructured triangular mesh with 16400 cells approximately. The simulation time is 60 s from the mud mass release and the CFL is set to 0.95. The simulation runs in a NVIDIA Tesla K40c device.

Fig. 9 depicts the flow depth and bed level degradation longitudinal profiles at (a) $t = 30$ s and (b) $t = 60$ s after the mud mass release, with and without considering the bed entrainment term. During the movement, the entrainment from the bed layer enhances the volume involved in the flow, increasing the height of the mud wave. This is one of the main effects that has been observed in large-scale debris experiments (Iverson et al., 2011) and real mud/debris events (Jakob and Hungr, 2005). However, at the first stages of the flow movement, part of the flow momentum is spent on accelerating the mass incorporated from the static bed. This momentum waste leads to lower velocities of the mud and hence the wave-front location shows a delay respect to the wave-front location when the entrainment term is neglected at $t = 30$ s. However, as the mud wave moves downstream, the mass increment leads to an associated momentum enhancement and the wave-front progresses faster than when the entrainment is neglected (see Fig. 9b).

The change in the mud velocity caused by the entrainment term is clearly shown in Fig. 10(a), where the flow velocity longitudinal profiles are depicted considering and neglecting the bed exchange flux. The velocity along the mud wave is slightly lower at $t = 30$ s when the entrainment from the erodible bed is considered but also shows a marked enhancement at $t = 60$ s respect to the non-erodible bed case, leading to the acceleration of the wave-front advance. The entrainment term causes that at $t = 60$ s the velocity magnitude is of the same order as that at $t = 30$ s, whereas, when non-erodible bed is considered, the velocity magnitude is progressively reduced as the flow moves downstream. This fact contributes directly in the large runout distances observed in mud/debris flows.

Furthermore, one of the causes of this behaviour is directly related to

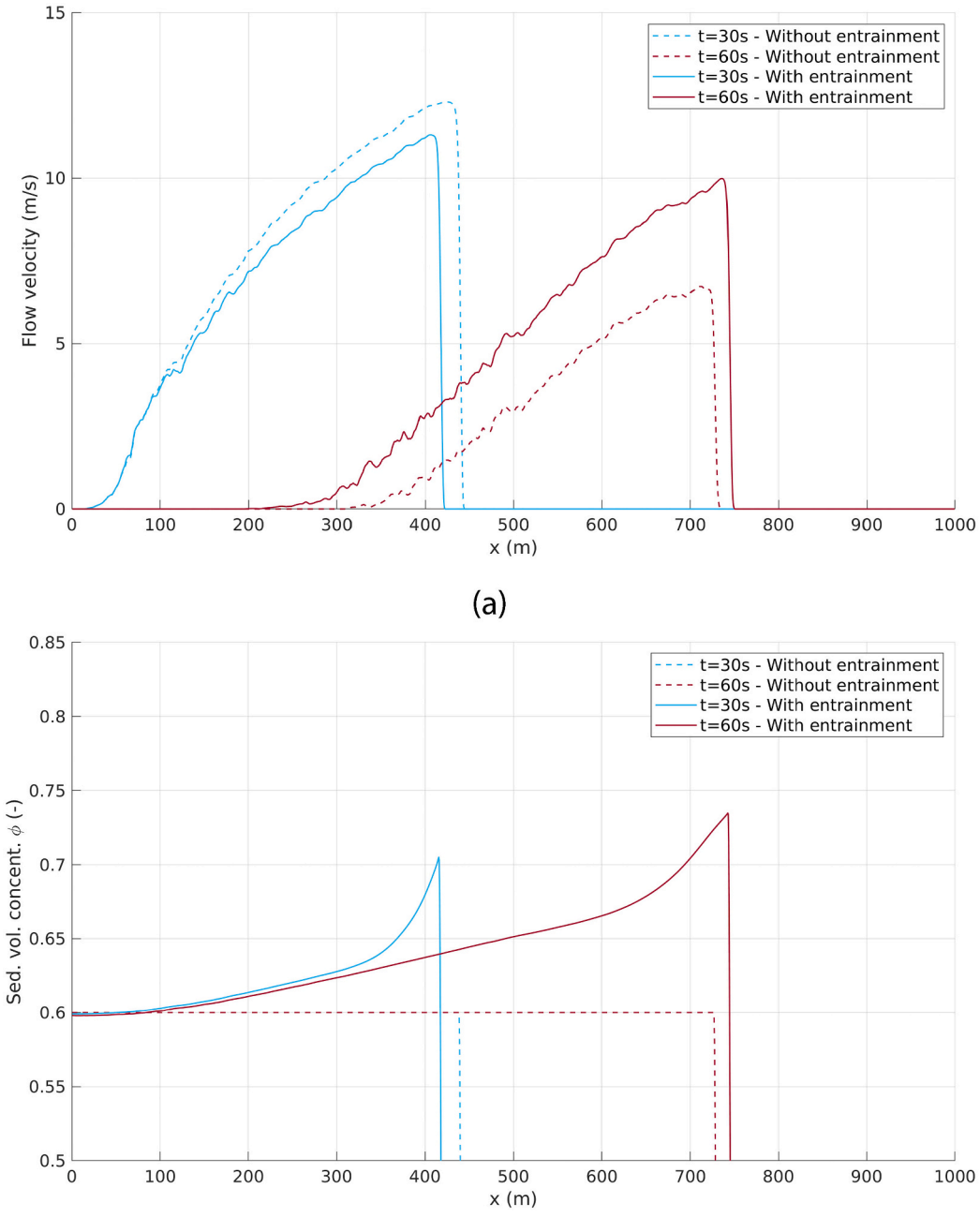

Fig. 10. Synthetic test B: (a) flow velocity and (b) sediment volumetric concentration at $t = 30$ s and $t = 60$ s, with and without considering bed entrainment.

the solid phase spatial distribution along the flow. Fig. 10(b) shows the sediment volumetric concentration longitudinal profile at $t = 30$ s and $t = 60$ s after the mud mass release, with and without considering the entrainment term. When the bed is considered non-erodible, the sediment concentration remains constant along the flow as a consequence of the equal velocity assumption for the liquid and solid phases adopted in the model. Nevertheless, when the entrainment is allowed, the solid concentration at the wave head is progressively increased as the flow moves downstream. A direct effect of that is the entrainment rate decrease as the flow increases its solid concentration, reducing the bed degradation and the momentum spent on accelerating the incorporated bed material. This fact contributes to the maintenance of the flow velocity magnitude as the flow moves downstream.

5.1.3. Test C: entrainment on mud/debris flows over non-uniform bed

In order to assess the effects of the active layer approach (23)–(24) for the estimation of the specific entrainment of each sediment class E_p when dealing with non-uniform beds, the above test B is repeated here but considering a non-uniform bed composed of two different sediment classes. The initial features of the flow and the non-uniform bed are summarized in Table 4. Note that the initial fraction distribution at the flow and bed layers is symmetric for both sediment classes considered in order to quantify the particle size effects on the active layer evolution.

Two simulations have been performed: one using the fixed-fraction approach and another using the active layer formulation, i.e. allowing the active layer composition to evolve with time. For the fixed-fraction approach, the hiding/exposure effects on the incipient motion critical Shields stress $\theta_{c,p}$ for each sediment class are estimated applying the Egiazaroff's (Egiazaroff, 1965) formula to a bulk critical Shields $\theta_c = 0.030$. The TC formulation is selected to estimate the basal shear stress with the same parameters as in the previous testB (see Table 1). The spatial domain is discretized using an unstructured triangular mesh

Table 4
Parameters for the synthetic test C.

Liquid density ρ_w	1000 kg/m^3	
Solid grain-classes N	2	
Sed. class	1 (coarse)	2 (fine)
Solid density ρ_p	2700 kg/m^3	2700 kg/m^3
Grain diameter d_p	0.6 mm	0.2 mm
Initial solid concentration φ_p	0.3	0.3
Initial bed fraction $F_{b,p}$	0.5	0.5
Bed porosity p_p	0.25	0.25
Friction angle $\phi_{b,p}$	40°	40°
Critical shields stress $\theta_{c,p}$	0.023	0.051
Transport capacity modification parameter β_T	1.0	
Active interface weighted parameter β_a	0.7	

with 16400 cells approximately. The simulation time is 60 s from the mud mass release and the CFL is set to 0.95. The simulation runs in a NVIDIA Tesla K40c device.

Fig. 11 shows the dambreak wave evolution at times $t = 30$ s and $t = 60$ s with the fixed-fractions and the active layer approaches for the bed entrainment. The active layer approach leads to slightly lower net bed entrainment and, hence, reduces the bed degradation due to the hiding/exposure effects in the non-uniform bed layer.

The reduction on the bed entrainment caused by the active layer approach leads to slightly lower flow velocities as the dambreak wave moves downstream. Fig. 12(a) shows the flow velocity at $t = 30$ s and $t = 60$ s with the fixed-fractions and the active layer approaches for the bed entrainment. As the dambreak wave progresses and the material is incorporated from the bed into, the smaller entrainment rates estimated with the active-layer model lead to a slight reduction in the flow velocity, compared with that obtained with the fixed-fraction approach. Nevertheless, the bulk concentration $\varphi_0 = \varphi_1 + \varphi_2$ in the flow remains approximately the same regardless of the bed entrainment approach used, and only small differences are noticeable at the central reach of the dambreak wave (see Fig. 12(b)).

Analyzing the temporal evolution of the fractions in the active layer and the volumetric concentration in the flow allows to identify the influence of the active layer approach in the materials stratification. Fig. 13 shows fractions in the active layer (bottom panel) and volumetric concentration in the flow (top panel) at (left) $t = 30$ s and (right) $t = 60$ s, with both the fixed-fraction and the active layer approaches. First, note that, using the fixed-fraction approach, the active fraction remains constant and uniform during the simulation $f_{a,1} = f_{a,2} = 0.5$, as well as the areal exposure $A_{b,1} = A_{b_2} = 0.5$. At the tail region of the dambreak wave, the lower shear stresses in the flow allow the coarser sediment class 2 to settle faster than the finer sediment class 1. Therefore, the concentration in the flow column of the coarser class φ_1 reduces along the tail reach whereas its fraction in the active layer $f_{a,1}$ grows progressively. Contrarily, at the wave-front region, the higher flow velocity leads to a higher entrainment of the coarser sediment class 1 due to hiding/exposure effects, increasing its concentration φ_1 in the flow layer and reducing its fraction $f_{a,1}$ in the active layer along the wave-front.

It is worth noting that, despite the active layer approach affects both the bed entrainment and the sediment size distribution along the dambreak wave, two important features of the flow are not modified: first, the coarser sediment class predominates in the flow column at the wave-front, whereas the wave tail is characterized by a more balanced sediment class distribution; second, both the wave-front advance velocity and the runout distance are not significantly modified, even for this large-scale test.

5.2. USGS debris dambreak flows over erodible bed

In this section the model predictions are validated using data from large-scale experiments consisting on dambreak debris flows over erodible bed. Eight different experiments were carried out in the USGS large-scale debris-flow flume and reported by Iverson et al. (2011). For all the experiments carried out, Iverson et al. (2011) reported the wave-front location along time, the wave-front velocity at the end of the channel and the final volume eroded from the bed. Moreover, the flow thickness and bed deformation at different points were reported for two of the experiments. The USGS debris-flow flume is a rectangular concrete channel 95 m length, 2 m wide and 1.2 m deep with a vertical headgate placed 12.5 m downstream the channel beginning, which retains the static debris fluid until the experiment initial time. Fig. 14 shows a schematic representation of the USGS debris-flow flume. All the longitudinal distances s are referred to the headgate position taken along the experimental flume floor. The channel has an 31° uniform slope until $s = 74$ m, where the flume begins to flatten following a catenary curve and evolving to a 4° slope at $s = 82.5$ m. There, the flume debouches onto a 15 m long, 8 m wide and 2 . 4° slope concrete runout surface.

The features of the different solid phases presented in the initial

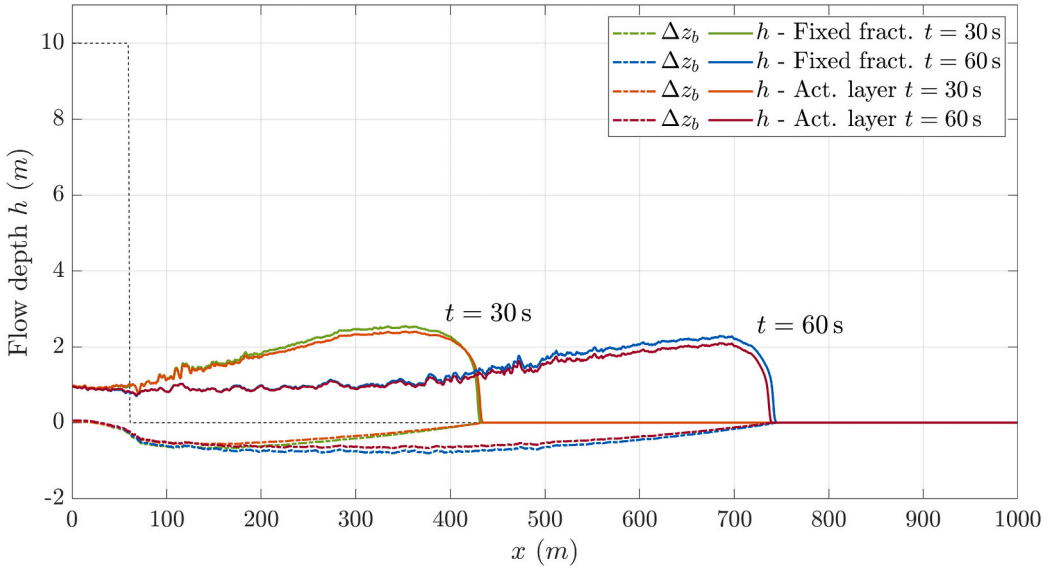

Fig. 11. Synthetic test C: bed and free surface levels at $t = 30$ s and $t = 60$ s, with fixed-fraction and active layer approaches for the bed entrainment.

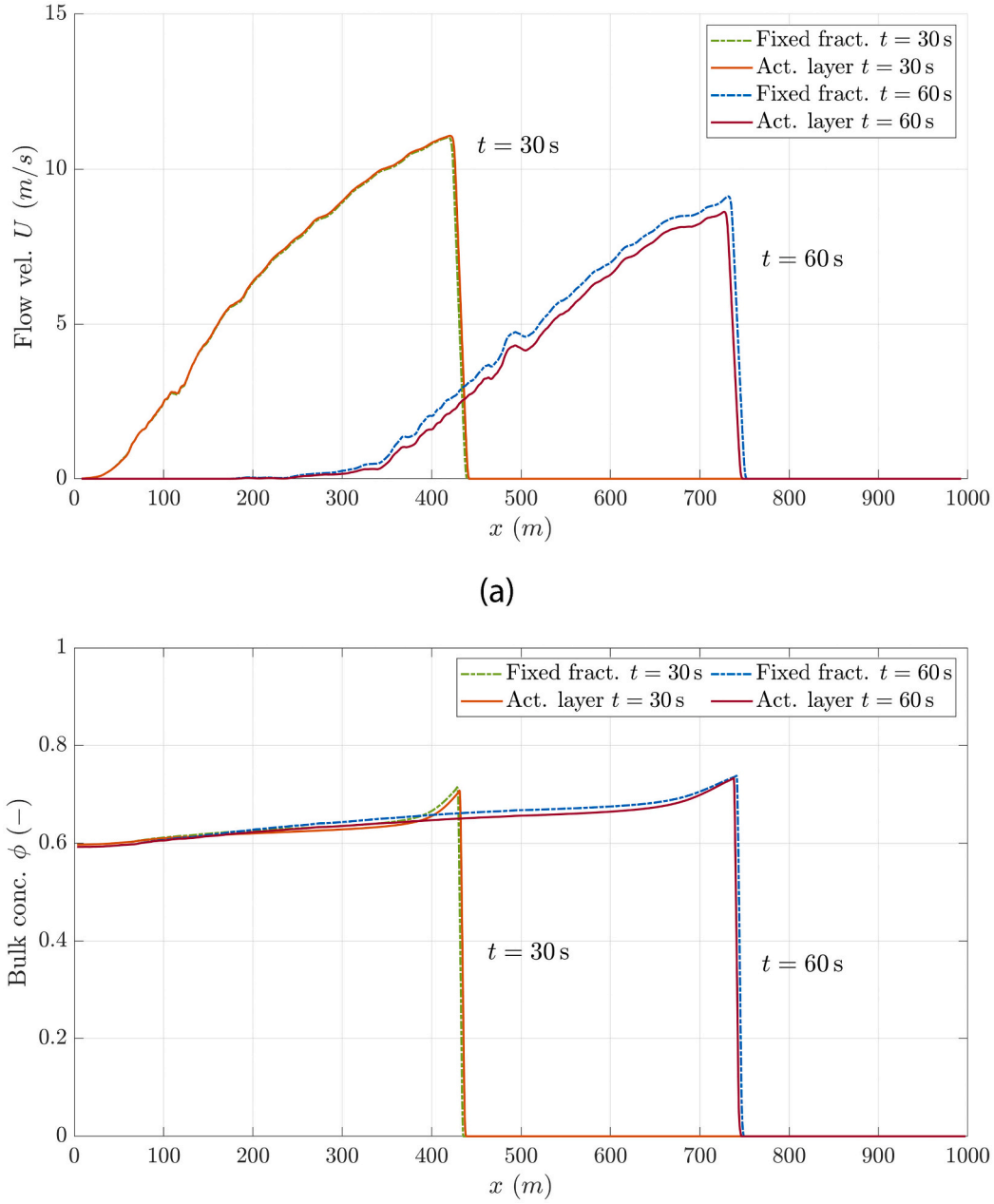

Fig. 12. Synthetic test C: (a) flow velocity and (b) sediment volumetric concentration at $t = 30$ s and $t = 60$ s, with fixed-fraction and active layer approaches for the bed entrainment.

debris mixture and the partially saturated bed were previously reported in Iverson et al. (2010). The initial debris volume is composed by a fully saturated mix of water and 56% gravel–37% sand–7% mud grains, called SGM mixture, where mud refers to particles smaller than 0.0625 *mm*. Table 5 shows the main parameter used in the simulations for characterizing the debris mixture. For all the experiments, the equivalent volumetric bulk concentration for the initial debris fluid is $\varphi_0 = 0.6$ ($r = 2.02$) and the initial volume stored upstream the headgate is 6 m^3. The flume floor is covered from $s = 6$ m to $s = 53$ m with a 12 *cm* thick layer of partially saturated SGM mixture. The porosity and water content of the erodible bed layer vary for each experiment, leading to different entrainment rates and wave-front velocities. In Table 6, the characteristics of each sediment size-class composing the SGM mixture have been summarized. For the sake of simplicity, and based on the results obtained in the above synthetic test C, the fixed-fraction approach is selected here for the computation of the specific bed entrainment. The hiding/exposure effects on the incipient motion critical Shields stress $\theta_{c,p}$ for each sediment class are estimated applying the Egiazaroff's (Egiazaroff, 1965) formula to a bulk critical Shields $\theta_c = 0.030$. Table 7 shows the bed water content $C_{w,p}$, the bed bulk porosity p_p and pore-fluid pressure coefficient γ_{pp} used in the simulations for each experiment. The simulations are performed using an unstructured triangular mesh of around 57000 cells, with an averaged area of 100 cm^2. The CFL is set to 0.95 and the total simulation time is $t_{end} = 25$ s for each experiment. Simulations are performed in a NVIDIA Tesla K40c device with the GPU-based code, whereas the Intel(R) Core (TM) i7-7700K @4.50GHz is used for the CPU-based algorithm.

Once the headgate was opened, the dam-break wave progressed over the erodible bed until it reached the runout surface where it stopped. For all the experiments, the wave-front position was tracked using image techniques and video frames. The wave-front velocity was also measured between $s = 60$ m and $s = 70$ m from the video frames. The

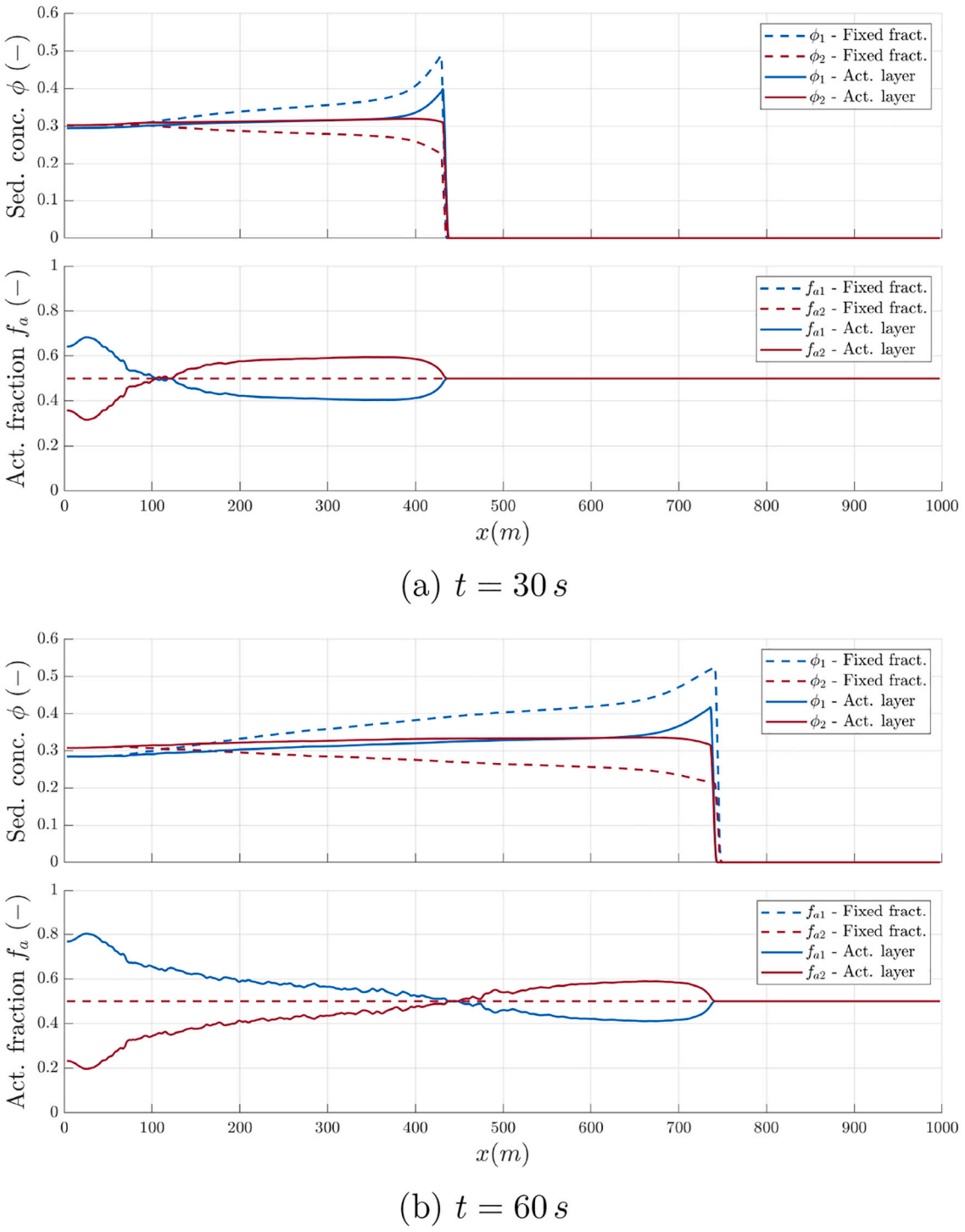

Fig. 13. Synthetic test C: (bottom panel) fractions in the active layer and (top panel) sediment volumetric concentration at (a) $t = 30$ s and (b) $t = 60$ s, with fixed-fraction and active layer approaches for the bed entrainment.

entrainment from the erodible bed to the debris flow was estimated by measuring the bed layer volume before and after the passage of the dambreak wave. The flow thickness was measured at the control sections P1 $s = 32$ m and P2 $s = 66$ m for the test G and C using laser sensors mounted above the flume. Furthermore, the bed degradation was also measured using scour sensor placed in the erodible bed at $s = 13$ m, $s = 23$ m, $s = 33$ m and $s = 43$ m for tests C and G.

A complete analysis of the numerical results obtained using different rheological formulations (see Table 1) to estimate the debris stresses is included herein for the tests C and G. Then, the results obtained by the rest of the experiments are also reported.

For test G, the lower part of each panel in Fig. 15 shows the bulk debris density in color scale and the upper part depicts the longitudinal profile of the specific volumetric concentration for each sediment class in the mixture at (a) $t = 6$ s and (b) $t = 18$ s after the gate opening and using the TC rheological relation. Note that the flow depth in the 3D figure is multiplied by 5 to improve the visualization of the debris wave shape. As the dambreak wave progresses downstream, bed material is

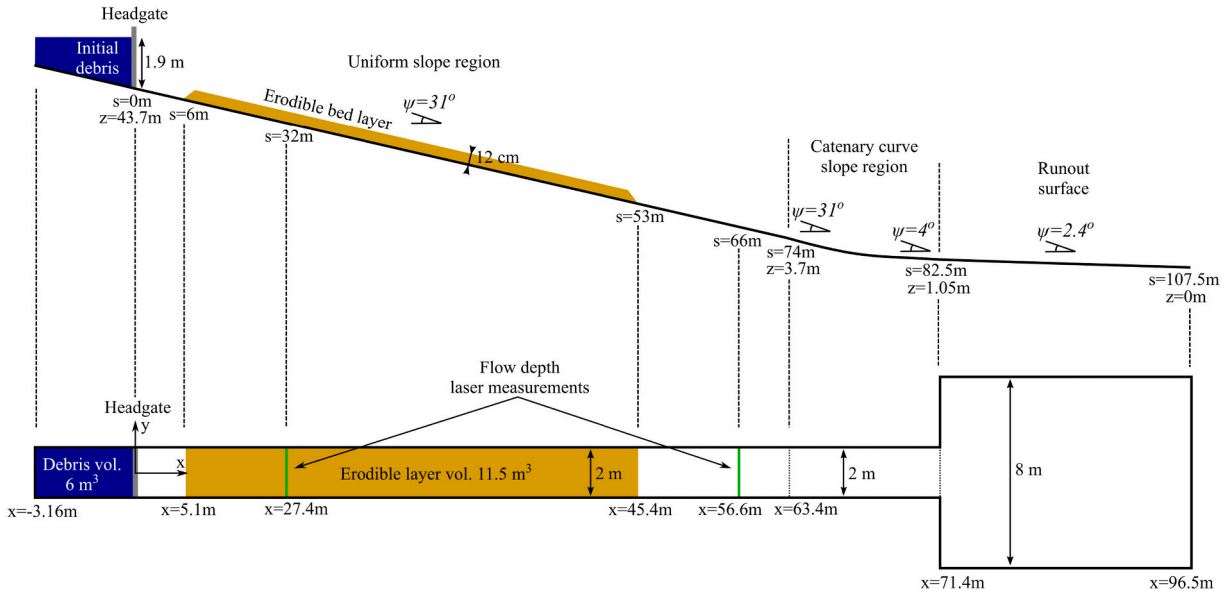

Fig. 14. Sketch of the USGS flume experiments. Details of the equivalent horizontal distance, vertical elevation and channel slope are also indicated.

Table 5
Parameters for the SGM mixture used in the simulations.

Liquid density ρ_w	1000 kg/m^3
Initial sediment concentration φ_0	0.60
Water content C_w	0.40
Initial debris density ρ	2020 kg/m^3
Plastic viscosity μ	1.66 Pa s
Yield stress τ_y	393 Pa
Internal stability angle ϕ_b	40°
Manning roughness coeff. n	Concrete: 0.018 s m$^{-1/3}$ Erodible layer: 0.021 s m$^{-1/3}$
Number of sediment size-classes	3
Transport capacity modification parameter β_T	0.3

Table 6
Features of the sediment size-classes composing the SGM mixture.

Sed. size-class	Fines	Sand	Gravel
Grain diameter d_p	0.016 mm	0.4 mm	12 mm
Solid density ρ_p	2700 kg/m^3	2700 kg/m^3	2700 kg/m^3
Initial vol. concentration φ_p	0.042	0.222	0.336
Friction angle $\phi_{b,p}$	40°	40°	40°
Critical Shields stress $\theta_{c,p}$	10.8575	0.4343	0.0212
Bed-flow exchange porosity p_p		Depends on the test	
Bed layer fraction $F_{b,p}$	0.07	0.37	0.56

Table 7
Features of the erodible bed layer used in the simulations.

Test	Bed water content $C_{w,p}$ (–)	Bed bulk porosity p_p (–)	Pore-fluid press. coeff. γ_{pp} (–)
A	0.282	0.51	1.70
B	0.257	0.46	1.67
C	0.253	0.48	1.65
D	0.244	0.43	1.62
E	0.227	0.39	1.60
F	0.220	0.43	1.58
G	0.183	0.42	1.56
D	0.148	0.49	1.55

incorporated into the flow, increasing the solid phase volume in the debris and hence its density. It is worth to mention that the coarse sediment fraction dominates along the front and central regions of the debris wave, whereas the finer sediment fraction shows higher concentrations along the tail zone. This sorting of the different solid phases in the flow mixture is typical of debris flow dynamics and is mainly caused by the differences on the solid phases velocity. However, the simplified model proposed in this work considers a unique velocity for all the solid phases. Therefore, this sorting of the sediment classes obtained by the numerical model, although correct, may be related to different bed entrainment rates for each sediment fraction from the bed.

The temporal evolution of the flow free surface at the control sections P1 ($s = 32$ m) and P2 ($s = 66$ m) with different rheological relationships for the basal resistance is depicted in Fig. 16 in comparison with the measured data. The wave-front arrival time to both control sections is reasonably well predicted using the TC formulation, as well as the peak of the free surface level corresponding to the wave head level. The SF formulation shows a smaller arrival time at both control sections, indicating higher flow velocities, whereas the wave head level is also well predicted. The SB and QD rheological formulations show higher free surface level peaks at the first control section P1, whereas they develop a double-wave flow structure at the second control section P2. The simulation performed using the CV relation correctly predicts the arrival time and wave head level at the first control section P1 but, for the second control section P2, the arrival time is larger and the peak of the free surface level higher than those observed in the experiment. The dambreak wave-front position is plotted against time in Fig. 17(a) for all the friction formulations simulated. The FB and SB formulations show higher wave-front velocities than those observed during the whole experiment, whereas the CV rheological relation predicts slower front velocities. The QD formula overestimates the wave-front velocity at the first stages but the runout distance is smaller than that measured in the experiment. Only the TC formulation is able to correctly estimate the wave-front advance process. Furthermore, during this experiment, bed degradation was not detected at any of the measurement section, indicating that the maximum scour depth was lower than 2 – 3 cm. Fig. 17 (b) shows the temporal evolution of the bed thickness at section P1 ($s = 32$ m) for all the friction formulations used. The deepest scour is computed using the TC relationship (3.2 cm) whereas the rest of basal

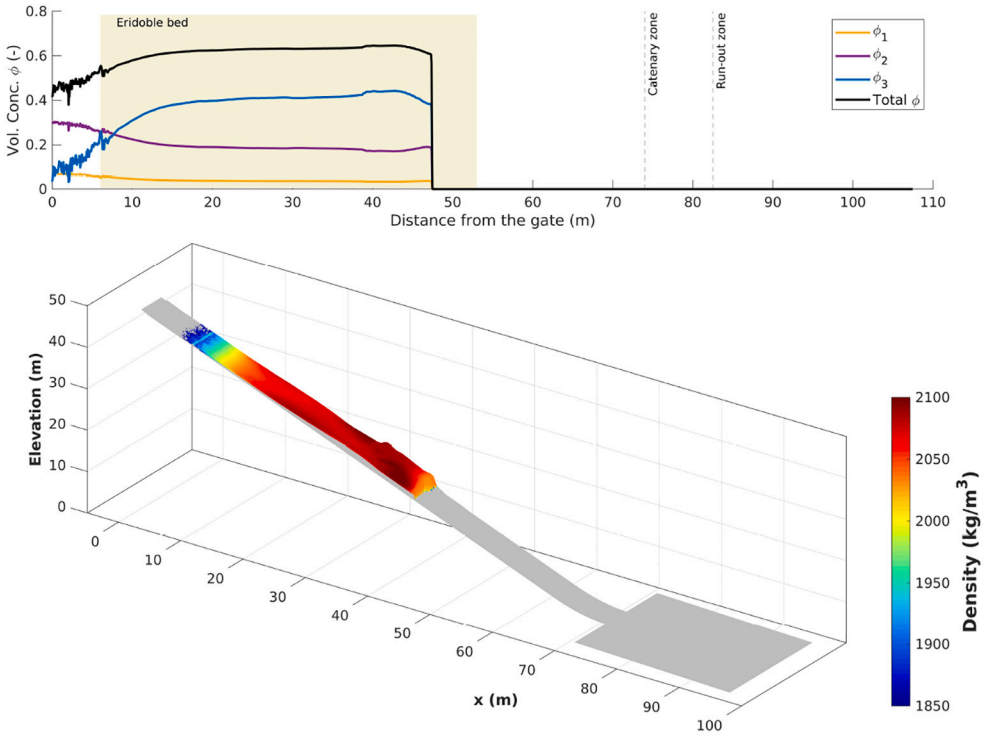

(a) $t = 6\,s$

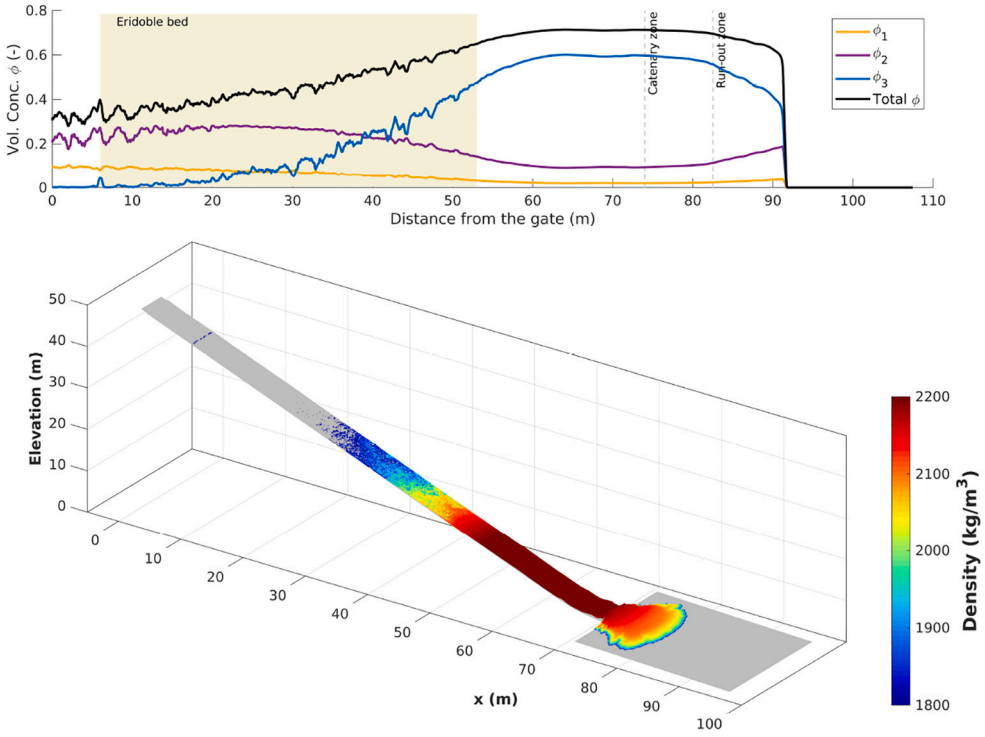

(b) $t = 18\,s$

Fig. 15. Test G: spatial flow distribution at (a) $t = 6$ s and (b) $t = 18$ s after the gate opening for test G and using the TC friction.

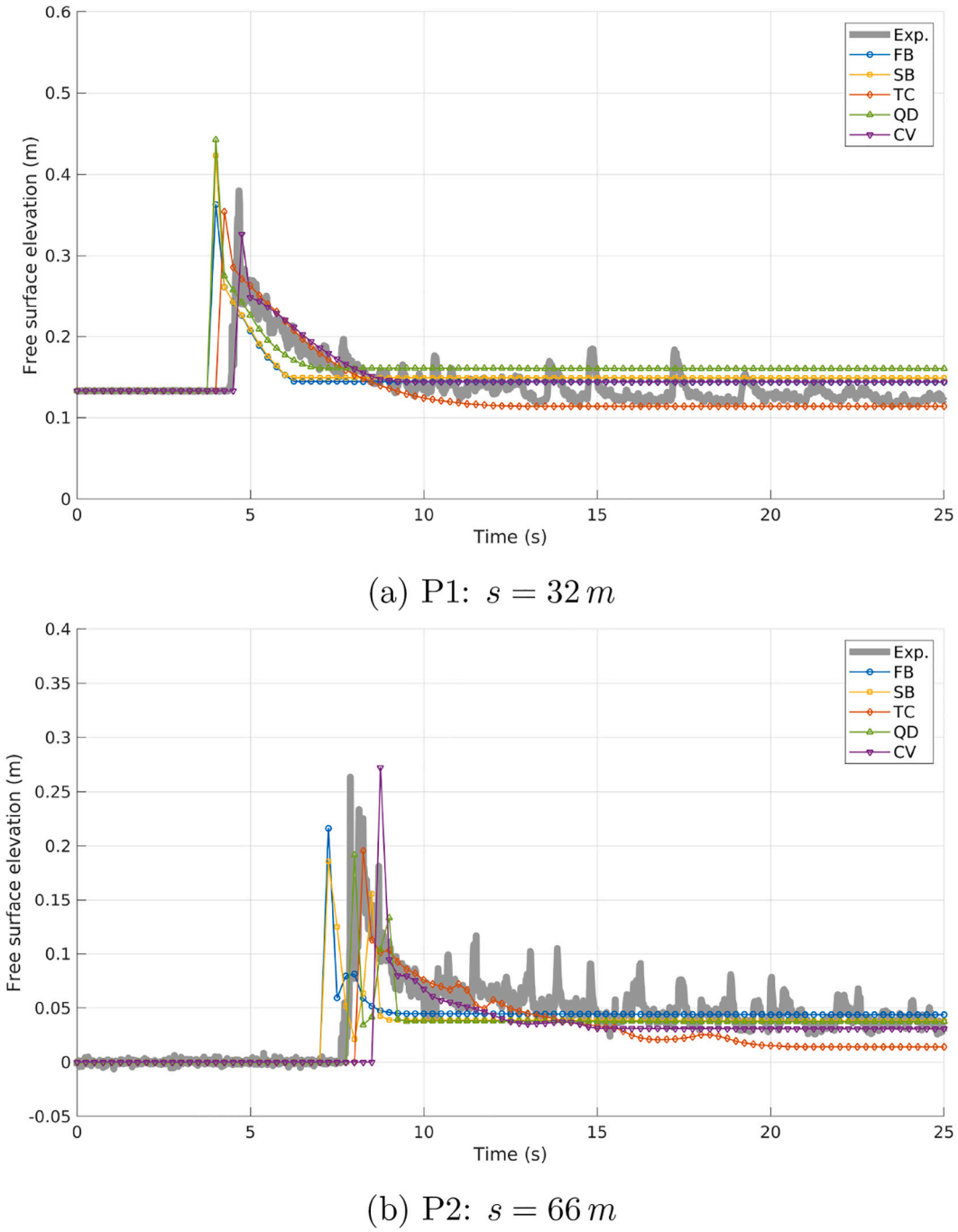

Fig. 16. Test G: temporal evolution of the flow free surface at (a) P1 and (b) P2 with different rheological relationships for the debris stress.

resistance formula predict bed scours lower than 2.4 cm. This is in agreement with the data measured during the experiment.

Table 8 shows the Root Mean Square Error (RMSE) for the flow free surface level at the control sections P1 ($s = 32$ m) and P2 ($s = 66$ m), as well as for the wave-front location, with the different rheological relationships simulated. The lowest RMSE is obtained with the CV formulation for the free surface level at the control section P1, whereas the TC relation shows the best results for both the free surface level at P2 and the temporal evolution of the wave-front location. The computational time required by the GPU-based algorithm to complete the simulation is also reported in Table 8 for all the rheological formulations, including the file input-output time. The computational effort is quite similar with all the debris stress relationships, with the exception of the TC formula which requires a larger time to complete the simulation.

Furthermore, the normalized wave-front speed between $s = 60$ m and $s = 70$ m, defined as $S = S_{measured}/9.81\ \mathrm{ms}^{-1}$, and the normalized post-entrainment flow volume, defined as $V = (6\ \mathrm{m}^3 + V_{eroded})/6\ \mathrm{m}^3$ is also computed for all the rheological relationships and compared with the measured data. Table 9 shows the computed results and the relative error with respect to those observed in the experiment. Although the best approximations to the measured wave-front speed S were obtained with the SB and CV formulations, also the TC and QD relations showed acceptable relative errors lower than 10%. Moreover, only the TC formulation reported a suitable approximation for the normalized post-entrainment volume V lower than 10% of the volume measured after the

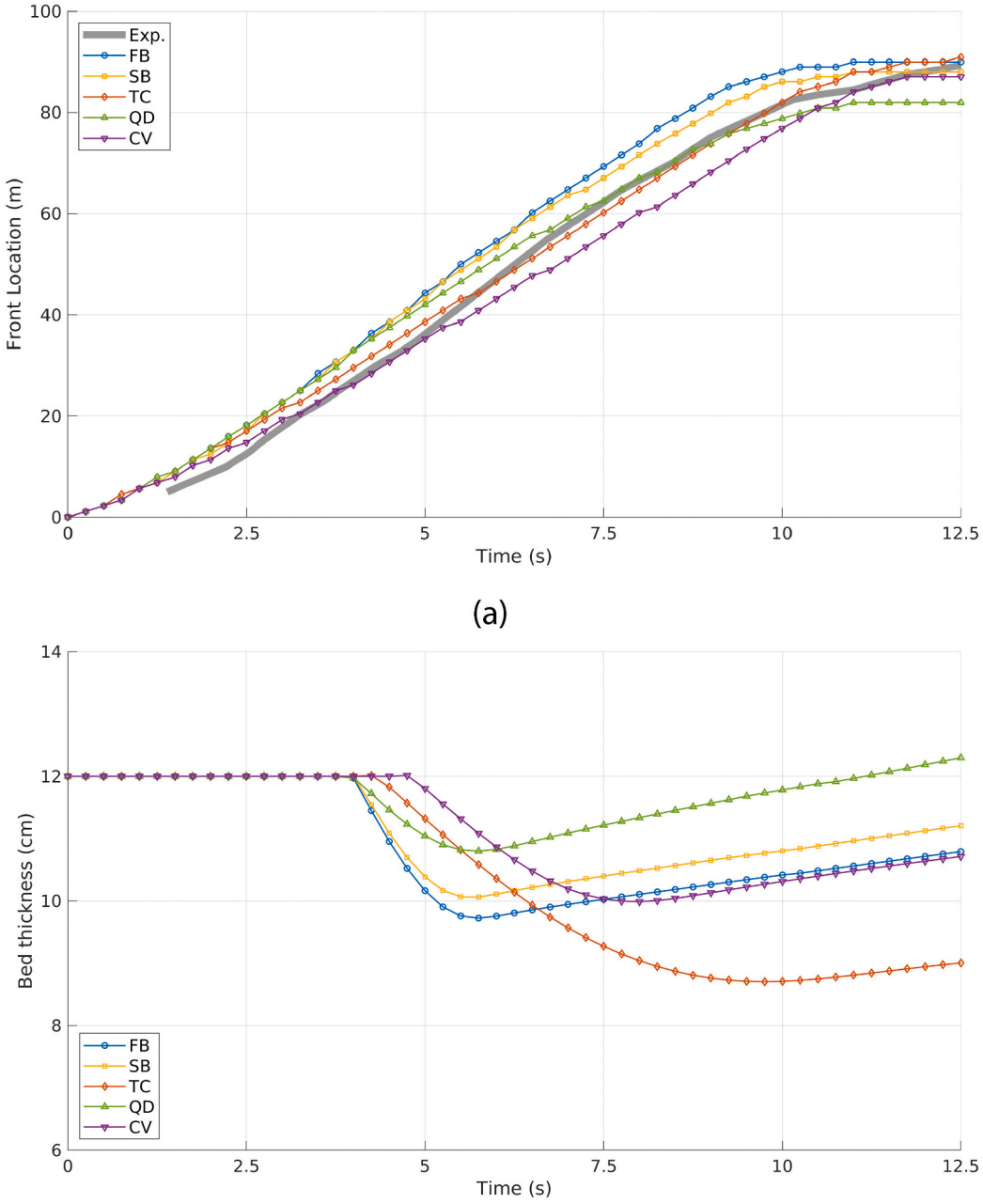

Fig. 17. Test G: temporal evolution of (a) the dambreak wave-front location and (b) the bed thickness at $s = 32$ m with different rheological relationships for the debris stress.

Table 8
Test G: RMSE for the flow free surface level at the control sections (P1 and P2) and for the wave-front location, and computational time required by the GPU-based algorithm to complete the simulation.

Formulation	RMSE		RMSE	Tesla k40c
	WSL_{P1} (m)	WSL_{P2} (m)	Front loc. (m)	Comp. time (s)
Full Bingham (FB)	4.46×10^{-2}	3.92×10^{-2}	5.97	21.43
Simplified Bingham (SB)	4.95×10^{-2}	4.10×10^{-2}	4.72	20.94
Turbulent Coulomb (TC)	3.83×10^{-2}	2.56×10^{-2}	2.72	26.28
Quadratic (QD)	5.16×10^{-2}	2.94×10^{-2}	4.38	20.61
Coulomb Viscous (CV)	1.81×10^{-2}	4.05×10^{-2}	3.55	21.73

Table 9
Test G: normalized wave-front speed S and post-entrainment flow volume V with all the rheological formulations simulated.

Formulation	Norm. speed S		Norm. vol. V	
	Value (–)	Rel. error (%)	Value (–)	Rel. error (%)
Measured	0.85	–	1.36	–
Full Bingham (FB)	1.0036	+18.06	1.1082	−17.91
Simplified Bingham (SB)	0.8495	−0.10	1.0452	−22.58
Turbulent Coulomb (TC)	0.9263	+8.90	1.3904	+2.99
Quadratic (QD)	0.7702	−9.17	0.9604	−33.30
Coulomb Viscous (CV)	0.8492	−0.10	1.1083	−17.90

Table 10
Test G: computational effort required by the GPU-based algorithm with different mesh refinement level and speed-up with respect to the CPU-based version.

Mesh	Cells number (–)	Averaged cell area (cm^2)	Cells increment (–)	Comp. time (s)		Speed-up (cpu/gpu) (–)
				Tesla k40c	i7-7700K	
M1	11515	500	$\sim\frac{1}{5}\times$ MR	4.497	12.073	×2.7
MR	57212	100	–	26.284	327.619	×12.5
M2	227803	25	~4×MR	155.904	4206.670	×26.9

experiment.

In order to assess the performance of the GPU-based algorithm for the computation of large-scale realistic mud/debris flow events, the computational time required with the above used mesh (taken as reference and called MR) is compared with computational time running in a CPU-core, both including the file input-output time. Moreover, the scalable acceleration of the GPU-based algorithm is showed by comparing the computational times using a mesh 5 times coarser than MR and referred as M1 (11500 cells), as well as with a mesh 4 times finer mesh than MR (referred as M2), with 228000 cells approximately. The computational efforts required for the GPU-based and CPU-based versions of the algorithm with the three considered meshes are reported in Table 10. Results show that for the reference mesh MR, the speed-up achieved by the GPU-based algorithm is 12 with respect to the CPU-based version. Furthermore, the performance of the GPU-based algorithm increases as the mesh is refined and the number of cells involved in the simulation is higher, with a speed-up near 27 for mesh M2.

Test C is simulated using the two more suitable basal resistance formulations for the USGS debris flow experiments, TC and CV relationships. The lower part of Fig. 18 depicts the bulk debris density and the upper part shows the longitudinal profile of the specific volumetric concentration of each sediment class at (a) $t = 6$ s and (b) $t = 18$ s after the gate opening using the TC rheological relation. In experiment C, the initial water content of the erodible bed was much higher than that of experiment G, leading to an increase of the bed material entrainment into the debris. The numerical results show that, when the flow progresses downstream and reaches the erodible bed, high concentration of the coarser solid phase appears rapidly at the wave-front whereas the volumetric concentration of the finer solid phases reduces.

As in test G, the finer fraction gains importance along the tail of the debris wave, although the volumetric concentration of the gravel fraction continues being higher than those of the sand and silt fractions. Furthermore, after the main wave-front reaches the runout zone and stops, secondary or roll waves are developed along the tail of the debris flow (see Fig. 18(b)). These roll waves are associated to the solid phases sorting, with higher concentration of the coarse sediment class at the wave head and finer grained more-liquefied tails (Jakob and Hungr, 2005). Roll waves move downstream and also stop when they reach the runout zone. This behavior is known as surge dynamics and is one of the mean features of the debris flows, mainly associated to the appearance of non-uniform shear stresses along the debris flow.

The temporal evolution of the flow free surface at control sections P1 ($s = 32$ m) and P2 ($s = 66$ m) has been depicted in Fig. 19 in comparison with the measured data. The wave-front arrival time to both control sections is again well predicted using the TC formulation, as well as the wave head level at the control section P1. However, the head level is slightly overestimated for the control section P2. Nevertheless, the CV formulation shows smaller arrival times and overestimates the free surface elevation of the wave head at both control sections, indicating higher flow velocities than those observed during the experiment.

The temporal evolution of the wave-front position is plotted in Fig. 20(a). The CV formulation shows much higher wave-front velocities than those observed during the experiment, whereas the TC rheological relation predicts correctly the wave-front advance. Furthermore, Fig. 20 (b) shows the computed temporal evolution of the bed thickness at $s = 13$ m, $s = 23$ m, $s = 33$ m and $s = 43$ m with both rheological formulations compared with the measured data. Both basal resistance relations predict the rapid degradation of the bed layer, but the TC formula shows a bed thickness evolution which agrees better with the measured data at all the control sections.

In order to analyse the sensitivity of the model to some calibration parameters, additional simulations are performed taking the above results for test C with the TC resistance formulation as reference. Considering that the solid phase features and the experiment description shown in Tables 5–7 are well-know from the original works (Iverson et al., 2010, 2011), the highest uncertainty arises from both the basal pore pressure coefficient γ_{pp} and the transport capacity modification parameter β_t. The 20% reduction of the basal pore pressure coefficient leads to a marked decrease of the wave propagation velocity whereas an 20% increment on γ_{pp} causes an increase of the wave propagation velocity (Fig. 21(a)). On the other hand, the variation of the transport capacity parameter β_t does not show a marked influence on the velocity propagation of the debris dambreak wave (Fig. 21(b)). Therefore, when the TC formulation is used for the basal resistance, a correct calibration of the the basal pore pressure coefficient γ_{pp} is essential.

As a main conclusion of the results shown above, the TC formulation for the debris stresses is considered as the most suitable to reproduce the USGS debris flume experiments. This relationship has also been used in other previous works to reproduce this set of experimental data (Ouyang et al., 2015a; Xia et al., 2018; Li et al., 2018). Therefore, the remaining six experiments are simulated using the TC formula to estimate the basal resistance along the debris flow. Fig. 22 shows the computed wave-front position against time for all the tests carried out at the USGS flume, compared with the measured front evolutions. The proposed model is able to predict reasonably well the advance of the dambreak debris wave for most of the experiments. Nevertheless, important differences appear in some cases, especially in tests H and D where the model overestimates the runout distance with respect to those observed in the corresponding experiments.

Finally, Table 11 shows the normalized wave-front speed S between $s = 60$ m and $s = 70$ m and the normalized post-entrainment flow volume V computed with TC formulation for the all the experiments carried out at the USGS debris flume, compared with the measured data. The proposed model is able to correctly estimate both dynamic data with relative errors lower than 20% for all the experiments, with the exception of the normalized wave-front velocity S for the tests H and F which shows important differences between experimental and computed values. Further developments of the physical model could be required to improve these numerical results.

5.3. Mine tailings dam failure in Brumadinho (Brasil)

The aim of this test is to assess the performance of the model for simulating a real large-scale highly unsteady mud flow, comparing the obtained results with the available field observations and gaining a better insight into the behavior of this kind of violent flows. On 25th January 2019 (12:28 p.m.), the Dam I at the C'orrego do Feijão Iron Ore Mine, located 9 km north-east of Brumadinho in the state of Minas Gerais (Brazil), suffered a sudden catastrophic failure, resulting in an extremely violent mud flow which traveled downstream more than 10 km and reached the Paraopeba River, a major tributary of the São Francisco River. This disaster caused more than 260 deaths and important economic and environmental losses. The dam consisted of 12×10^6 m^3 mining waste tailings with a height of $70 - 80$ m, constructed over a period of 37 years in 10 raises and covering an area of 4.13×10^5 m^2. The initial failure extended across the face of the dam and the slope collapse was complete in less than 10 seconds. Most of the

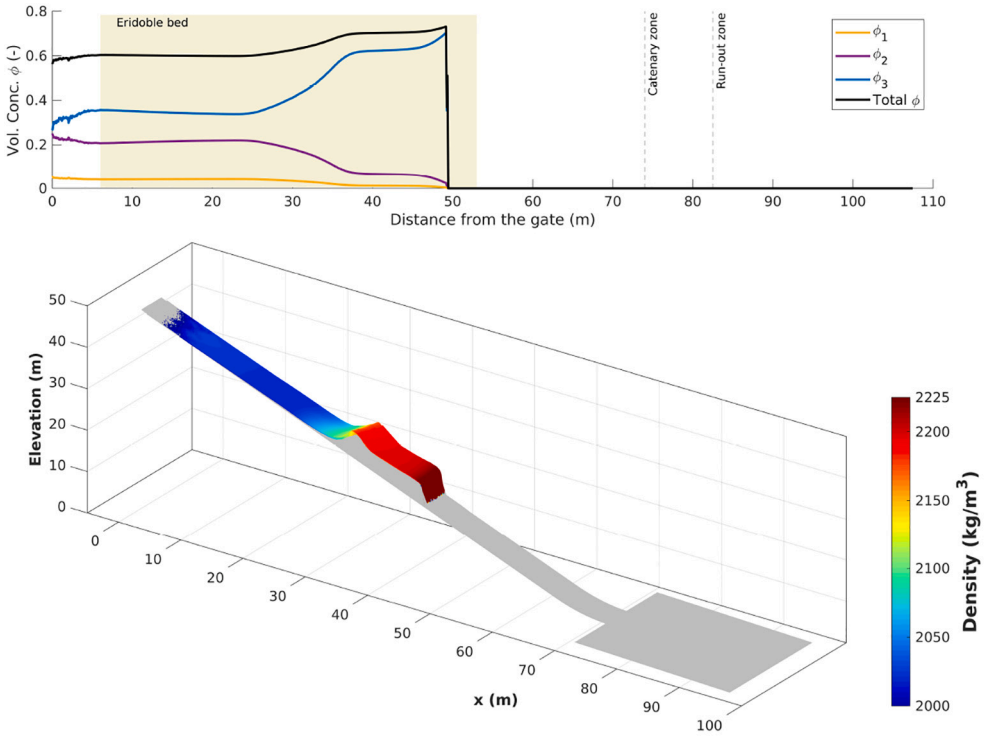

(a) $t = 6\,s$

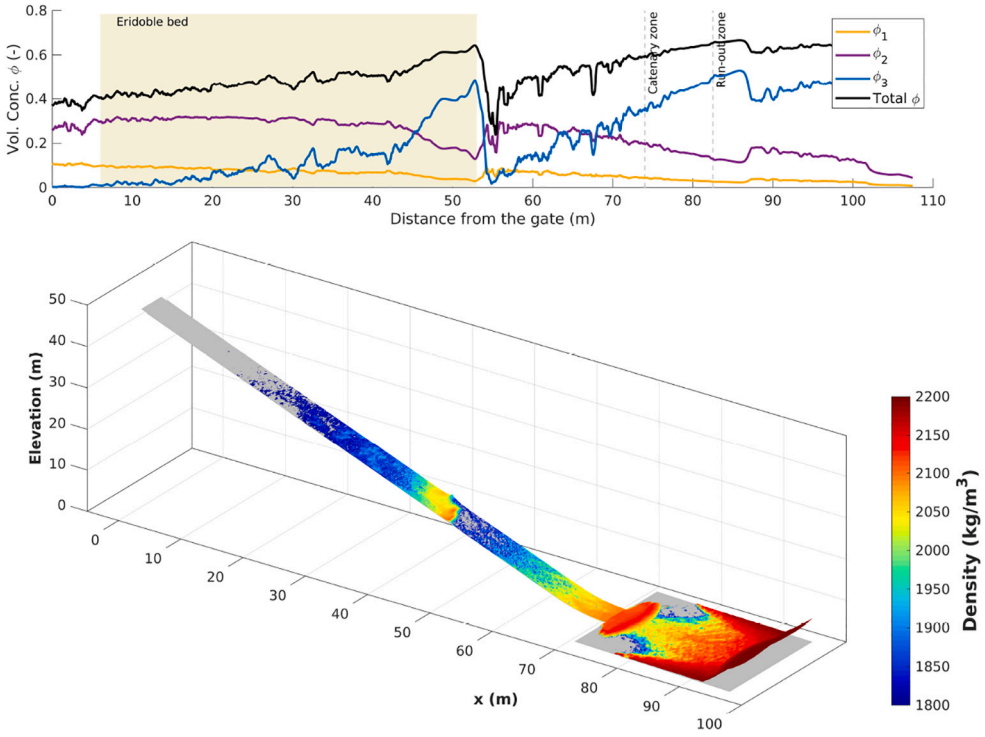

(b) $t = 18\,s$

Fig. 18. Test C: spatial flow distribution at (a) $t = 6$ s and (b) $t = 18$ s after the gate opening for test G and using the TC friction.

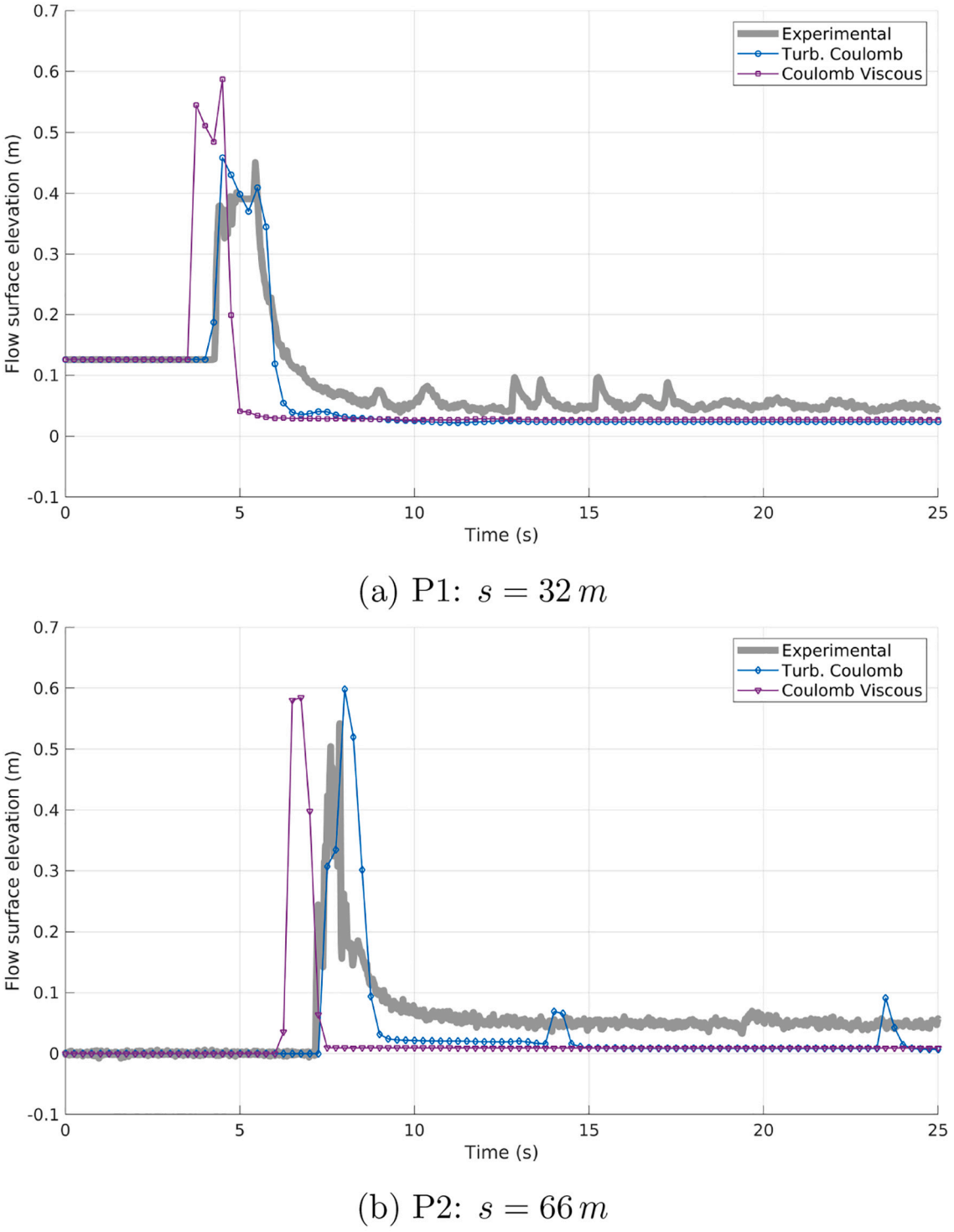

Fig. 19. Test C: temporal evolution of the flow free surface at (a) P1 and (b) P2 with TC and CV rheological relationships for the debris stress. (a) P1: $t = 32$ m. (b) P2: $t = 66$ m.

dam material flowed out of the dam in less than 5 minutes. The tailings in the dam showed a sudden and significant loss of strength and rapidly became a heavy liquid that flowed downstream at a high speed (about 120 km/h in some zones). Based on the available videos, it is clear that the failure was the result of flow static liquefaction within the materials of the dam (Robertson et al., 2019).

Table 12 shows some of the features of the materials in the dam. Tailings were composed by a mixture of water, sediments and heavy metals, mainly iron (Fe) 264.9 mg/g, aluminum 10.8 mg/g, manganese 4.8 mg/g and titanium 0.5 mg/g (Vergilio et al., 2020). The size distribution consisted basically of a mineral sand fraction (38%) and a fines fraction (62%), accounting for mineral silt-clay and metals particles. The water content before the failure was estimated around 50% by volume with a specific weight of $22 - 26$ kN/m^3 (Robertson et al., 2019).

Fig. 23 shows an aerial image of the mine site after the dam collapse, including the dam location and the original tailings elevation in meters above sea level ($m.o.s.l$). The area affected by the mud was 3.3×10^6 m^2, without including the original dam area, and reached the

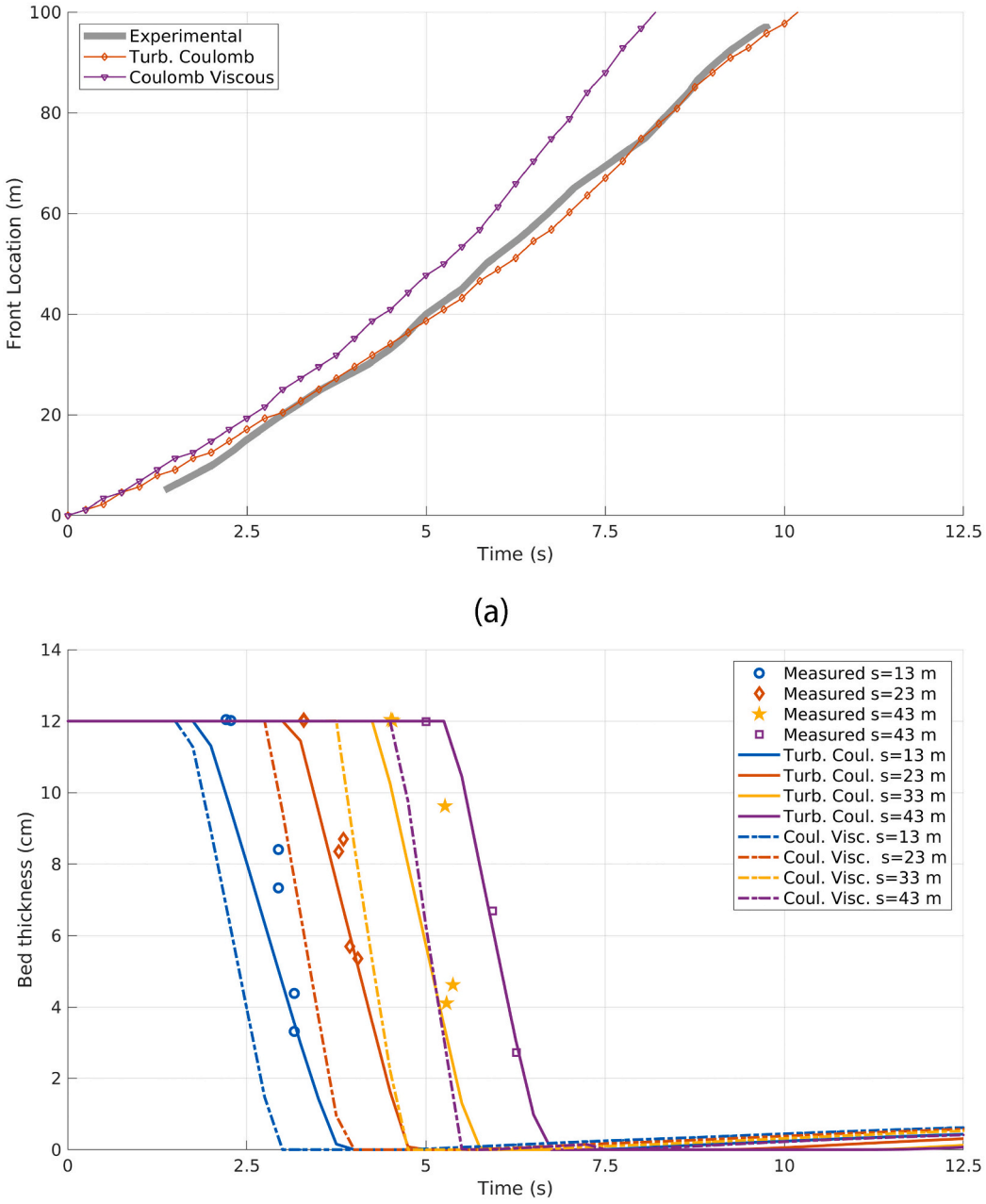

Fig. 20. Test C: temporal evolution of (a) the dambreak wave-front location and (b) the bed thickness at $s = 13$ m, $s = 23$ m, $s = 33$ m and $s = 43$ m with TC and CV rheological relationships for the debris stress.

Paraopeba River 8.5 *km* downstream the dam.

In order to perform the simulations, a spatial domain of 10.396×10^6 m^2 is discretized using a unstructured triangular mesh with 5,30,000 cells approximately and slightly refined in the dam area. Four control cross-sections are placed downstream of the dam at (CS-1) the mine stockpile area, (CS-2) the railway bridge, (CS-3) the Alberto Flores road and (CS-4) the Alberto Flores Gauge Station in the Paraopeba River. Furthermore, the base regime water depth and velocities in the Paraopeba River before to the mud arrival is assessed by a previous simulation (without considering the tailings dam collapse) setting a constant clear water inlet of 45.6 m^3/s and uniform flow conditions at the outlet boundary. The mean thalweg slope in the Paraopeba River is $S_0 = 0.0025$ m/*m*. This previous simulation runs until the solution converges to the base steady state. Numerical results shows that the maximum water depth in the Paraopeba River before the dam collapse is around 3.5 m with a negligible sediment concentration at the outlet boundary (lower than 2% by volume) and maximum flow velocities about 2.5 m/s (see Fig. 23).

Fig. 24 shows the terrain elevation ($1 \times 1m$ DTM) previous to the dam collapse. The thalweg elevation along the area covered by the mud varies between 860 m.*o.s.l.* at the dam-toe and 720 m.*o.s.l.* at the Paraopeba River, with an averaged longitudinal bed slope $S_0 = 0.0165$ m/*m*. The initial tailings depth at the dam is estimated by comparing the terrain elevation before and after the dam failure using $1 \times 1m$ DTM's.

Six different solid phases are set, including mineral sand, mineral silt, iron (Fe), aluminum (Al), manganese (Mn) and titanium (Ti). A summary of the main parameters used in the simulation is shown in Table 13. The tailings mixture is considered fully saturated with an initial global volumetric concentration of solids $\varphi_0 = 0.5$, leading to a mixture density $\rho = 2247.5$ kg/m^3. The specific initial volumetric concentration for each solid phase φ_p is estimated from the available literature (Robertson et al., 2019; Vergilio et al., 2020; Rotta et al., 2020).

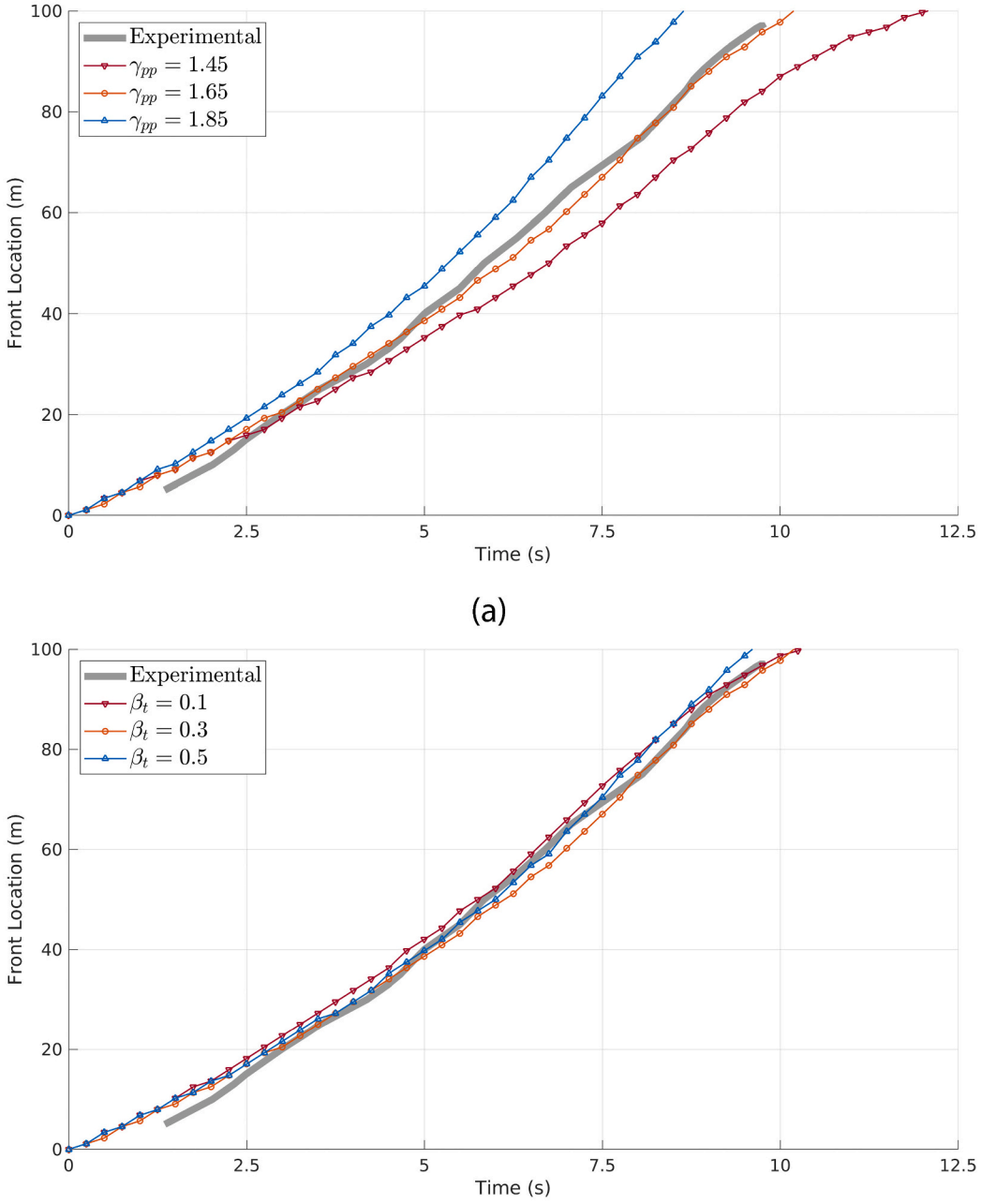

Fig. 21. Test C: temporal evolution of the dambreak wave-front location with (a) increasing basal pore pressure coefficient γ_{pp} and (b) increasing transport capacity modification parameter β_t, using TC rheological relationships for the debris stress.

The deposition porosity p_p and the hiding-exposure effects on the incipient motion critical Shields stress $\theta_{c,p}$ for each solid phase are estimated using the Wu's (Wu, 2007) and the Egiazaroff's (Egiazaroff, 1965) formula, respectively. As the mining tailings in the dam showed a low plasticity and high values of pore-fluid pressure (Robertson et al., 2019) before the collapse, the TC friction formulation is set for the estimation of the flow basal resistance during the simulation. The land use along the area covered by mud was mainly forest and agriculture, hence a uniform Manning's roughness parameter $n = 0.065$ s m$^{-1/3}$ is used and the transport capacity modification parameter is set to $\beta_T = 0.5$ for all the solid phases. A basal friction angle intergranular stress $\phi = 5^{\circ}$ and a pore-fluid pressure excess factor $\gamma_{pp} = 2.05$ are also set. For the sake of simplicity, and based on the results obtained in the above synthetic test C, the fixed-fraction approach is selected here for the computation of the specific bed entrainment. The simulated time is $t_{end} = 3$ h from the dam collapse and the CFL is set to 0.95. Simulations are performed in a NVIDIA GeForce GTX 1080 Ti device with the GPU-based code, whereas the Intel(R) Core(TM) i7-3820 @3.60GHz is used for the CPU-based algorithm.

Fig. 25 shows the mud flow depth at (a) $t = 5$ min, (b) $t = 10$ min and (c) $t = 35$ min after the dam collapse, whereas Fig. 26 depicts the modulus of the flow velocity at the same times. The numerical results show that practically the whole initial tailing volume flows out of the dam in the first 5 minutes after the dam collapse, as it was observed in the available videos. The mud wave moves downstream with a computed height larger than 25 m and with velocities higher than 15 m/s (54 km/h) in some zones during the first minutes. Furthermore, the simulation results indicate that the mud reaches the mining treatment plant and the stockpile areas (CS-1), as happened during the real event. After this initial stage, the numerical results show that the dambreak wave decreases its velocity at $t = 10$ min but the computed mud depth is still higher than 20 m when the wave-front reaches the railway bridge

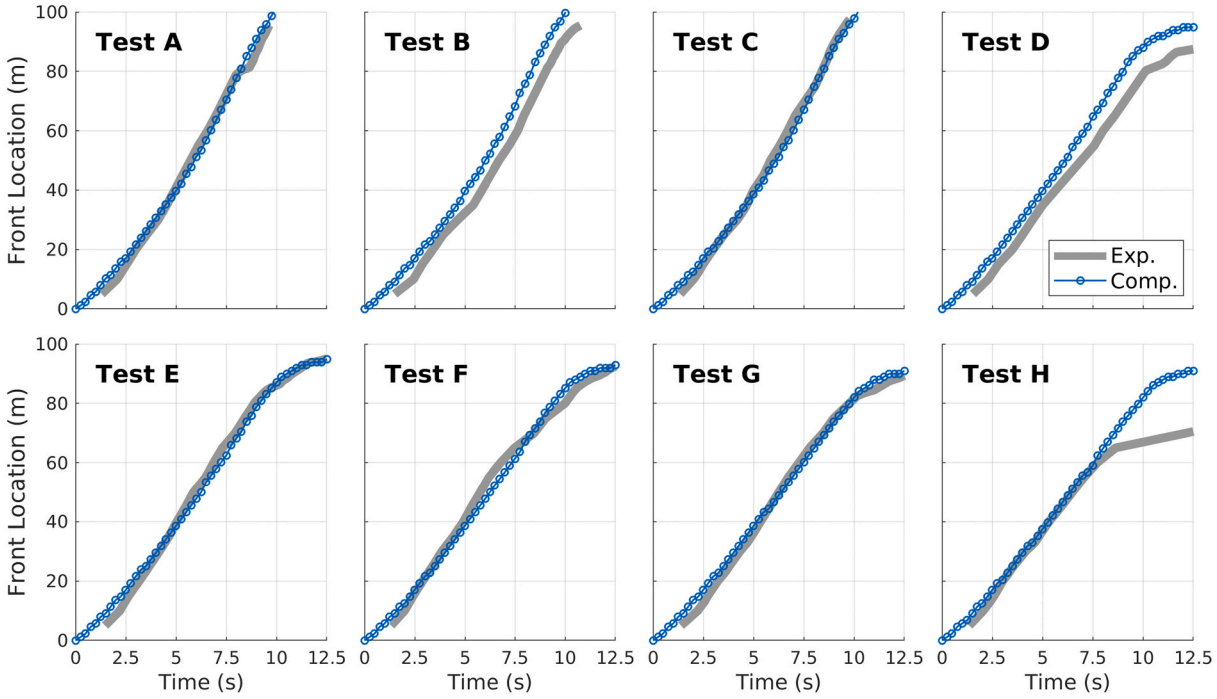

Fig. 22. Temporal evolution of the dambreak wave-front location with TC rheological relationship for the all the experiments carried out at the USGS debris flume.

Table 11
Measured and computed normalized wave-front speeds S and post-entrainment flow volumes V with TC rheological formulation for all the experiments carried out at the USGS debris flume.

	Front vel. S			Debris Vol. V		
Test	Measured (–)	Computed (–)	Rel. error (%)	Measured (–)	Computed (–)	Rel. error (%)
A	1.33	1.38	+4.5	3.05	2.73	-10.5
B	1.53	1.51	-1.6	2.59	2.64	+1.8
C	1.19	1.38	+17.5	2.27	2.61	+15.2
D	1.01	1.11	+10.0	2.20	2.21	+0.6
E	0.95	1.02	+7.2	2.24	2.18	-2.4
F	0.61	1.01	+67.0	1.52	1.63	+8.1
G	0.85	0.92	+8.9	1.36	1.39	+2.9
H	0.24	1.01	+324.5	1.56	1.48	−4.4

Table 12
Dam and tailings features.

Dam capacity	12×10^6 m^3			
Dam area	4.13×10^5 m^2			
Solid-phase concent. φ_0	50%			
Water content C_w	50%			
Specific weight	22 − 26 kN/m^3			
Size distribution	Sand		Fines	
Relative content	38%		62%	
Heavy metals	Fe	Al	Mn	Ti
Weight concentration	264.9 mg/g	10.8 mg/g	4.8 mg/g	0.5 mg/g
Relative content	87%	10%	1.7%	0.3%

(CS-2). During the real event, the mud wave impact caused the collapse of the railway bridge structure. As the wave moves downstream, the velocity and depth of the mud reduce progressively along the whole flow, not only in the wave-front. Numerical results show that 35 min after the event beginning, the mud wave-front is close to the Alberto Flores road (CS-3) and the flow is practically stopped in all zones. As it was observed during the real event, the simulation predicts that the wave-front reaches the Paraopeba River, flowing into the riverbed and creating a "dam" which increases progressively the upstream water level at the Alberto Flores Gauge Station (CS-4) along the following hours. The computed mud accumulation reaches 14.5 m in some zones after the flow deposition.

Fig. 27 depicts the predicted temporal evolution of the mud wave-front location and velocity along the thalweg each 2.5 min during the first hour of the flow. At the first stages, the velocity of the wave-front is around 50 km/h and it is progressively decreasing as the flow progresses downstream until the wave-front reaches the Paraopeba River 43.5 min after the dam collapse.

The predicted temporal evolution of the cross-section averaged flow depth and the total volume discharge (m^3/s) at the stockpile area (CS-1), the railway bridge (CS-2) and the Alberto Flores road (CS-3) are plotted in Fig. 28. For cross-section CS-1, the discharge shows a peak of 38000 m^3/s with an average mud depth of 7.5 m at $t = 2.5$ min. However, the flow has reduced its velocity considerably 10 min after the dam failure and the deposited mud depth along this cross-section is lower than 0.2 m. In this zone just downstream the dam-toe, the simulation predicts that the mud wave erodes the original bed and gains mass and momentum during the first stages of the flow. The predicted increment of the volume involved in the flow is near 56% of the original mass due to entrainment from the erodible bed. Hence, when the flow reaches cross-section CS-2, the average flow depth is near 12 m although the discharge shows a lower peak (14000 m^3/s) at $t = 5$ min, caused by the

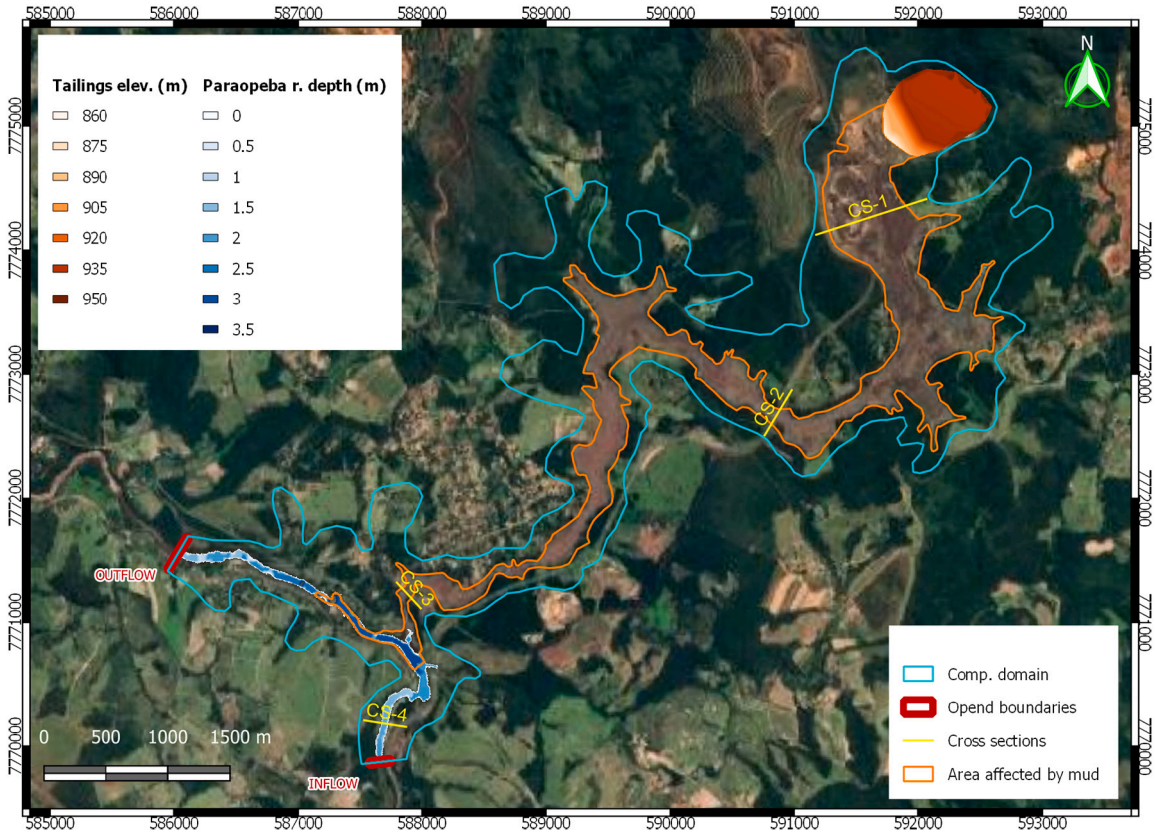

Fig. 23. Aerial image of the area affected by the mud and the computational domain used in the simulation.

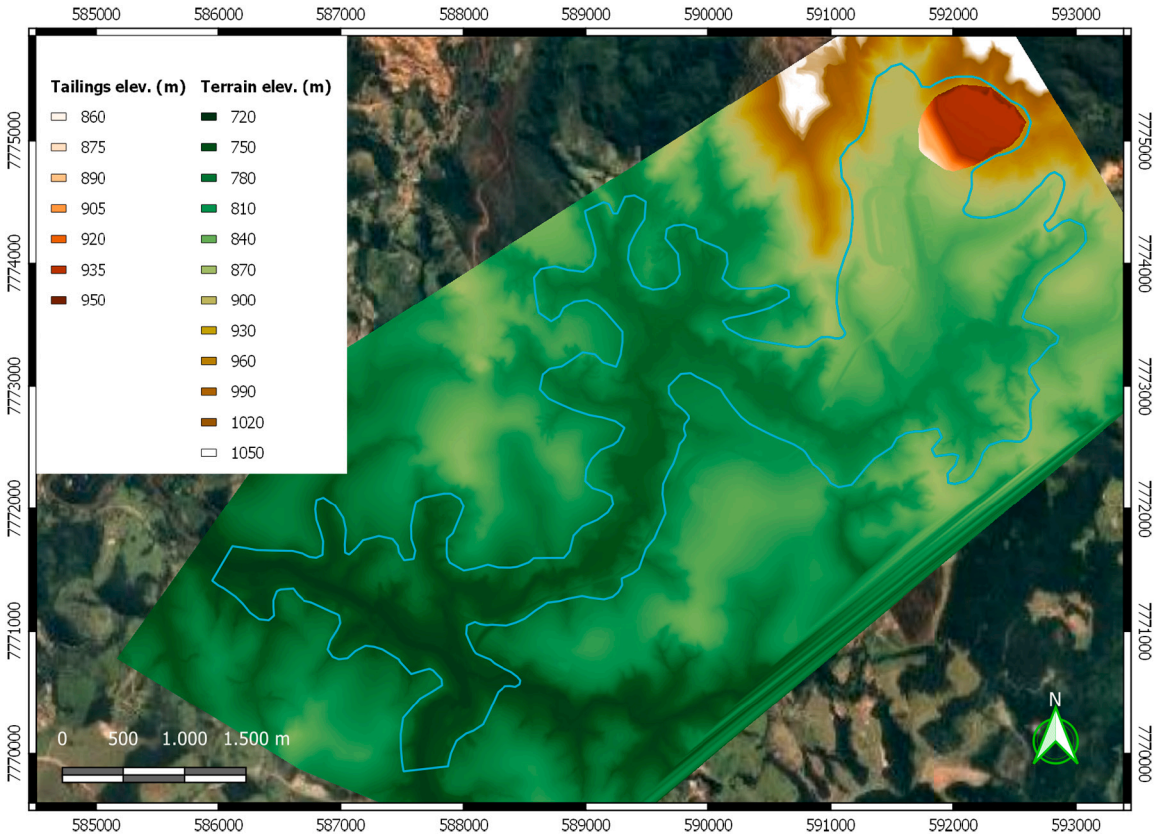

Fig. 24. Terrain elevation before the dam collapse (1 × 1 m DTM).

Table 13
Parameters used in the simulation.

Liquid density ρ_w (kg/m^3)	1000					
Initial mixture density ρ (kg/m^3)	2247.5					
Internal stability angle ϕ_b(°)	5					
Manning roughness coeff. n (s m$^{-1/3}$)	0.065					
Pore press. excess coeff. γ_{pp} (−)	2.05					
Global critical Shields stress θ_c (−)	0.030					
Transport capacity parameter β_T (−)	0.5					
Number of solid phases	6					
Solid phase	Sand	Silt	Fe	Al	Mn	Ti
Medium diameter d_p (*mm*)	0.4	0.075	0.075	0.075	0.075	0.075
Initial concent. φ_p (−)	0.19	0.224	0.075	0.009	0.0015	0.0003
Solid density ρ_p (kg/m^3)	2700	2700	7874	2700	7210	4506
Bed fraction $F_{b,p}$ (−)	0.38	0.62	0.0	0.0	0.0	0.0
Deposition porosity p_p (−)	0.35	0.45	0.45	0.45	0.45	0.45
Critical Shields stress $\theta_{c,p}$ (−)	0.020	0.067	0.067	0.067	0.067	0.067

reduction of the flow velocity. In this cross-section CS-2, the movement of the mud is practically stopped 50 min after the dam failure. Nevertheless, the predicted temporal evolution of the flow at cross-section CS-3 shows a more progressive depth increment with time and a much lower discharge, needing more than 2 h after the dam failure before the mud is totally stopped.

Fig. 29 shows (a) the mud density distribution and (b) the iron solid phase volumetric concentration for $t = 60$ min after the dam collapse. Generally, the flow density remains approximately constant and higher than 2100 kg/m^3 for the first stages of the flow. Then, the density progressively reduces as the flow moves downstream, especially at the upstream region and at the boundaries of the area affected by mud, where deposition of the solid phases dominates due to the lower velocities. In the center of the channel at the downstream region, where a slight movement of the flow continues even at $t = 60$ min, the density shows important variations with respect to the original mud density. Once the flow reaches the Paraopeba River, the mud starts to mix with the "clear water" of the Paraopeba River and the flow density decreases abruptly along the mixing interfaces. Spatial differences in the solid concentration are more marked for the iron phase, since it is more affected by deposition due to its higher density. Therefore, the iron volumetric concentration in the flow decreases more rapidly than the mineral solid phases or the mixture bulk density in the low velocity regions.

The most important available observation during the real disaster is the arrival of the mud wave to the Paraopeba River. Herein we compare some observed data with the numerical results obtained by the model. At the Alberto Flores road (CS-3), the height of the mud once the flow stopped was estimated between 4-5 meters from published photographies. Fig. 30(a) shows the computed bed and flow free surface profiles at CS-3 for $t = 3$ h. The maximum mud depth is 4.9 m and agrees with the observed data. Furthermore, the Alberto Flores Gauge Station in the Paraopeba River, upstream the mud-river confluence, also offers interesting data for comparison. This gauge station continuously recorded the free surface level each 15 min. During the real event, the mud flowing into the river created a "dam" in the confluence region, which temporally increased the free surface level in the Paraopeba River upstream the confluence region until the water reached the maximum elevation of the "dam" and started to flow over the mud. The observed temporal variation curve of the free surface level at the Alberto Flores

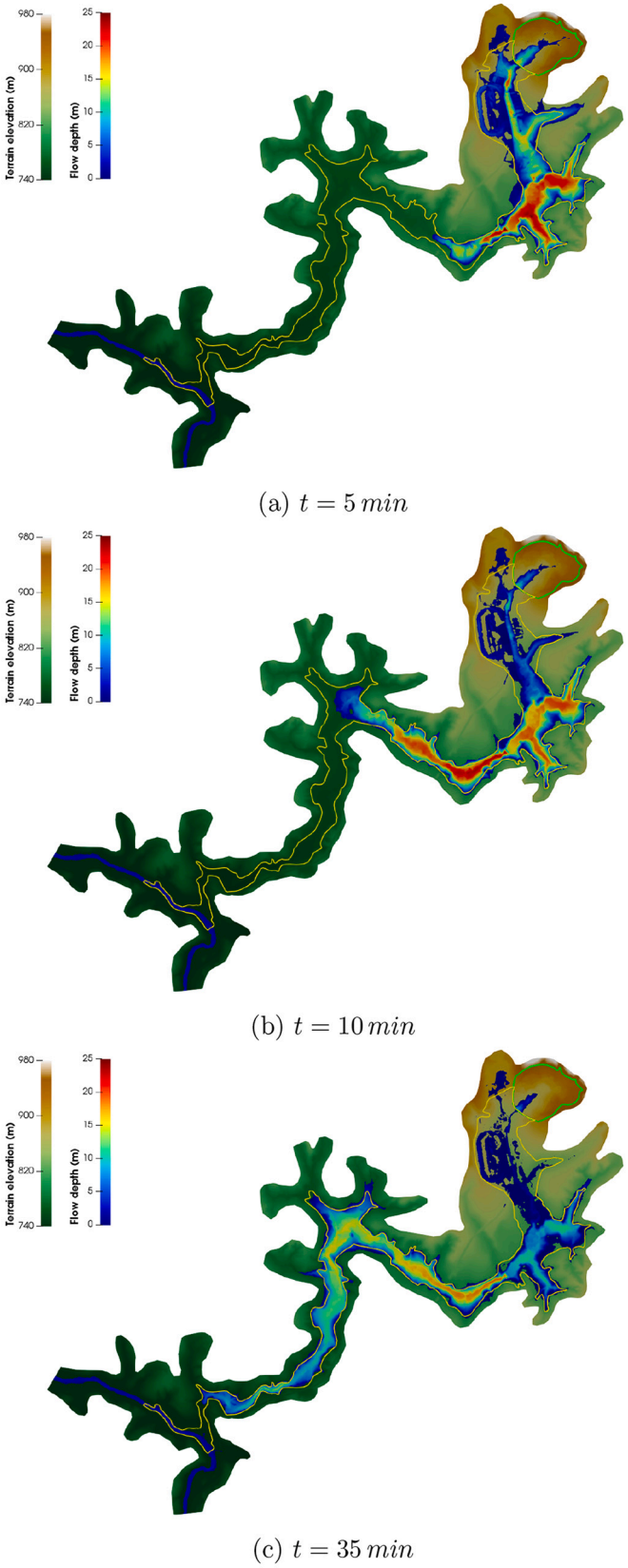

Fig. 25. Mud flow depth at (a) $t = 5$ min, (b) $t = 10$ min and (c) $t = 35$ min after the dam collapse.

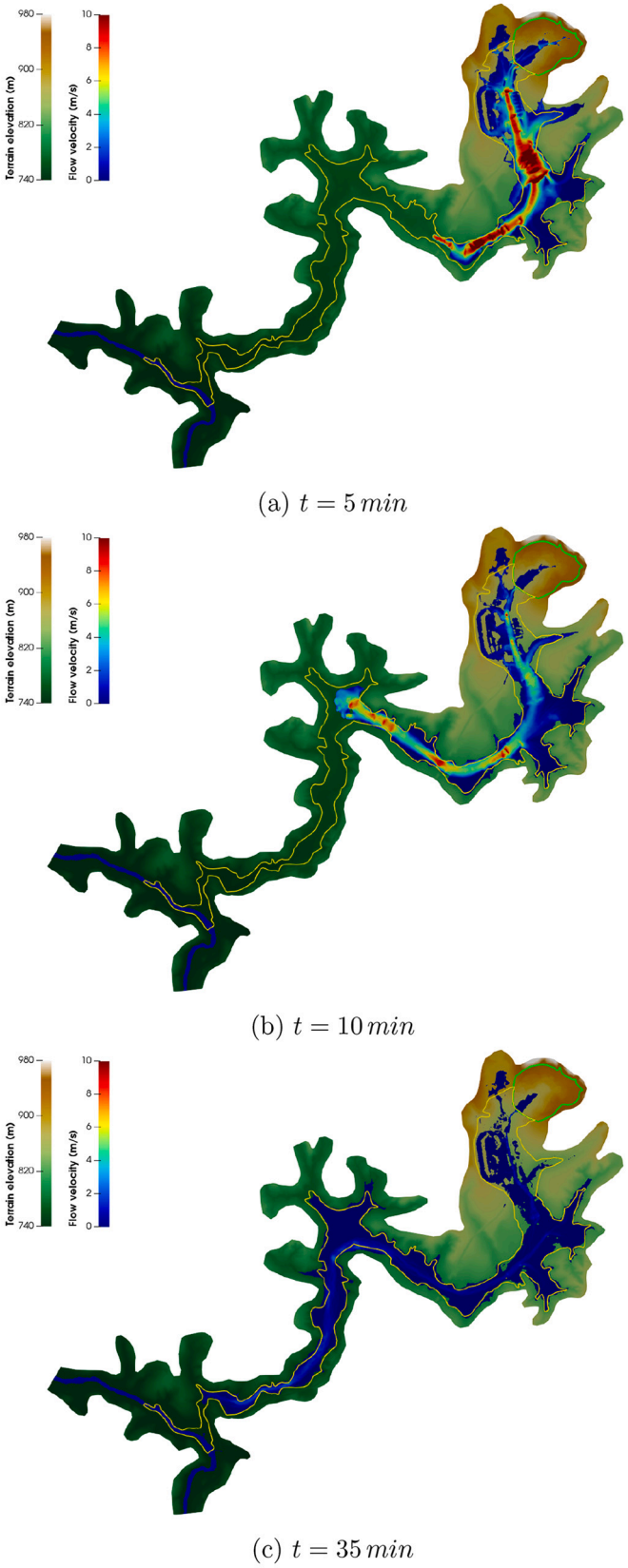

Fig. 26. Modulus of the mud flow velocity at (a) $t = 5$ min, (b) $t = 10$ min and (c) $t = 35$ min after the dam collapse.

Gauge Station can not be compared directly with the numerical results obtained for the control cross-section CS-4, because of the different storage capacity upstream the confluence between the simulation domain and the real river. However, two important conclusions can be extracted from the recorded data. First, the river free surface level at the gauge station started to increase 32 – 47 min after the dam collapse, capturing the arrival interval of the mud flow to the river. Second, the maximum level registered by the free surface was 5.11 m above the base regime level previous to the mud arrival, indicating the height of the mud "dam" at the confluence region. Fig. 30(b) depicts the predicted temporal evolution of the river water depth and discharge at the control cross-section CS-4. The model is able to capture the arrival time of the mud flow to the river (43.5 min). Moreover, the maximum increment of the free surface level at CS-4 is 4.06 m, showing a reasonably agreement with the observed data.

Table 14 shows a comparison of the observed and computed data which can be extracted for this event. The model is able to correctly estimate the mud volume released and the area affected by mud. Furthermore, also the mud accumulation at the Alberto Flores road (CS-3) and the height of the mud "dam" at the confluence region showed a reasonable agreement, as well as the arrival time to the Paraopeba River (CS-4).

In order to assess the spatially distributed hazard level caused by the dam collapse, the maximum mud flow depth and velocity are continuously recorded at each computational cell during the whole simulation. Firstly, Fig. 31(a) shows that the maximum mud depth occurs downstream of the dam-toe and along the thalweg zone next to the stockpile area, with mud depth values higher than 35 m, but the flow depth is higher than 10 m at some time during the simulation practically until the flow reaches the river. Secondly, the highest velocity is also computed downstream the dam-toe with values higher than 100 km/*h*, as it is shown if Fig. 31(b). These results are also in agreement with the available observed data, since an approximated velocity of 120 km/*h* for the wave-front was estimated at the first stage from the available videos of the dam collapse.

Finally, Table 15 shows the computational time required for simulating the 3 h event using GPU-parallelization compared with the CPU-based version of the code, both including the file input-output time. While the computational time for the CPU algorithm was almost 2.5 days, the GPU algorithm required less than 1 h to complete the simulation, representing a 61 speed-up. That means that for achieving the GPU-parallelized code performance with a CPU-based algorithm, a cluster with at least 76 CPU cores is required.

6. Conclusions

This work is focused on the development of a GPU-accelerated Efficient Simulation Tool (EST) for 2D variable-density mud/debris shallow flows over erodible bed able to deal with non-structured meshes for the simulation of large-scale realistic events. The system of depth-averaged equations is formed by the 2D conservation equations for the mass and momentum of the multi-grain mixture, supplemented by the mass conservation equation for the different solid phases transported in the flow and the non-uniform bed evolution equation. The depth-averaged density of the mixture varies according to the volumetric concentration of the different solid-phases, that can be incorporated into the flow or deposited in the bed independently. By defining a new mixture variable called buoyant solid concentration φ^{χ}, the initial $3+N+1$ conservation equations can be addressed as a hyperbolic system of five equations, where the density and depth of the mixture remain coupled in the conservative part of the system. This avoids the appearance of numerical instabilities when marked density gradients occur in the flow.

The main contribution is the development of an accurate, robust and efficient Riemann solver based on the augmented Roe (A-Roe) approach to solve variable-density flows. The proposed Riemann solver maintains the mixture density coupled with the flow depth into the conserved

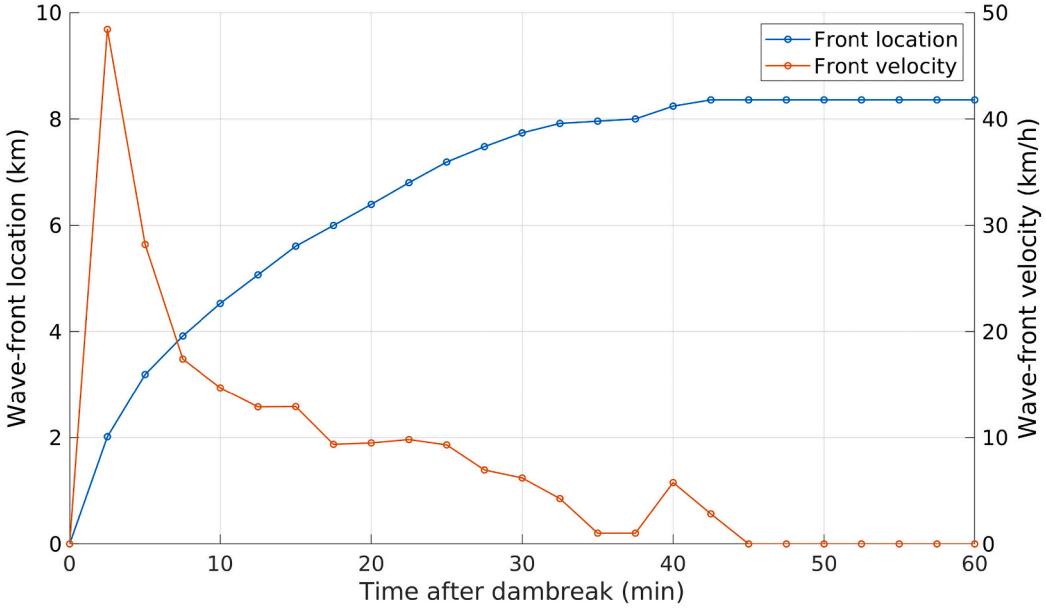

Fig. 27. Temporal evolution of the wave-front until the mud flow reached the paraopeba River.

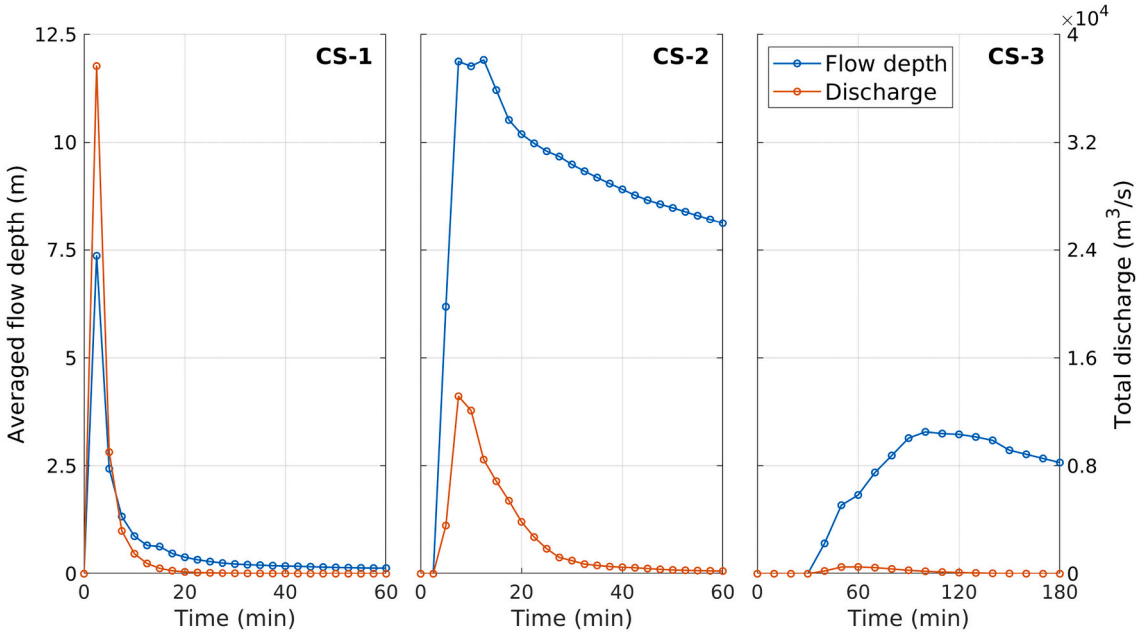

Fig. 28. Temporal evolution of the cross-section averaged flow depth and the total volume discharge at the stockpile area (CS-1), the railway bridge (CS-2) and the Alberto Flores road (CS-3).

variables and the intercell numerical fluxes, instead of including the spatial density gradients by means of a source term in the momentum equations. This requires a complete reformulation of the averaged-Roe variables at the intercell edges, allowing that the density of the mixture participates in the definition of the characteristic wave celerities of the local Riemann problem. The numerical scheme is defined to ensure a well-balanced flux formulation in steady states and wet-dry boundaries. The non-Newtonian rheological behavior of the multi-grain mixture is included into the momentum equation using six different basal resistance formulations. The global time step is dynamically controlled by the wave celerities of the coupled system of equations, preserving the scheme stability even for high flow-bed interaction and density gradients, and reducing the computational effort required by the model. Special attention has been paid to the integration procedure for the momentum source terms, avoiding excessive time step restrictions caused by an incorrect estimation of the basal resistance term. Furthermore, both the fixed-fraction and the active layer approaches have been considered for the estimation of the bed entrainment.

The numerical model has been first tested using three idealized highly sediment-laden flows. In the synthetic Test A, the model is able to deal with a different-density flow confluence, showing the importance of including the mixture density into the Riemann problem formulation to correctly address mixing problems. The synthetic Test B is used to demonstrate the behavior of the scheme when a marked bed entrainment is considered, also showing the stability and robustness of the

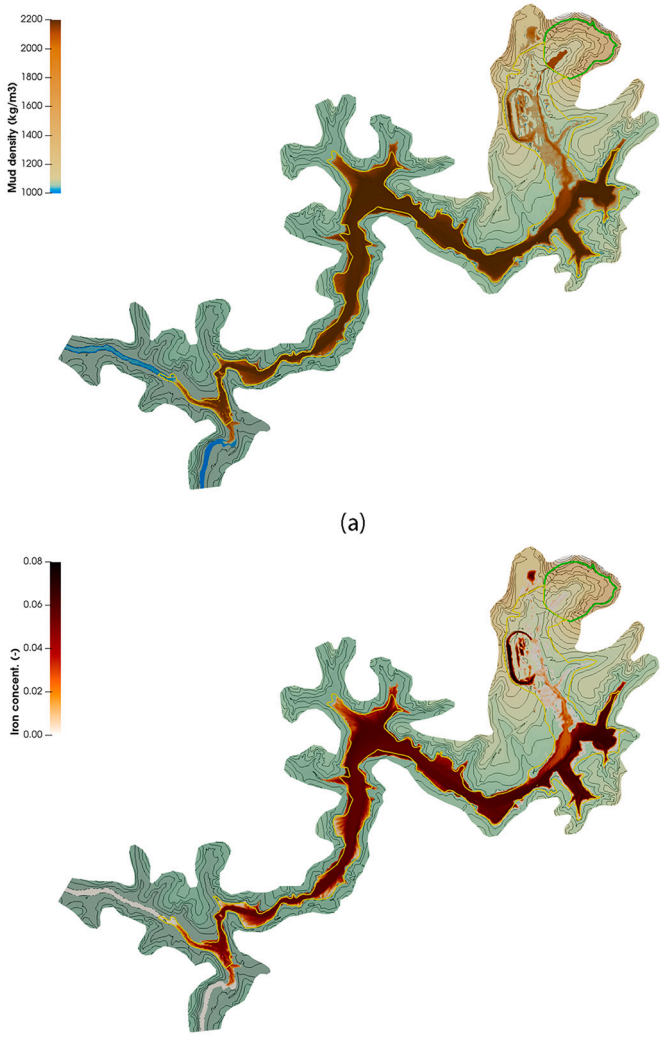

Fig. 29. (a) Mud density and (b) iron volumetric concentration for $t = 60$ min after the dam collapse.

proposed scheme. The synthetic test C is based on the above test B, but considering non-uniform bed. Despite the active layer approach affects both the bed entrainment and the sediment size distribution in the flow column along the dambreak wave, differences in the main features of the flow are not noticeably modified with respect to those obtained using the fixed-fraction approach.

Then, the mud/debris flow model has been validated against the completed set of USGS debris dambreak experiments over erodible bed reported in (Iverson et al., 2011). Numerical results obtained using different formulations for the basal resistance have been compared with the experimental data. The TC (Turbulent & Coulomb) formula is the most suitable to predict the measured data. Moreover, the model demonstrates to be able to predict the debris advance and wave-front velocity in almost the eight different dambreak experiments carried out at the USGS flume, with relative errors lower than 15%, although important differences appear in two of them. The temporal evolution of the different solid-phases concentrations throughout the flow shows that, for the highly wetted bed cases, the entrainment flux creates larger concentrations of the coarser solid phase at the wave-front whereas the finer fractions dominate at the tail of the dambreak wave.

In order to assess the performance of the model to simulate realistic mud/debris flow events, the mining tailings dam failure occurred on 25th January 2019 at Brumadinho (Brazil) has been simulated. The numerical results show a very good agreement with the available observations during the real disaster. The model is able to estimate accurately the tailings volume released, the area affected by the mud and the arrival time of the wave-front to the Paraopeba River. Furthermore, the numerical and observed mud depth at different sections after the flow stopped have been compared, showing also a good agreement.

The computational acceleration obtained with the GPU-based algorithm has been assessed in comparison to a CPU-based version of the algorithm. The computational acceleration obtained with the GPU-based algorithm scales with the number of cells of the spatial domain, being up to 61 times faster (using a medium-grade graphic processing device) than the CPU-based algorithm for domains larger than 10^5 cells. That means that, for achieving the GPU-accelerated performance with a CPU-based algorithm, a cluster with at least 76 CPU cores is required. It is worth noting that all the tests presented in this work using the GPU-based code have been performed on medium-grade NVIDIA devices. It is expected that the performance of the GPU-accelerated algorithm may increase markedly running in last generation NVIDIA GPUs. Due to the complexity and high uncertainty in mud/debris flow modelling, a high number of simulations are needed for the calibration of models, as well as for the evaluation of control measurements or the elaboration of hazard maps. Therefore, the correct modelling of this kind of flows in a reasonable time is only possible using high performance computing algorithms, being the GPU-based computation the most promising option.

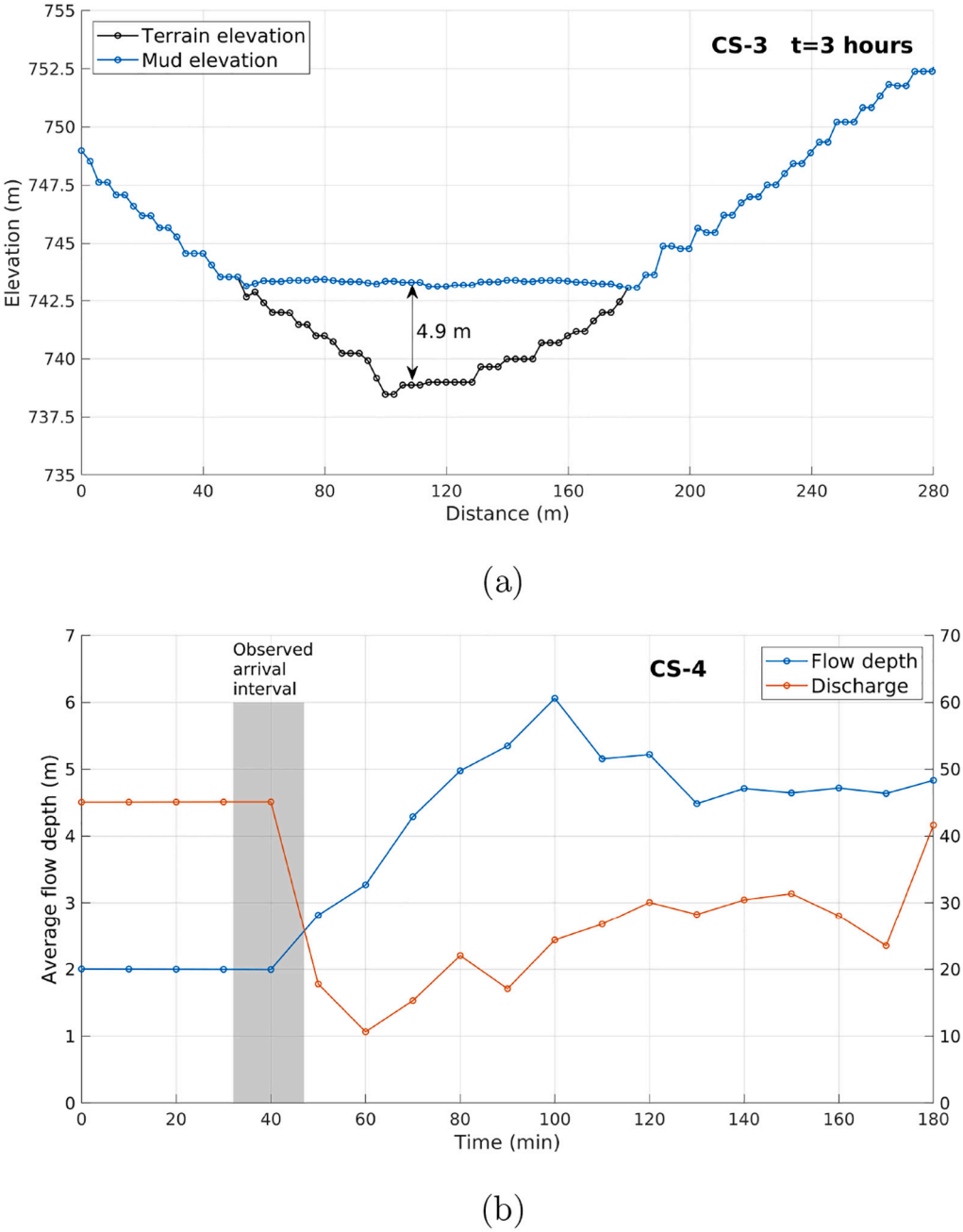

Fig. 30. (a) Bed and mud level profiles at CS-3 for $t = 3$ h and (b) temporal evolution of the river water depth and discharge at CS-4.

Table 14
Comparison of observed and computed data.

	Observed	Computed
Released tailings volume (m^3)	9.6×10^6	9.747×10^6
Affected area (m^2)	3.3×10^6	3.604×10^6
Final mud elevation at CS-3 (m)	≈4 −5	4.9
Arrival time to CS-4 (min)	32 − 47	43.5
Free surface increment at CS-4 (m)	5.11	4.06

List of symbols

h	Flow depth
$\mathbf{u}$	(u, v) Depth-averaged flow velocity
ρ	Depth-averaged mixture bulk density
ρ_w	Pore-fluid density
ρ_p	Density of the pth solid phase
φ_p	Depth-averaged volumetric concentration of the pth solid phase
z_b	Bed level

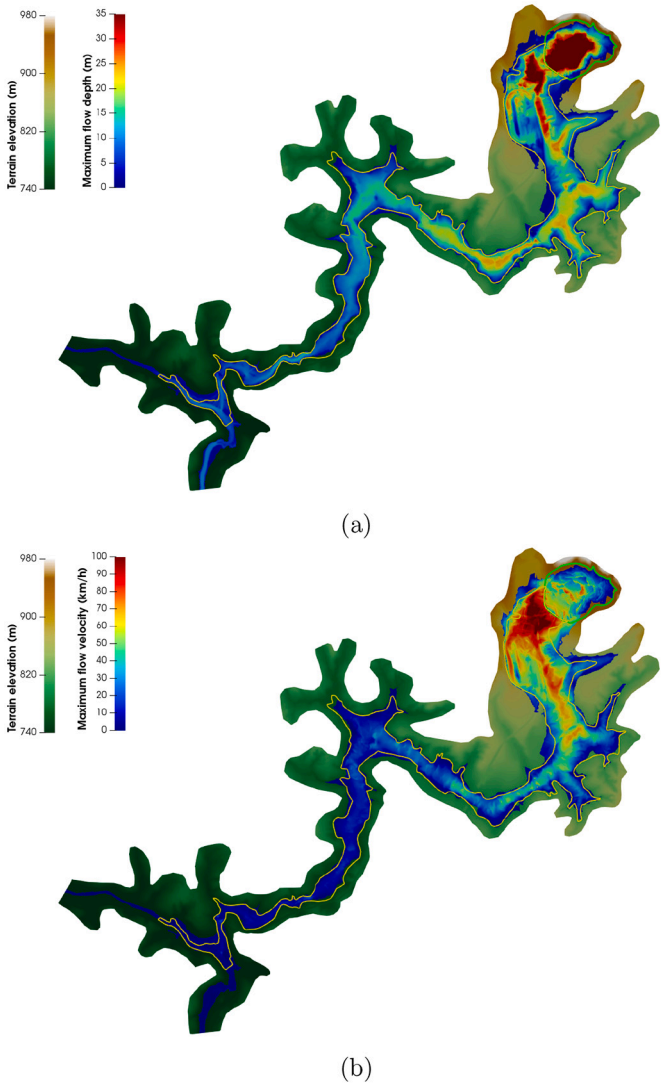

Fig. 31. (a) Maximum mud depth and (b) maximum velocity modulus during the 3 h simulated after the dam collapse.

Table 15
Computational times with GPU-based and CPU-based algorithms.

Comp. domain (m^2)	Number of cells	Comp. time (h)		Speed-up (cpu/gpu) (–)
		GTX 1080 Ti	i7-3820	
10.396×10^6	529339	0.967	59.43	×61.4

$\boldsymbol{\tau}$	(τ_x, τ_y) Basal shear stress
$\cos\psi$	Direction cosine of the bed-normal with the vertical axis
g_ψ	Bed-normal modified gravity
$F_{b,p}$	Bed fraction of the pth solid phase
$N_{b,p}$	Net exchange flux for the pth solid phase
p_p	Deposition porosity for the pth solid phase
$\rho_{b,p}$	Equivalent static bed density for the pth solid phase
$C_{w,p}$	Specific pore-fluid content in the static bed for the pth solid phase
r	Normalized bulk density
φ^χ	Buoyant solid concentration
$\mathbf{U}$	Conservative variable vector
$\mathbf{E}$	$(\mathbf{F}, \mathbf{G})$ Conservative flux matrix
$\mathbf{S_b}$	Bed-pressure momentum source vector
$\mathbf{S_\tau}$	Basal resistance momentum source vector
τ_t	Turbulent/dispersive stress along the flow column
τ_μ	Viscous stress along the flow column
μ	Pore-fluid dynamic viscosity
τ_y	Cohesive-type yield stress
τ_f	Frictional intergranular stress at the bed surface
ϕ_b	Basal friction angle for the flow column
σ_{pp}	Basal pore-fluid pressure
γ_{pp}	Dynamic basal pore-fluid pressure factor
$\mathbf{E_b}$	Bed-flow net exchange vector
D_p	Volumetric deposition rate for the pth solid phase
E_p	Volumetric entrainment rate for the pth solid phase

d_p	Characteristic particle diameter for the pth solid phase
$\omega_{s,p}$	Settling velocity in clear water for the pth solid phase
φ_0	Bulk solid concentration
φ_p^*	Capacity depth-averaged concentration of the pth solid phase
ν	Pore-fluid kinematic viscosity
$q_{s,p}^*$	Solid transport capacity for the pth solid phase
β_T	Modification coefficient for the solid transport capacity
$\theta_{b,p}$	Shield stress at the bed surface for the pth solid phase
n_p	Equivalent Manning roughness parameter for the pth solid phase
n	Bulk Manning roughness parameter
$\theta_{w,p}$	Shield stress along the flow column for the pth solid phase
d_m	Medium particle diameter in the bed layer
$\theta_{c,p}$	Critical Shield stress for the incipient motion of the pth solid phase
$A_{b,p}$	Areal exposure fraction for the pth solid phase
$f_{a,p}$	Fraction of the pth solid phase in the active layer
$f_{s,p}$	Fraction of the pth solid phase in the interface between the active layer and the underlying bed
η_a	Active layer thickness

CRediT authorship contribution statement

S. Martínez-Aranda: Conceptualization, Data curation, Formal analysis, Investigation, Methodology, Software, Validation, Visualization, Writing – original draft, Writing – review & editing. **J. Murillo**: Conceptualization, Formal analysis, Investigation, Methodology, Resources, Supervision, Writing – review & editing. **P. García-Navarro**: Conceptualization, Methodology, Writing – review & editing.

Declaration of Competing Interest

The authors declare that they have no known competing financial interests or personal relationships that could have appeared to influence the work reported in this paper.

Acknowledgements

This work was partially funded by the MINECO/FEDER under research project PGC2018-094341-B-I00 and by Diputacion General de Aragon, DGA, through Fondo Europeo de Desarrollo Regional, FEDER. Authors thank the U.S. Geological Survey (USGS) which supply the experimental data used in Section 5.2 and Hydronia LLC (http://www.hydronia.com/) for providing the data used in Section 5.3.

References

Armanini, A., Fraccarollo, L., Rosatti, G., 2009. Two-dimensional simulation of debris flows in erodible channels. Comput. Geosci. 35 (5), 993–1006.
Berger, C., McArdell, B.W., Schlunegger, F., 2011. Direct measurement of channel erosion by debris flows, Illgraben, Switzerland. J. Geophys. Res.: Earth Surf. 116 (F1), 93–104.
Berti, M., Simoni, A., 2005. Experimental Evidences and Numerical Modeling of Debris Flow Initiated by Channel Runoff, Landslides..
Berti, M., Genevois, R., Simoni, A., Tecca, P.R., 1999. Field observations of a debris flow event in the dolomites. Geomorphology 29 (3), 265–274.
Brufau, P., Garcia-Navarro, P., Ghilardi, P., Natale, L., Savi, F., 2000. 1D mathematical modelling of debris flow. J. Hydr. Res. 38 (6), 435–446.
Burguete, J., García-Navarro, P., Murillo, J., 2008. Friction term discretization and limitation to preserve stability and conservation in the 1D shallow-water model: application to unsteady irrigation and river flow. Int. J. Numer. Meth. Fluids 54, 403–425.
Calhoun, N.C., Clague, J.J., 2018. Distinguishing between debris flows and hyperconcentrated flows: an example from the eastern Swiss Alps. Earth Surf. Process. Landforms 43 (6), 1280–1294.
Cao, Z., Pender, G., Wallis, S., Carling, P., 2004. Computational Dam-Break hydraulics over erodible sediment bed. J. Hydr. Eng. 130 (7), 689–703.
Cao, Z., Li, J., Pender, G., Liu, Q., 2015. Whole-process modeling of reservoir turbidity currents by a double layer-averaged model. J. Hydr. Eng. 141 (2), 04014069.
Cao, Z., Xia, C., Pender, G., Liu, Q., 2017. Shallow water hydrosediment-morphodynamic equations for fluvial processes. J. Hydr. Eng. 143 (5), 02517001.
Castro, M., Fernández-Nieto, E., Ferreiro, A., García-Rodríguez, J., Parés, C., 2009. High order extensions of roe schemes for two-dimensional nonconservative hyperbolic systems. J. Scientific Comput. 39, 67–114.
de la Asunción, M., Castro, M., 2017. Simulation of tsunamis generated by landslides using adaptive mesh refinement on GPU. J. Comput. Phys. 345, 91–110.
Denlinger, R.P., Iverson, R.M., 2001. Flow of variably fluidized granular masses across three-dimensional terrain: 2. numerical predictions and experimental tests. J. Geophys. Res.: Solid Earth 106 (B1), 553–566.
Egashira, S., Honda, N., Itoh, T., 2001. Experimental study on the entrainment of bed material into debris flow, physics and chemistry of the earth, Part C: solar. Terrest. Planet. Sci. 26 (9), 645–650.
Egiazaroff, I., 1965. Calculation of nonuniform sediment concentrations. Proc. ASCE 91, 225–247.
George, L., Iverson, M., 2011. A two-phase debris-flow model that includes coupled evolution of volume fractions, granular dilatancy and proe-fluid pressure. In: 5th International Conference on Debris-Flow Hazards: Mitigation, Mechanics, Prediction and Assessment, 10.
George, D.L., Iverson, R.M., 2014. A depth-averaged debris-flow model that includes the effects of evolving dilatancy. II. Numerical predictions and experimental tests. Proceed. Royal Soc. A: Mathemat. Phys. Eng. Sci. 470 (2170), 20130820.
Godlewski, E., Raviart, P.-A., 1996. Numerical Approximation of Hyperbolic Systems of Conservation Laws. Springer-Verlag, New York.
Greco, M., Di Cristo, C., Iervolino, M., Vacca, A., 2019. Numerical simulation of mud-flows impacting structures. J. Mount. Sci. 16 (2), 364–382.
Gualtieri, C., Ianniruberto, M., Filizola, N., 2019. On the mixing of rivers with a difference in density: the case of the Negro/SolimÒµes confluence, Brazil. J. Hydrol. 578, 124029.
Hess, J., Tai, Y.-C., Wang, Y., 2019. Debris flows with pore pressure and intergranular friction on rugged topography. Comput. Fluids 190, 139–155.
Hirano, M., 1971. River bed degradation with armoring. Proceed. Japan Soc. Civil Eng. 1971 (195), 55–65.
Hungr, O., Evans, S.G., Bovis, M.J., Hutchinson, J.N., 2001. A review of the classification of landslides of the flow type. Environ. Eng. Geosci. 7 (3), 221–238.
Iverson, R.M., Denlinger, R.P., 2001. Flow of variably fluidized granular masses across three-dimensional terrain: 1. Coulomb mixture theory. J. Geophys. Res.: Solid Earth 106 (B1), 537–552.
Iverson, R.M., Ouyang, C., 2015. Entrainment of bed material by earth-surface mass flows: review and reformulation of depth-integrated theory. Rev. Geophys. 53 (1), 27–58.
Iverson, R.M., Vallance, J.W., 2001. New views of granular mass flows. Geology 29 (2), 115–118.
Iverson, R.M., Logan, M., LaHusen, R.G., Berti, M., 2010. The perfect debris flow? aggregated results from 28 large-scale experiments. J. Geophys. Res.: Earth Surf. 115, F03005.
Iverson, R.M., Reid, M.E., Logan, M., LaHusen, R.G., Godt, J.W., Griswold, J.P., 2011. Positive feedback and momentum growth during debris-flow entrainment of wet bed sediment. Nature Geosci. 4, 116–121.
Iverson, R.M., 1997. The physics of debris flows. Rev. Geophys. 35 (3), 245–296.
Jakob, M., Hungr, O., 2005. Debris-Flow Hazards and Related Phenomena, Springer Praxis Books. Springer Berlin Heidelberg.
Juez, C., Murillo, J., García-Navarro, P., 2013. 2D simulation of granular flow over irregular steep slopes using global and local coordinates. J. Comput. Phys. 255, 166–204.
Juez, C., Lacasta, A., Murillo, J., García-Navarro, P., 2016. An efficient GPU implementation for a faster simulation of unsteady bed-load transport. J. Hydr. Res. 54 (3), 275–288.
Kowalski, J., 2008. Two-Phase Modeling of Debris Flows. ETH Zurich, Switzerland. Ph.D. thesis.
Kowalski, J., McElwaine, J.N., 2013. Shallow two-component gravity-driven flows with vertical variation. J. Fluid Mech. 714, 434–462.
Lacasta, A., Morales-Hernández, M., Murillo, J., García-Navarro, P., 2014. An optimized GPU implementation of a 2D free surface simulation model on unstructured meshes. Adv. Eng. Soft. 78, 1–15.
Lacasta, A., Juez, C., Murillo, J., García-Navarro, P., 2015. An efficient solution for hazardous geophysical flows simulation using GPUs. Comput. Geosci. 78, 63–72.
Lacasta, A., Morales-HernÒ¡ndez, M., Murillo, J., GarcÒa-Navarro, P., 2015b. GPU implementation of the 2D shallow water equations for the simulation of rainfall/runoff events. Environ. Earth Sci. 74 (11), 7295-7305.
Lancaster, S.T., Hayes, S.K., Grant, G.E., 2003. Effects of wood on debris flow runout in small mountain watersheds. Water Resour. Res. 39 (6), 21.
Lane, S.N., Parsons, D.R., Best, J.L., Orfeo, O., Kostaschuk, R.A., Hardy, R.J., 2008. Causes of rapid mixing at a junction of two large rivers: RÒO ParanÒ¡ and RÒo Paraguay, Argentina. J. Geophys. Res.: Earth Surf. 113, F02024.
Leighton, F.Z., Borthwick, A.G.L., Taylor, P.H., 2010. 1-D numerical modelling of shallow flows with variable horizontal density. Int. J. Numer. Methods Fluids 62 (11), 1209–1231.
Li, J., Chen, G., 2006. The generalized Riemann problem method for the shallow water equations with bottom topography. Int J. Numer. Meth. Eng 65, 834–862.
Li, J., Cao, Z., Hu, K., Pender, G., Liu, Q., 2018. A depth-averaged two-phase model for debris flows over erodible beds. Earth Surf. Process. Landforms 43 (4), 817–839.
Li, J., Cao, Z., Qian, H., Liu, Q., Pender, G., 2019. A depth-averaged two-phase model for fluvial sediment-laden flows over erodible beds. Adv. Water Res. 129, 338–353.
Li, J., Cao, Z., Cui, Y., Borthwick, A.G., 2020. Barrier lake formation due to landslide impacting a river: a numerical study using a double layer-averaged two-phase flow model. Appl. Mathemat. Model. 80, 574–601.

Luna, B.Q., Remaitre, A., van Asch, T., Malet, J.-P., van Westen, C., 2012. Analysis of debris flow behavior with a one dimensional run-out model incorporating entertainment. Eng. Geol. 128, 63–75.
Macías, J., Castro, M.J., Ortega, S., Escalante, C., González-Vida, J.M., 2017. Performance benchmarking of Tsunami-HySEA Model for NTHMPs inundation mapping activities. Pure Appl. Geophys. 174, 3147–3183.
Major, J.J., Iverson, R.M., 1999. Debris-flow deposition: effects of pore-fluid pressure and friction concentrated at flow margins. GSA Bulletin 111 (10), 1424–1434.
Martínez-Aranda, S., Murillo, J., García-Navarro, P., 2020. A robust two-dimensional model for highly sediment-laden unsteady flows of variable density over movable beds. J. Hydroinfo. 22 (5), 1138–1160.
McArdell, B.W., Bartelt, P., Kowalski, J., 2007. Field observations of basal forces and fluid pore pressure in a debris flow. Geophys. Res. Lett. 34 (7), L07406.
McCoy, S.W., Kean, J.W., Coe, J.A., Tucker, G.E., Staley, D.M., Wasklewicz, T.A., 2012. Sediment entrainment by debris flows: in situ measurements from the headwaters of a steep catchment. J. Geophys. Res.: Earth Surf. 117, F03016.
Meng, X., Wang, Y., 2016. Modelling and numerical simulation of two-phase debris flows. Acta Geotech. 11, 1027–1045.
Ming, X., Liang, Q., Xia, X., Li, D., Fowler, H.J., 2020. Real-time flood forecasting based on a high-performance 2D hydrodynamic model and numerical weather predictions. Water Resour. Res. 56 e2019WR025583.
Murillo, J., García-Navarro, P., 2010. Weak solutions for partial differential equations with source terms: application to the shallow water equations. J. Comput. Phys. 229, 4327–4368.
Murillo, J., García-Navarro, P., 2012. Wave Riemann description of friction terms in unsteady shallow flows: application to water and mud/debris floods. J. Comput. Phys 231 1963–2001.
Murillo, J., García-Navarro, P., 2012b. Augmented versions of the HLL and HLLC riemann solvers including source terms in one and two dimensions for shallow flow applications. J. Comput. Phys. 231, 6861–6906.
Murillo, J., Navas-Montilla, A., 2016. A comprehensive explanation and exercise of the source terms in hyperbolic systems using Roe type solutions.Application to the 1D-2D shallow water equations. Adv. Water Res. 98, 70–96.
Murillo, J., García-Navarro, P., Burguete, J., 2008. Time step restrictions for well balanced shallow water solutions in non-zero velocity steady states. Int. J. Numer. Meth. Fluids 56, 661–686.
O'Brien, J., Julien, P., 1988. Laboratory analysis of mud flow properties. J. Hydr. Eng. 114, 87–887.
Ouyang, C., He, S., Tang, C., 2015a. Numerical analysis of dynamics of debris flow over erodible beds in Wenchuan earthquake-induced area. Eng. Geol. 194, 62–72.
Ouyang, C., He, S., Xu, Q., 2015b. MacCormack-TVD finite difference solution for dam break hydraulics over erodible sediment beds. J. Hydr. Eng. 141 (5), 06014026.
Parsons, J., Whipple, K., Simioni, A., 2001. Experimental study of the grain-flow, fluid-mud transition in debris flows. J. Geol.
Pelanti, M., Bouchut, F. c., Mangeney, A., 2008. A Roe-type scheme for two-phase shallow granular flows over variable topography. ESAIM Mathemat. Model. Numer. Anal. 42 (5), 851–885.
Pierson, T., 2005. Hyperconcentrated Flow - Transitional Process Between Water Flow And Debris Flow. Debris-Flow Hazards and Related Phenomena. Springer Berlin Heidelberg, Berlin, Germany.
Pitman, E.B., Le, L., 2005. A two-fluid model for avalanche and debris flows, philosophical transactions of the royal society a: mathematical. Phys. Eng. Sci. 363 (1832), 1573–1601.
Rickenmann, D., Weber, D., Stepanov, B., 2003. Erosion by debris flows in field and laboratory experiments. In: 3rd International Conference on Debris-Flow Hazards: Mitigation, Mechanics, Prediction and Assessment". Rotterdam, Millpress, pp. 883–894.
Robertson, P., de Melo, L., Williams, D., Wilson, G.W., 2019. Report of the Expert Panel on the Technical Causes of the Failure of Feij ao Dam I, Tech. Rep., Vale S.A..
Roe, P.L., 1981. Approximate riemann solvers, parameter vectors, and difference schemes. J. Comput. Phys. 43, 357–372.
Rosatti, G., Begnudelli, L., 2010. The Riemann problem for the one-dimensional, free-surface shallow water equations with a bed step: theoretical analysis and numerical simulations. J Comput. Phys 229, 760–787.
Rotta, L.H.S., Alcântara, E., Park, E., Negri, R.G., Lin, Y.N., Bernardo, N., Mendes, T.S.G., Filho], C.R.S., 2020. The 2019 brumadinho tailings dam collapse: possible cause and impacts of the worst human and environmental disaster in Brazil. Int. J. Appl. Earth Observ. Geoinfo. 90, 102119.
Toro, E., 1997. Riemann Solvers and Numerical Methods for Fluid Dynamics: A Practical Introduction. Springer-Verlag, Berlin Germany.
Vergilio, C.d.S., Lacerda, D., Oliveira, B.C.V.d., Sartori, E., Campos, G.M., Pereira, A.L.d. S., Aguiar, D.B.d., Souza, T.d.S., Almeida, M.G.d., Thompson, F., Rezende, C.E. d., 2020. Metal concentrations and biological effects from one of the largest mining disasters in the world (Brumadinho, M inas Gerais, Brazil). Scientific Rep. 10 (1), 5936.
Wang, G., Sassa, K., Fukuoka, H., 2003. Downslope volume enlargement of a debris slide-debris flow in the 1999 Hiroshima, Japan, rainstorm. Eng. Geol. 69 (3), 309–330.
Wu, W., 2007. Computational River Dynamics, NetLibrary, Inc. CRC Press.
Xia, C., Cao, Z., Pender, G., Borthwick, A., 2017. Numerical algorithms for solving shallow water hydro-sediment-morphodynamic equations. Eng. Comput. 34 (8), 2836–2861.
Xia, C., Li, J., Cao, Z., Liu, Q., Hu, K., 2018. A quasi single-phase model for debris flows and its comparison with a two-phase model. J. Mount. Sci. 15 (5), 1071–1089.
Zhang, R., Xie, J., 1993. Sedimentation Research in China: Systematic Selections. China Water and Power Press.